Production and characterization of bifunctional highly structured oxygen electrodes for secondary zinc-air battery

Von der Fakultät Energie-, Verfahrens- und Biotechnik
der Universität Stuttgart
zur Erlangung der Würde eines Doktor-Ingenieurs
(Dr.-Ing) genehmigte Abhandlung

Vorgelegt von
Alexander Kube geb. Niederstrasser
aus Karl-Marx-Stadt

Hauptberichter: Prof. Dr. K. Andreas Friedrich
Mitberichter: Prof. Dr. Thomas Turek
Tag der mündlichen Prüfung: 04.04.2023

Institut für Gebäudeenergetik,
Thermotechnik und Energiespeicherung
der Universität Stuttgart

2022

Contents

Abbreviations

BET Brunauer-Emmett-Teller Theorie

CE Counter Electrode

CMC Carboxymethyl Cellulose

CV Cyclic Voltammetry

DRT Distribution of Relaxation Times

EDX Energy Dispersive X-ray Spectroscopy

EEG Erneuerbare Energien Gesetz

EIS Electrochemical Impedance Spectroscopy

EPDM Ethylene Propylene Diene Monomer Rubber

GDE Gas Diffusion Elektrode

GDL Gas Diffusions layer

KOH Potassium Hydroxide

NHE normal hydrogen electrode

OCV Open-Circuit Voltage

OER Oxygen Evolution Reaction

ORR Oxygen Reduction Reaction

PEEK Polyether Ether Ketone

PMMA Poly(Methyl Methacrylate)

PTFE Polytetrafluoroethylene

RE Reference Electrode

SEM Scanning Electron Microscope

RHE Reversibel Hydrogen Electrode

SHE Standard Hydrogen Electrode

USBM US Bureau of Mines

WE Working Electrode

XRD X-ray Diffraction

ZnO Zinc oxide

TMO Transition Metal Oxides

MOF Metal Organic Frameworks

DoD Depth of Discharge

1. Motivation

The European Union's Renewable Energy Directive of 2018, according to which at least 32 % of energy production is to come from renewable sources in 2030, is further accelerating the transformation of energy production. In Germany, this transformation can be observed since 2000, when the Erneuerbare Energien Gesetz (EEG) started the energy transition which increases share of e.g. solar, wind and tidal power plants in the German electricity mix. Due to the dependence of renewable energies on environmental influences such as sunshine or wind strength, there is a divergence between production and consumption periods.

To meet the changing requirements, powerful and cost-effective energy storage systems are needed that combine high control performance with a short response time. Stationary electrochemical energy storage systems such as batteries are particularly suitable for this purpose and can contribute to a stable, secure and versatile energy production landscape. In contrast to the pumped storage power plants that dominate today, batteries can be placed modularly at the point of energy production without having to create special infrastructure, as is the case with pumped storage power plants. By using the highly flexible and scalable battery technologies, energy can be delivered in a targeted manner at any point in time when it is needed, thus reducing the price of electricity as a whole. In today's electricity mix, regulation takes place mainly through the switching off and on of generators and consumers, such as aluminum smelters. The example of the Li-ion based system installed in Australia by Tesla demonstrates the efficiency of such a system. This battery storage cost $ 95m, has a size of 100 MW /129 MWh and generates $4m [1] per year through the control power provided. Li-ion batteries are mainly used for this purpose, but in addition to their many advantages, they also have major disadvantages in terms of safety and cost. For example, in 2018, more than 20 Li-ion-based grid storage units burned in South Korea [2].

Alternative battery technologies such as metal-sulfur or metal-air batteries can compensate for the disadvantages mentioned here, have higher storage densities depending on the technology and are safer because, for example, no thermal runaway occurs. Zinc-air batteries, which are investigated in this work, are considered to be particularly safe and can well replace Li-ion batteries in the field of grid storage due to their high capacities and due to the very common materials which are easy accessible.

2. Zinc-air battery

The advantage of metal-air batteries is their very high theoretical energy density. This advantage is achieved by using metal electrodes on the negative electrode side and gas diffusion electrodes as the positive electrode, where the reactant oxygen is taken from the surrounding atmosphere and thus does not need to be stored within the battery. A variety of possible elements are available for the metal negative electrode, such as iron (Fe), zinc (Zn), magnesium (Mg), aluminum (Al), lithium (Li) or sodium (Na), with each material having its own advantages and disadvantages. Here, Al- (8076 Wh/kg), Mg- (6815 Wh/kg), and Li-air batteries (11429 Wh/kg) show the highest theoretical energy densities [3].

2.1. State of the art

The only commercially available metal-air battery to date is the Zn-air battery, which is widely used commercially as a primary battery, e.g. in hearing aids. The theoretical energy density of the Zn-air battery is 1358 Wh/kg for the pure metal and 1086 Wh/kg with oxygen, and is approximately 3 times greater than the capacity of currently commercially available Li-ion batteries, which have energy densities in the range 350-500 Wh/kg [3, 4]. The first commercial Zn-air battery was patented as early as 1933 [5, 6] and has since found application in various fields, such as electrically powered automobiles [7, 8], ocean-going buoys, and train signals. The present application of primary Zn-air batteries is mainly as hearing aid batteries. Secondary Zn-air batteries are mainly used as stationary power storage devices. Of particular note here is NantEnergy's system, which uses an ionic liquid with hygroscopic additive [9] and, according to press reports, can be manufactured for less than $100 kWh. This is currently the only commercially available secondary Zn-air battery system.

2.1.1. Positive electrode

The positive electrode consists of an electrically conductive highly porous medium, which in the literature is often carbon-based [10]. However, there are also approaches using other conductive media, such as nickel [11], silver [12] or other metal based materials. Another component of the positive electrode is the catalyst, for which there are many examples in the literature. Among them spinels with general formula AB_2X_4 like Co_3O_4 and $NiCo_2O_4$ [13] and perovskites with general formula ABO_3 [14] like $LaNiO_3$ and $La_{1-x}Ca_xCoO_3$ [13][15]. At the three-phase boundary between gas, electrolyte, and catalyst, the conversion of oxygen to OH^- takes place. Here, in the alkaline system used in this work, a distinction is made between the direct 4-electron pathway (equation 2.1) and the indirect 2-electron pathway (equations 2.2 and 2.3)

[16]. All equations additionally give the reaction potentials versus the Standard Hydrogen Electrode (SHE).

Direct 4-electron process

$$O_2 + 2H_2O + 4e^- \rightarrow 4OH^-, \text{ 0,401 V vs. SHE} \tag{2.1}$$

2-electron process

$$O_2 + H_2O + 2e^- \rightarrow HO_2^- + OH^-, \text{ -0,065 V vs. SHE} \tag{2.2}$$

$$HO_2^- + H_2O + 2e^- \rightarrow 3OH^-, \text{ 0,867 V vs. SHE} \tag{2.3}$$

Since, in contrast to the fuel cell, both the Oxygen Reduction Reaction (ORR) and the Oxygen Evolution Reaction (OER) take place at the Gas Diffusion Elektrode (GDE). The stability of the materials used in the resulting large potential range is essential. This is also the basis for the carbon-free approaches mentioned above, since carbon is oxidized to CO_2 during OER. In this work, the ORR describes the cathodic operation, the OER the anodic operation.

The electrochemical performance as well as the cycling stability of the GDE depends on a large number of parameters. Due to the wide potential range during charging and discharging, oxidation as well as reduction reactions of the materials within the GDE occur. This leads to a degradation of both the catalyst and the conductive medium and accordingly in a loss of the electrochemical activity of the electrode. The resulting change in the pore structure can lead to a higher wettability and thus to a higher flooding degree of the pore space with electrolyte. The degree of flooding within the pore space is also dependent on the negative electrode, which increases its volume during discharge by converting Zn to ZnO, and on the air humidity. High humidity leads to increasing flooding, while low humidity causes the pore space and the battery to dry out.

The preferred catalysts are Transition Metal Oxides (TMO) and Metal Organic Frameworks (MOF). TMO currently have the advantage of higher activity for OER as well as for ORR and lower cost. Furthermore, they are abundant, non-toxic and the catalysts from them are easier to prepare. The group of TMO-based catalysts includes simple metal oxides, spinels, and perovskites (ABO_3, A,B=metal). MOF, on the other hand, have only recently been used for rechargeable Zn-air batteries, have advantages in mass and charge transport due to their large surface area and interconnected pores. However, these materials still show weaknesses in reproducibility, cost, and complex synthesis.[17]

Ni is often used as a conductive additive, since carbons are not stable in the wide potential range and are converted to CO_2 by carbon corrosion.
In the literature, two cell architectures are generally distinguished:

1. *Two-electrode setup*: This design, known from the primary zinc-air battery, uses a bifunctional electrode on the positive electrode side. Here, the positive electrode is operated over the entire potential range of the charging and discharging processes, exposing the

materials to both oxidative and reductive stress. The stability of the positive electrode materials in this large potential range is essential for this cell architecture and will be discussed in more detail in chapter 4. The advantages of this architecture are smaller battery sizes and thus higher volumetric energy densities as well as increased power density during the onset of discharge due to reduction of positive electrode materials oxidized during the charging process [18].

2. *Three-electrode setup*: This architecture reduces stress on the positive electrode materials by electrically separating the positive electrode into two electrodes, one for charging, one for discharging. The advantage of this design is the ability to use inexpensive positive electrode materials for the discharge positive electrode, such as carbon, thereby reducing costs while increasing electrode life. The disadvantage is that, depending on the concept, it is difficult to remove the developed oxygen. In addition the volume and weight of the battery are increased.

In this work, the two-electrode setup with metallic conductive aditives (Ag, Ni) and the spinel Co_3O_4 is used.

An additional challenge for high cycle stability is the use of highly alkaline electrolytes where insoluble carbonates (e.g. K_2CO_3 or $KHCO_3$) can precipitate. These are formed by the reaction of KOH with CO_2 and can separate the electrolyte space from the gas space, reducing battery performance.

2.1.2. Negative electrode

Metallic zinc serves as the negative electrode of the Zn-air battery, which reacts according to the reactions 2.4 - 2.6 in the alkaline system to form ZnO.

$$Zn \rightarrow Zn^{2+} + 2e^- \tag{2.4}$$

$$Zn^{2+} + 4OH^- \rightarrow Zn(OH)_4^{2-}, \text{ -1,25 V vs. SHE} \tag{2.5}$$

$$Zn(OH)_4^{2-} \rightarrow ZnO + H_2O + 2OH^- \tag{2.6}$$

For the highest possible degree of utilization of the zinc, a high surface area and small particle sizes are necessary, since the ZnO layer that forms serves as a diffusion barrier. For a high cycle stability, the preservation of the 3D structure of the negative electrode is mandatory, since rearrangement of the zinc reduces diffusion paths and reactive surface area. Different strategies for this can be found in the literature. One of these is the deposition of a zinc layer on a conductive medium, e.g. copper, which provides the structure. A second possibility is the sintering of zinc powder with subsequent oxidation of the uppermost zinc layer. In combination with only a low utilization of the capacitance, the specified structure should be maintained during the cycles. However, both strategies have the disadvantage of reducing the theoretical energy density of the negative electrode. As a third strategy, gelation of the electrolyte is used.

Polymer fibers (e.g. Carboxymethyl Cellulose (CMC)) are used here to maintain paths for electrolyte diffusion throughout charging and discharging.

In addition to the changes in the negative electrode morphology, parasitic hydrogen evolution at the negative electrode is a major challenge, as it reduces both the capacity and the efficiency of the battery. Furthermore, especially at high current densities, dendrites can form which can short-circuit the battery.

2.1.3. Electrolyte and separator

Electrolyte systems for the Zn-air battery can be divided into three classes:

1. *Aqueous-alkaline*: Provides very high capacities due to the precipitation of Zinc oxide (ZnO), as the discharge reaction is not limited by solubility limits. Most commonly used electrolyte is 7 - 8 M potassium hydroxide KOH, which has very high conductivities in the range of 600 to 800 mS. Due to the high pH, potassium carbonate forms in this system, which decreases the conductivity of the electrolyte and the pH, and can block the pore space of the positive electrode. One way to minimize potassium carbonate formation is to reduce the pH, as presented in [19].

2. *Aqueous-acidic*: The aqueous acidic system also shows high conductivities. However, compared to the alkaline system, the acidic system shows a stronger tendency to hydrogen evolution. Due to the low pH, ZnO deposition is not favored in this system, resulting in lower capacities than the aqueous-alkaline system. For the aqueous-acidic system, research is focused on pH values close to neutral. The first studies on this, in which different electrolyte variations were tested, date back to 1973, suggesting the favoring of chlorine-based compounds over nitrate-based ones, since high corrosion of zinc was observed in nitrate-based electrolytes. In particular, the $ZnCl_2$-NH_4Cl system, known from the Leclanché battery, was studied for the Zn-air battery [20–22].

3. *Ionic liquid*:

   Ionic liquids are room temperature liquid molten salts of organic salts that have high conductivity and support electrochemical reactions [23]. Since ionic liquids are non-volatile, water management is not required for them. However, a large number of ionic liquids exhibit a high degree of wetting of the positive electrode materials, which can lead to flooding of the pore space and low formation of a stable three-phase boundary. Furthermore, ionic liquids are very cost-intensive. By adding H_2O, both the wetting properties on the positive electrode side, the zinc deposition on the negative electrode side and the costs can be positively influenced [24].

The use of additives is also a promising approach to increase the cycle stability of the battery by suppressing individual weak points of the system. These include, for example, improving Zn deposition, preventing dendrite growth, stabilizing the zinc structure and suppressing parasitic hydrogen evolution. The additives can be grouped into three classes: organic additives, metal oxide additives and structural electrode modifiers. It should be mentioned here that only a

small portion of the additives are used to prevent weak spots on the positive electrode side, and research on additive studies is focused on the negative electrode.[25]

2.2. Interrelation between the studies and the overall scientific context

In the literature, the components of the Zn-air battery are usually considered individually, without taking into account their effect on the other components. The focus of many works is on the material level, such as the development of suitable catalysts to reduce the required overpotentials and to achieve higher current densities. The development of novel electrolyte compositions to reduce the pH, reduce hydrogen evolution on the negative electrode side and preserve the morphology of the negative electrode structure by e.g. gelation of the electrolyte. Mostly with the focus on the negative electrode. The concept of this dissertation is to identify the important positive electrode aspects leading to performance loss and degradation. In particular, gas heterogeneity, the effect on degradation of the negative electrode, electrolyte penetration and the influence of electrolyte composition on performance and degradation is studied. With this approach a more rational development of rechargeable Zinc-Air batteries becomes possible. For this purpose, different methods for quantification have been developed and applied.

Figure 2.1 shows the schematically the current issues of the Zn-air system and which area is addressed by the publications explained below.

The performance of zinc-air batteries depends mainly on the performance of the positive electrode. This is due to the sluggish ORR. The highest current densities are achieved in the region of the three-phase boundary, which means that a large active area in the region of the three-phase boundary is required for high battery performance, and this must be supplied with sufficient reactants, especially gas. By adding Polytetrafluoroethylene (PTFE), the positive electrode is hydrophobized and a stable three-phase boundary can be established. For the gas supply, investigations in the fuel cell field show that there are a large number of possible flow field variations and that these have a strong influence on the performance of the electrodes.[26] It has also been shown that a homogeneous gas distribution leads to a more homogeneous current density distribution and thus also to a more uniform temperature distribution. This reduces the mechanical stress within the positive electrode.[26] Together with the more uniform current density distribution and the resulting more uniform overvoltage-induced aging, this leads to homogeneous aging of the positive electrode and thus longer lifetimes. For zinc-air batteries, the influence of the gas distribution has so far only been investigated at electrode level for cells with a maximum size of 10x10cm. Here, a consistent picture has emerged that the performance of the battery increases with increasing gas flow. However, if the gas flow is set too high, the performance decreases again due to higher pressures in the system, which push electrolyte out of the positive electrode.[27, 28] However, these findings were measured without segmentation and thus only provide information about the averaged current density. In publication I (red text in figure 2.1), the influence of the gas supply was investigated with a segmented measurement

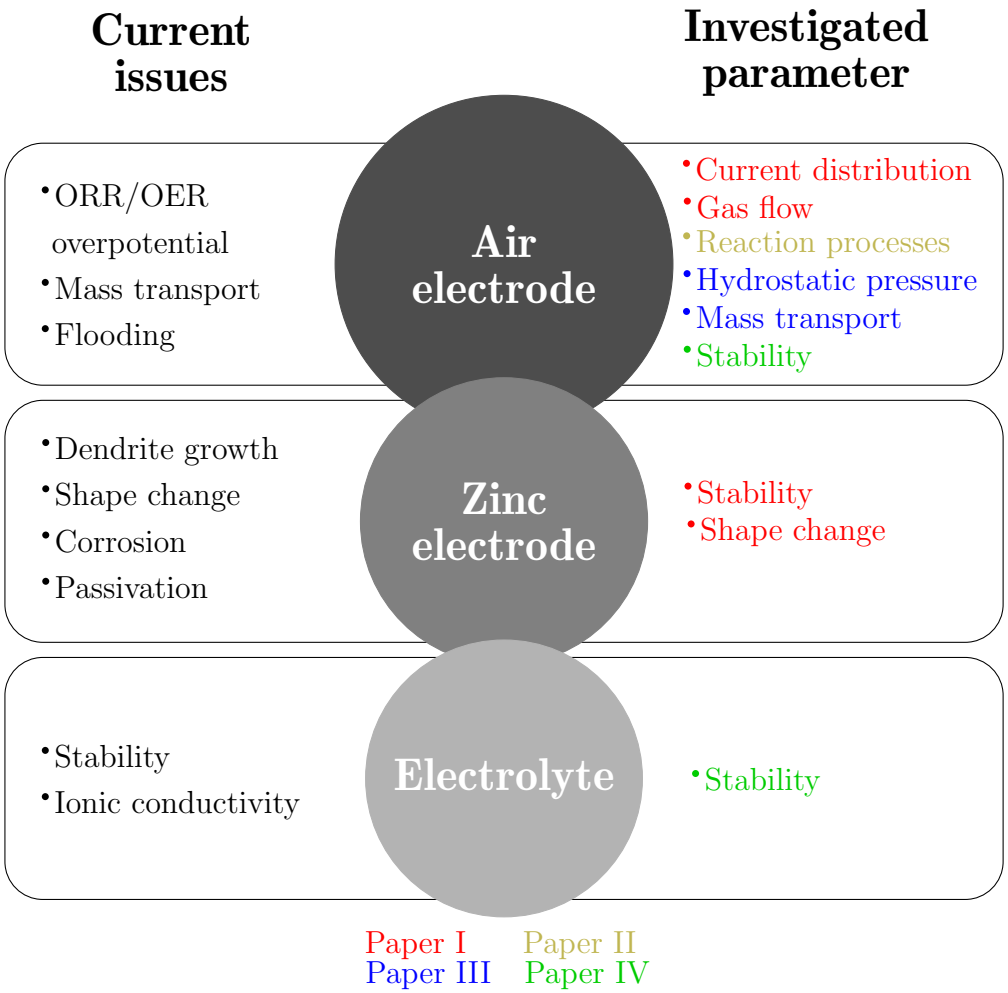

Figure 2.1.: Schematic representation of the interrelation of the articles

technique on the positive electrode side. It could be shown that, analogous to the observations in fuel cell systems, the current density distribution is strongly influenced by the gas flow. Furthermore, it was shown that the current density distribution is very sensitive to the gas pressure. This is due to the fact that the three-phase boundary is pushed further towards the electrolyte space at high pressures. This observation is in agreement with the gas flow measurements of Shallal et al. and Sangeetha et al.[27, 28] However, it could be shown that gas pressures induced by the flow velocity must be distributed homogeneously over the electrode area to avoid current density heterogeneities. Since Zn-air battery use ambient air as feed gas, the gas composition over the electrode area is also a factor to be considered. In their studies, Pichler et al. were able to show that cycle life is greatly reduced when synthetic air is used and attributed this to the fact that nitrogen blocks transport to the active sites. [29]. In publication II (yellow text in Figure 2.1), this increased transport resistance was confirmed using Electrochemical Impedance Spectroscopy (EIS).

The penetration behavior of the electrolyte into the GDE is determined not only by the gas pressure induced by the gas flow but also by the electrode structure itself and is the key for a high achievable performance of the battery. Because of this, it is also the subject of intensive research in the field of fuel cells as well as CO_2 electrolysis. Especially on the pore scale, a heterogeneous

distribution of the electrolyte has been demonstrated. Paulisch et al. demonstrated by means of synchotron radiation how the pores are continuously filled at constant current, and that there are pores which are preferentially filled. On the other hand, there are also pores into which electrolyte apparently does not penetrate, which function for the gas transport into the depth of the electrode. [30] The observations could be confirmed by simulations by Röhe et al. Also, Röhe et al. showed that the position of the three-phase boundary within the porous structure of the positive electrode affects the electrochemical performance more than the wetted catalytically active surface [31] In addition to these effects in the GDE, conditions outside the electrode also influence the saturation level of the porous system. Schröder et al. could show by X-ray tomography that the increase in volume of zinc during discharge pushes electrolyte into the porous positive electrode. The overvoltage in the positive electrode, which increased due to the flooding, therefore also limited the capacity of the battery by prematurely reaching the end-of-charge voltage.[32] Since the slow charge and discharge rates of the zinc-air battery mean that the main area of application should be stationary storage, it is highly likely that large-format cell types will be used. With these, the hydrostatic pressure of the electrolyte is added to the phenomena explained so far. This results in a heterogeneity in the penetration depth of the electrolyte over the electrode area and, consequently, a heterogeneous current density distribution. To quantify this effect, a riser tube cell was used in publication III (blue text in figure 2.1). By means of chronoamperometry measurements as well as impedance measurements it could be shown that the hydrostatic pressure indeed leads to a higher penetration depth and thus to a reduced electrochemical performance. These investigations were preceded by a series of measurements to determine the individual processes within the electrode using EIS as well as Distribution of Relaxation Times (DRT). In the literature, there has been little investigation using EIS for the thick GDE of Zn-air batteries. Ma et al. compared new and aged GDEs and empirically assigned processes and used equivalent circuits known from the literature.[33] Publication II (yellow text in Figure 2.1)) uses DRT to visualize the number of processes and use parameter variation to identify the underlying processes. This showed a general agreement between the assumptions in Ma's research and the research in this paper. There were differences especially concerning the adsorption resistance as well as the ionic and electrical transport in the pores, which were neglected by Ma. Furthermore, it was shown that the complex structure of the Ni/CO_3O_4-electrode leads to the fact that the DRT cannot resolve the occurring two parallel transmission line models to describe the ionic and electrical transport in the pore system of the CO_3O_4-agglomerates and the bigger pores between the agglomerates and the Ni-particles. Knowledge of the individual processes and their behavior at different electrode operating conditions is the basis for the impedance-based studies in Publication III, as described above, and was applied to study the penetration behavior of the electrolyte. At the cell level, the effect of hydrostatic pressure was investigated using the segmented measurement technique and it was found that the effect increases with increasing number of cycles and the higher current densities occur in the upper region of the cell with lower hydrostatic pressure. It also showed that only the three-phase boundary dependent ORR exhibits the shift in current density distribution, whereas the two-phase boundary dependent OER shows no significant change in current density distribution.

An aspect that has been rarely investigated in the literature is the difference in the wetting behavior of the electrode during charging and discharging. Due to the large potential range during charging and discharging, the positive electrode materials undergo several oxidation/reduction steps depending on the material, which results in a volume change of the particles as well as different contact angles of the electrolyte on the positive electrode materials. This difference could be shown in publication III by means of pressure saturation curves. In addition, the changed particle sizes resulted in large differences in the transport parameters.

The rate of change of the positive electrode structure due to oxidation and reduction processes is thereby dependent on the current density distribution, which is linked to concentration gradients in the electrolyte.[34] These in turn have a direct effect on the reaction rates on the negative electrode side. As shown in Publication I, heterogeneous current distribution, in this case due to hydrostatic pressure, leads to heterogeneous dissolution of the negative electrode. The maintenance of the negative electrode structure, however, is critical for high cycling stability, as well as for the high capacitances. Li et al. have investigated the influence of current intensity as well as depth of discharge (DoD) on the cycling stability of zinc deposited on a carbon nanofiber network as well as on titanium. On the one hand, it was shown that higher current densities lead to increased dendrite growth as well as reduced useful capacities. Decreasing cycle life was shown for increasing DoDs. [35] This is due to the nature of the reaction mechanism as described in equation 2.4-2.6. During discharge, $Zn(OH)_4^{2-}$ is formed first, which precipitates as ZnO after reaching the solubility limit. This can lead to zinc not being deposited in the place where it went into solution and thus to a change in mophology. This results in a densification of the negative electrode which leads to a loss of porosity and therefore to a capacity reduction.[36] As explained above, the heterogeneous dissolution of the zinc was shown in publication I. In this case, it was also evident on the negative electrode side that the zinc underneath the zinc oxide layer is dissolved during discharge and thus the zinc oxide loses its adhesion to the surface of the negative electrode. This shows on the one hand that the usable capacity of the negative electrode must be limited, as it has already been shown in many studies,[37–39] as well as that one must consider the mutual influence of the electrodes. In previous studies, mainly small electrodes and/or only the negative electrode were considered, which meant that the mutual influence was still negligible.

The deposition of zinc oxide on the negative electrode surface can be influenced by adding additives to the electrolyte solution to achieve a higher uniformity.[40–42] Especially organic additives such as succinic acid, or tartaric acid are used.[43, 44]. These can also act as pH buffers and thus be used to reduce the pH, as suggested by Clark et al.[45] To increase the hydrogen evolution potential, various additives such as bismuth, indium, or organic additives can be added directly to the electrolyte or negative electrode.[45] The commonly used electrolyte in Zn-air batteries is KOH due to its high conductivity. However, this reacts with CO_2 to form carbonates. This lowers the electrolyte concentration, as well as blocks pores of the positive electrode, resulting in reduced battery life and usable capacity.[46] However, in most of the studies conducted in the literature, only the effect on the negative electrode is investigated; whether there is an effect on the positive electrode is rarely investigated. In Publication IV (green text Figure 2.1), the electrolyte proposed by Clark et al. consisting of potassium citrate,

glycine, and zinc oxide was studied in more detail for the positive electrode side. The electrolyte composition is intended to both stabilize the pH at pH 9 and gel the electrolyte to preserve the structure of the negative electrode. Both Ni-based and Ag-based electrodes were used for this purpose and showed greatly reduced electrochemical performance, which could be attributed to the use of citric acid. The carboxyl groups on the citric acid also caused a dissolution process of the positive electrode materials, due to a Kolbe electrolysis. This effect was well observed in the electrolyte studied due to the high concentration of citric acid. However, it can be assumed that this effect also occurs with smaller amounts of carboxylic acids in the electrolyte, such as the tartaric acid, succinic acid etc. used in other studies. Furthermore, it has been shown that the electrolyte additives used are not stable in the wide potential range on the positive electrode side and are decomposed to CO_2 and hydrogen.

The mutual influences of the electrodes shown in the publications indicate that the challenges of the individual electrodes must be solved on the way towards commercialization, but the influence of an improvement on the overall system must also be kept in mind. This also applies to effects such as the expansion of the negative electrode during discharge, which affects the electrolyte pressure and thus the degree of saturation of the porous structure of the positive electrode and consequently the performance of the battery. In solving this issue, the understanding gained by means of the studies of the wetting characteristics of the positive electrode in this work helps and is thus another piece of the puzzle on the way towards electrically rechargeable batteries.

3. Fundamentals

In the following, an overview of the measuring methods used as well as the measuring equipment used is given. The cells developed for this work are presented.

3.1. Cyclic voltammetry

Cyclic voltammetric investigations (CV) can be used to study electrode reactions. For this purpose, a potential which changes linearly in time is applied on the cell between two reversal potentials, the direction of change changes when the reversal potential is reached. At potentials characteristic of the respective electrochemical processes, a current flow attributable to the reaction can be registered. Two cases can be distinguished here:

1. Substances with finite concentration, e.g. oxide layers, are characterized by a recordable peak in which the current flow decreases with time due to depletion of the reaction species.

2. Substances of infinite concentration, e.g., oxygen reduction, are characterized by a steady increase in current density until a transport limit is reached, above which the current flow remains constant.

For reversible reactions, the peak current can be calculated using the Randles-Sevcik equation [47]

$$i_p = 2,686 \cdot 10^5 \cdot z^{\frac{3}{2}} \cdot A \cdot D^{\frac{1}{2}} \cdot \nu^{\frac{1}{2}} \cdot c^0 \tag{3.7}$$

With the parameters electrode area A, diffusion coefficient D, scan velocity ν, the number of electrons transferred z and concentration of the reactant c^0, it describes the dependence of the peak current i_p on the concentration of the reactants. The peak potential of reversible reactions can be calculated from the potential difference between the anodic and cathodic peak potentials according to

$$|E_p^{ox} - E_p^{red}| = 2,303 \cdot \frac{R \cdot T}{z \cdot F} \tag{3.8}$$

with the oxidation potential E_p^{ox} and the reduction potential E_p^{red} [48, 49]. The general gas constant is described by R, the temperature by T, the Faraday constant by F, and the number of electrons involved in the reaction by z.

3.2. Electrochemical impedance spectroscopy

The EIS is a non-destructive measurement method for determining the kinetics of the electrochemical and physical reactions occurring at the electrode. An applied sinusoidal disturbance of the system results in a likewise sinusoidal but phase-shifted response signal of the same frequency and an amplitude deviating from the excitation amplitude. A distinction is made between galvanostatic and potentiostatic operation:

1. *Galvanostatic operation*: An alternating current is applied, the response signal is an alternating voltage.

2. *Potentiostatic operation*: An AC voltage is applied, the response signal is an AC current.

.

Processes assigned in the equivalent circuit can be used to describe the subprocesses occurring in the electrode. These subprocesses are represented in the equivalent circuit by defined elements and are briefly introduced below. Ohmic behavior, such as electrical and ionic conduction (e.g. electrolyte), can be described via a resistor R. A coil with inductance L describes the inductive influence, e.g. of the cables. The charge tranfser resistance is a process depending on the speed of the charge transfer and results from the Butler-Volmer equation according to equation 3.9 with the activity coefficient α, the overpotentials $\eta^{=}$ of the constant applied voltage and $\eta_D^{\sim}$ of the AC voltage as well as the current densities $i_D^{=}$ of the DC current and $i_D^{\sim}$ of the AC current [50] for the ORR:

$$R_D = \frac{\eta_D^{\sim}}{i_D^{\sim}} = \frac{RT}{zF} \frac{1}{(\alpha \cdot i_D^{=} + i_0 \cdot exp(-(1-\alpha) \cdot \eta^{=} \cdot \frac{zF}{RT}))} \tag{3.9}$$

In the no-current state (Open-Circuit Voltage (OCV)) with $\eta^{=} = 0$ and $i_D^{=} = 0$, the equation simplifies to.

$$R_D = \frac{RT}{zFi_0} \tag{3.10}$$

This charge tranfser resistance is often described by an R||C element, in which a resistor and a capacitor are connected in parallel, at equivalent circuit level. The capacitance C describes the charge separation caused by the capacitance of the double layer of the electrolyte-electrode interface.

Adsorption can be described by an R||C element according to the equations 3.11 and 3.12 [51],

$$R = \frac{RT}{n^2F^2c_sAk_r} \tag{3.11}$$

$$C = \frac{n^2F^2c_sA}{RT} \tag{3.12}$$

with the temperature and concentration dependent rate constant k_r of the reaction, the surface concentration c_s as well as the electrode surface A.

The diffusion of individual reactants, such as oxygen transport in air, or ion transport in the electrolyte, can be described by diffusion elements such as the finite 1-D transmissive diffusion impedance, also called Nernst diffusion, according to equation 3.13,

$$Z_W = \frac{W}{\sqrt{j\omega}} \frac{tanh\sqrt{j\omega}}{\sqrt{k_N}} \tag{3.13}$$

with

$$W = \frac{|\nu_k| p_k RTa}{z^2 F^2 c_k \sqrt{D} A}, \qquad [W] = \frac{\Omega}{\sqrt{s}} \tag{3.14}$$

and

$$k_N = \frac{D}{d_N^2}, \qquad [k_n] = s^{-1} \tag{3.15}$$

in which p_k describes the reaction order, ν_k the stoichiometric number, c_k the concentration, a the coupling factor resulting from the transfer coefficients of the partial currents, d_N the thickness of the diffusion layer and ω the frequency.

3.2.0.1. Distribution of relaxation times

The relation between the complex impedance $Z(\omega)$ and the distribution function of relaxation times (DRT) is given by equation 3.16 [52]. The distribution function allows the separation of electrochemical processes with different time constants, where the impedance function is decomposed into an infinitesimal sum of differential R||C elements,

$$Z(\omega) = R_0 + Z_{pol}(\omega) = R_0 + R_{pol} \int_0^\infty \frac{\gamma(\tau)}{1 + j\omega\tau} d\tau \tag{3.16}$$

with

$$\int_0^\infty \gamma(\tau) d\tau = 1 \tag{3.17}$$

and the ohmic resistance R_0 as well as the polarization resistance $Z(\omega)$, the distribution function $\gamma(\tau)$ and the time constant τ.

To solve the distribution functions, various solution approaches can be found in the literature such as by applying a Fourier transform [53, 54], or the Tikhonov regularization approach [55–57] used in this work. This requires fewer parameters than the Fourier transform to solve equation 3.16, in this case mainly the parameter λ, which suppresses the oscillation of the solution:

$$min_{\overline{\gamma}} = \{\|\boldsymbol{H}\overline{\boldsymbol{\gamma}} - \boldsymbol{z}\|^2 + \lambda\|\overline{\boldsymbol{\gamma}}\|^2\} \tag{3.18}$$

Here $\boldsymbol{H}$ describes a NxM matrix, $\overline{\boldsymbol{\gamma}}$ the vector with the unknowns and $\boldsymbol{z}$ a vector with the measured values of the impedance spectroscopy.

3.3. Mercury porosimetry

Mercury porosimetry is a widely used technique for determining pore volume, pore diameter and distribution, as well as the porosity. Here, non-wetting mercury penetrates the porous system of the sample to be measured while simultaneously varying and recording the external pressure. Using the Washburn equation 3.19, the corresponding pore radius can be determined from the pressure p with the pore radius r, the mercury surface tension γ, the wetting angle Θ [58].

$$p = \frac{-2\gamma cos(\Theta)}{r} \tag{3.19}$$

Measurements to determine mercury porosimetry were carried out in this work using a Pascal 140 measuring system in combination with Pascal 240 from the company Porotec.

3.4. Nitrogen absorption measurement

Nitrogen absorption measurement (Brunauer-Emmett-Teller Theorie (BET)) is a method in which the adsorption of gas molecules on the surface of the particles to be measured is used to determine the specific surface area cm^2/g of the particle material. For this purpose, the adsorbed gas quantity n_{ads} is measured as a function of the gas pressure p.

$$n_{ads} = f(p) \tag{3.20}$$

The adsorption isotherm of Brunauer, Emmett and Teller can be used to infer the number of adsorbed molecules, and the area of the measuring material can be calculated using the known area of the adsorbed molecule. As measuring gas for surfaces larger than $1\,m^2$ usually nitrogen is used, for surfaces smaller than $1\,m^2$ krypton. The specific surface area cm^2/g determined in this way is an important quantity in electrochemistry, since the activity of a material is also a function of the surface [59].

3.5. Scanning electron microscopy

Scanning Electron Microscope (SEM) uses accelerated electrons to generate images, which are rastered over the area of the sample to be examined. The accelerating voltages used to accelerate the electrons in the cathode are in the range of 60 - 100 keV. After acceleration, the electrons are focused by condenser lenses and strike the sample surface as a focused beam. This produces, among other things, backscattered, Auger and secondary electrons as well as X-rays, which are collected and further processed in the respective detectors. A schematic representation of the SEM and the interaction lobe are shown in Figure 3.1.

Secondary electrons generated by inelastic interaction with valence electrons of the sample as well as backscattered electrons generated by elastic interaction with atomic trunks serve as the most common analysis methods for image acquisition. The characteristic X-rays produced

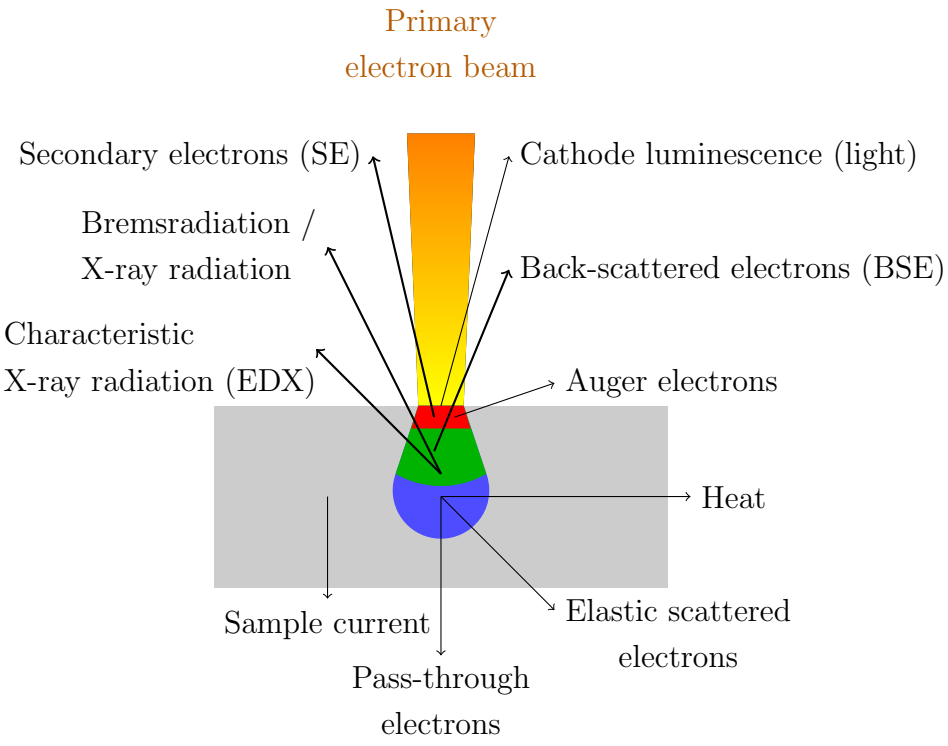

Figure 3.1.: Schematic representation of the interaction lobe of the electron beam with the material of the sample

by interaction of primary electrons with orbital electrons of the sample are used for energy dispersive X-ray spectroscopy (EDX) analysis to determine elemental composition [60].

SEM Images in this work were taken using an Ultra Plus. Attached to this is a Bruker EDX detector (XFlash 5010 125eV) for compositional analysis.

3.6. X-ray diffraction

The method of X-ray diffraction (XRD) is used to analyze the chemical composition of crystalline samples. Monochromatic X-rays, with a wavelength typically in the range of 10^{-3} to 10^{-1} nm, are accelerated onto a crystalline sample and diffracted according to the Bragg equation 3.21.

$$n\lambda = 2dsin(\Theta) \tag{3.21}$$

The Bragg equation describes with the wavelength λ, the spacing between diffracting planes d, the incident angle Θ as well as the degree of the examined maximum n the condition under which constructive interference occurs. This constructive interference can be detected in the spectrum as phase-specific characteristic peaks [61]. By angle-dependent detection, the peaks can be recorded and the phase-specific diffractogram can be generated. A X-ray Diffraction (XRD) system (Bruker D8 Discover GAAS) with CuK_α radiation was used for this purpose.

3.7. Cells

3.7.1. Half-cell

The electrodes fabricated in this work were measured in a half-cell setup as schematically shown in figure 3.2. The advantage of the setup used is that the negative and positive electrode processes are decoupled, allowing each electrode to be characterized individually under varying operating conditions. In this setup, the voltage is measured at high impedance against a reference electrode (RE), which is connected via a Haber-Luggin capillary to the working electrode (WE). The current is measured between a platinum counter electrode (CE) and the working electrode.

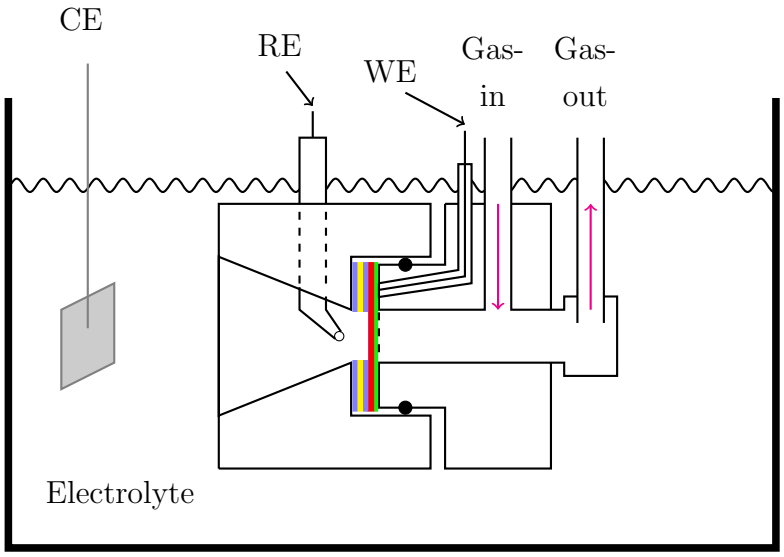

Figure 3.2.: Schematic representation of the half cell used. The electrode is shown in red, the gas diffusion layer between electrode and gas compartment/current collector is shown in green. In blue are the Ethylene Propylene Diene Monomer Rubber (EPDM) flat gaskets, in yellow the PTFE flat gasket is shown in yellow

The cell used is made of Poly(Methyl Methacrylate) (PMMA) and is placed in a heatable electrolyte tank, both to ensure constant electrolyte pressure and temperature. By using an electrolyte tank with a capacity of one liter of electrolyte, the influence of the electrolyte composition and properties is minimized and the specific variation of the electrolyte composition can be investigated. The changes that occur as a result of this variation, such as in pH, are compensated for by the use of a reversible hydrogen electrode (RHE), since this is a non-polarized electrode with a constant equilibrium potential. The potential of RHE is coupled to the pH dependent normal hydrogen electrode (NHE) via the formula:

$$U(RHE) = U(NHE) + 0,059V \cdot pH \tag{3.22}$$

The front part of the cell, which forms the transition between the working electrode and the electrolyte space, tapers conically to $1\,\mathrm{cm}^2$, which corresponds to the active area of the

working electrode. The working electrode is pressed between the two cell parts shown. To seal the cell space, a layer of two EPDM seals (blue) with a PTFE seal (yellow) in between is installed in front of the electrode on the electrolyte side. A carbon-based Gas Diffusions layer (GDL) is pressed between the working electrode and the gas chamber. The working electrode is electrically contacted via a platinum mesh located behind the gas diffusion layer. The gas flow is adjusted by a gas wash bottle connected in the gas network behind the half cell with one bubble per second. This gas wash bottle is filled with a 3 cm high water column to ensure a constant gas overpressure of 3 mbar.

3.7.2. Cell for hydrostatic pressure measurement

A cell based on the half-cell described above was developed for measurements at variable hydrostatic pressure of the electrolyte. Figure 3.3 shows a schematic drawing of the cell. The rising tube for adjusting the electrolyte pressure is shown on the left. Using this rising tube, electrolyte columns can be set between 4 cm and 40 cm, corresponding to an electrolyte pressure for 32 wt.-% Potassium Hydroxide (KOH) of 5.1 mbar to 51.3 mbar. By placing the cell within the water bath, the temperature can also be varied for this cell. The rising tube, like the rest of the half-cell, is made of PMMA and mounted to the half-cell via four screws. Sealing is provided by a EPDM O-ring.

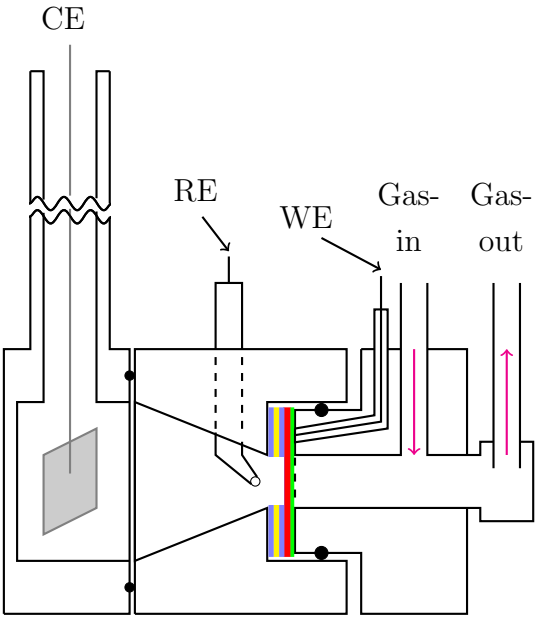

Figure 3.3.: Schematic representation of the rising tube half-cell design used. The desired hydrostatic pressure can be set via the height of the electrolyte in the rising tube on the left side of the cell. The color selection corresponds to that from figure 3.2

3.7.3. Electrical conductivity

The measurement setup shown in figure 3.4 is used to determine the through plane resistance. For the measurement, the electrode is placed between two gold-plated copper electrodes and deposited with a Sigracet GDL 29BC to represent the installation situation in the half cell as well as possible. Both copper electrodes have an area of 1 cm^2 and are each embedded in a polycarbonate body. This is used to guide the copper electrodes in order to bring both as parallel as possible to the GDE to be measured. Furthermore, a metal weight of 3 kg is placed on the upper part of the measuring cell, which ensures constant pressure and good electrical contact for all electrodes.

For the measurement, both copper electrodes are connected to a Zahner Zennium impedance system to perform an impedance measurement at constant current or voltage in the range of 100 Hz to 1 MHz.

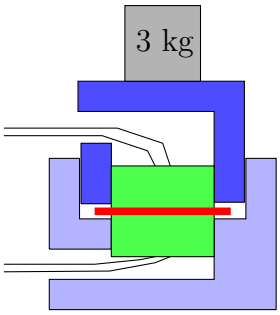

Figure 3.4.: Schematic representation of the conductivity measuring cell. The electrode (red) is clamped between two enclosed copper contacts (green). A weight, placed on the inner component in dark blue, can be used to set the desired pressure

3.7.4. Ionic conductivity

A Philips PW9512/01 measuring electrode was connected to a Zahner workstation to measure ionic conductivity. The cell consists of a glass body in which two 8 x 8 mm platinum electrodes are mounted 7 mm apart. By determining the impedance at a phase angle of 0, the ionic conductivity can be determined.

3.7.5. Gas permeability measuring cell

To determine gas permeability, the GDE was incorporated into the cell shown in Figure 3.5. The electrode is shown in red. Two flat seals above and below the GDE are used to prevent the sample gas from flowing around the electrode. The force required for sealing is realized by four screws on the top of the cell, which is made of PMMA. The measuring range of the absolute pressure transmitter as well as the differential pressure transmitter is between 0 to 1 bar, which also corresponds to the measuring range used. A laminar flow is achieved by slow flow velocities and a constant diameter of 2 cm of the bore over the entire measuring cell length, which results in the measuring range of the electrode being 3,14 cm^{-2}. Nitrogen with a dynamic viscosity of

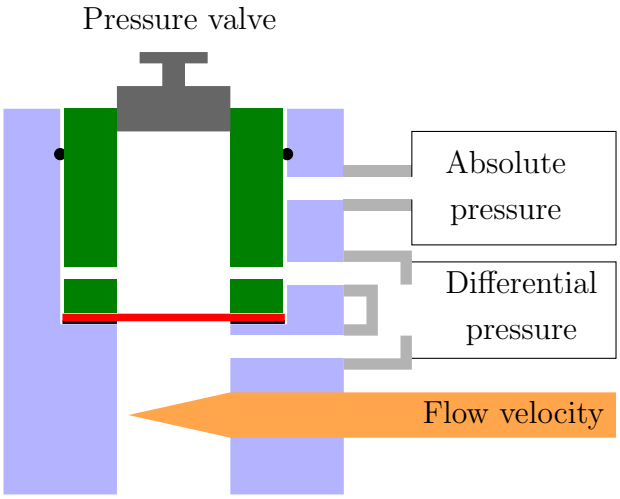

Figure 3.5.: Schematic representation of the gas permeation measuring cell. The electrode (red) is installed with a flat seal inside the gas-carrying channel

17.9 μPa at 25 °C [62] is used as the sample gas. Defined pressures can be set via the upper pressure valve.

Via Darcy's law for incompressible media [63]

$$k = -Q\frac{L}{A}\left(\frac{2(P_1 - \Delta P)}{(P_1 - \Delta P)^2 - P_1^2)}\right) \tag{3.23}$$

and from the measured values the permeability is determined. Here k is the permeability of the porous medium, L the sample thickness, A the sample area, Q the flow rate, P_1 the absolute pressure above and P_2 below the sample and ΔP the pressure difference above and below the sample.

3.7.6. Measurement of the effective ion diffusion constant

The effective diffusion rate within the fabricated electrodes depends on the tortuosity and pore distribution and significantly affects the electrochemical performance of the fabricated electrodes, depending on the penetration depth of the electrolyte into the electrode. For the measurement, the electrode is placed between two chambers with an electrolyte volume of 40 mL each with different ion concentration (see figure 3.6) and the time course of the resistance is measured, which is a function of the ion concentration according to Kohlrausch's square root law (see equation 3.24),

$$\Lambda(c) = \Lambda_0 - k * \sqrt{(c)} \tag{3.24}$$

with the molar conductivity Λ and the concentration c. The concentration can be determined via a recorded calibration line, shown in figure 3.7 a).

The first Fick's law is [64]

$$J = -D\frac{dC}{dx}, \text{ with } D = -K\frac{RT}{C} \tag{3.25}$$

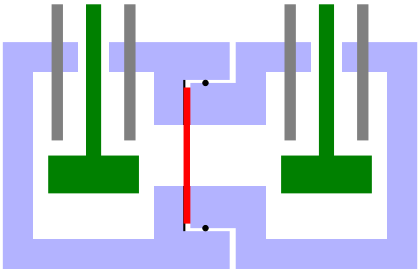

Figure 3.6.: Schematic representation of the measuring cell for determining the effective diffusion constant. The electrode (red) is installed between the two components containing the electrolyte chambers and is additionally sealed with a EPDM flat gasket. During the measurement, a uniform electrolyte concentration can be ensured in both chambers with stirrers (green). To determine the electrolyte concentration, the electrolyte resistance is measured between two nickel rods (gray)

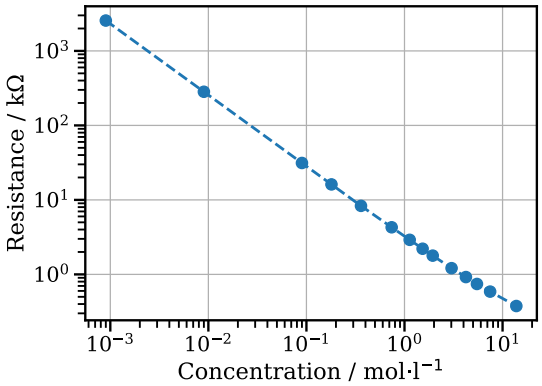

Figure 3.7.: Recorded calibration line for converting the measured resistances into electrolyte concentration

with the mass concentration C, the diffusion flux J and the constant K. By transforming equation 3.25 one obtains

$$\frac{V}{S}\frac{dC_2}{dt} = -D\frac{C_1 - C_2}{L} \tag{3.26}$$

with the cross-sectional area S, the sample thickness L, the volume V of the measuring chamber and the electrolyte concentrations C_1 and C_2 of chambers 1 and 2. The differential equation 3.26 solved with the assumption $C_2 \ll C_1$ and resolved according to the diffusion coefficient D results in

$$D = \frac{VL}{SC_1}\frac{C_2}{t - t_0}, \text{ if } C_2 \ll C_1 \tag{3.27}$$

3.7.7. Pressure saturation curve measurement cell

The intrusion cell developed for the pressure saturation curves (p-S curves) is based on the work of Gostick [65] and is made of stainless steel. An external heat source can be used to adjust the temperature of the cell and to study any temperature effects specifically. The temperature

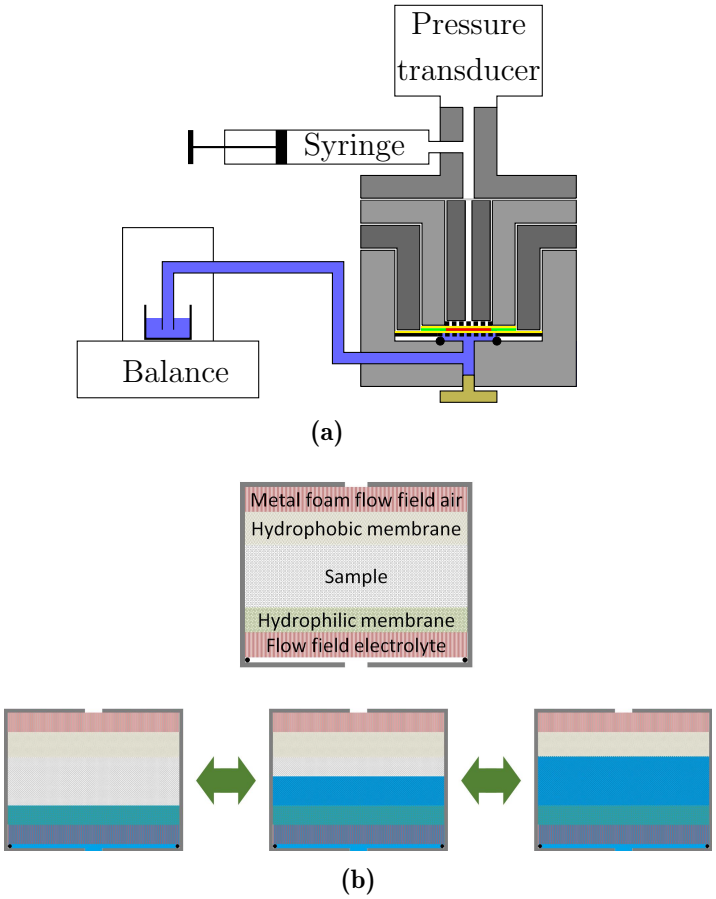

Figure 3.8.: a) Schematic representation of the intrusion measuring cell. The mass of the liquid used for the measurement is determined via a balance. A syringe on the gas side can be used to control the saturation via the gas pressure. During measurement, the electrode (red) is sandwiched between a hydrophilic membrane, which separates the liquid channel and the sample, and a hydrophobic membrane, which separates the gas chamber and the sample. Figure b) schematically shows the measuring principle, in which the measuring liquid is periodically filled in and withdrawn between the hydrophilic and hydrophobic membrane

inside the cell is determined by a heat sensor below the measuring chamber and is controlled to the set value at this point. The measuring chamber is connected to the gas section of the cell at the top and to the liquid section at the bottom. A hydrophilic membrane is installed between the sample and the liquid section. This membrane acts as a barrier to prevent gas from entering the liquid compartment. A hydrophobic membrane is installed between the sample and the gas space to prevent the liquid from entering the gas space. By using these two membranes, the measuring range can be limited to the sample under investigation. Above the hydrophobic membrane there is a metal foam which applies a uniform pressure to the membrane. This prevents the liquid pressure from pushing the membrane into the gas space and thus increasing the measuring volume of the sample space. On the other hand, the metal foam serves as an oxygen distributor to ensure a homogeneous supply and removal of oxygen during the measurement. The electrode to be measured has a diameter of 18 cm^2 and is inserted into a PTFE ring, which has an inner diameter of 18.1 mm and an outer diameter of 38 mm. The thickness of the PTFE ring here is based on the thickness of the electrode. The pressure

required to seal the cell is passed completely over the PTFE ring in the assembled state in order to avoid influencing the pore structure of the sample.

During the measurement, the gas pressure above the sample is varied via the syringe and a pressure dependent equilibrium of the degree of saturation is established. Figure 3.8 b) shows the measurement process schematically. Starting with a wet hydrophilic membrane, the pressure in the gas chamber is reduced until the set pressure limit is reached and the sample is completely filled with the measuring liquid. Then the direction of movement of the syringe is changed and the pressure in the gas chamber is continuously increased until the set limiting pressure is reached again and the sample is emptied. The p-S curves can then be calculated from the recorded values of water weight and gas pressure.

Statements about the wettability of the porous system can be made via the US Bureau of Mines (USBM) Index used in this work. This index is based on the observation that the area under a p-S curve corresponds to the work expended to inject or extract a liquid (see Figure 3.9) [65, 66].

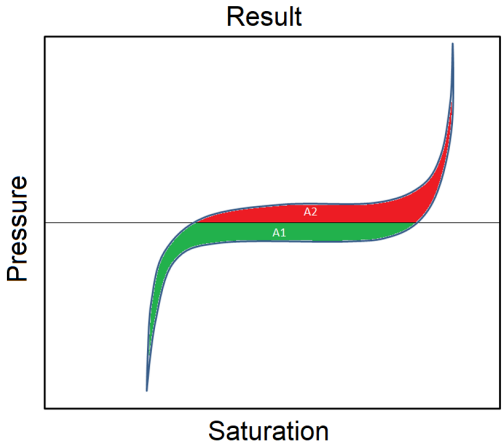

Figure 3.9.: Graphical representation of the areas used for the determination of the USBM index.

Equation 3.28 shows the mathematical definition of the USBM index,

$$I_{USBM} = log\frac{A_1}{A_2} \tag{3.28}$$

where negative I_{USBM} values represent a non-wetting material, in the case of this work a hydrophobic material, and positive I_{USBM} values represent a wetting, hydrophilic material.

3.7.8. Optical full-cell with pH monitoring

Figure 3.10 shows the cell used for in-operando UV-Vis measurements with coupled pH monitoring. The main body was made of Polyether Ether Ketone (PEEK) with an electrode spacing of 10 mm, an electrode size of 21 mm and an active area of 18 mm. Electrical contact is made by a circular platinum wire connected to two 2 mm-thick banana plugs. Both electrodes are respectively sealed on the electrolyte side with a EPDM flat gasket, and on the contact side with a PTFE flat gasket. On the gas side there is a gas connection with two 6 mm hose connections. Vertical to the electric field, centered on both electrodes, is the beam passage for optical

measurement. Two optical windows made of quartz glass (Thorlabs WG41010R UVFS 25x36, 1mm thick) separate the electrolyte chamber from the environment. The optical fibers are integrated into the cell holder. Two optical fiber connectors with integrated collimator lenses are used.

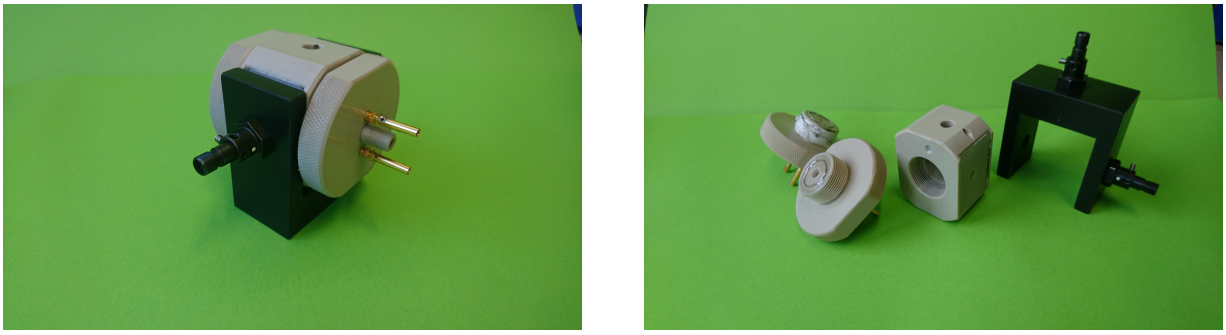

(a) **(b)**

Figure 3.10.: a) The assembled optical cell for UV-Vis measurements, b) shows the individual components of the cell

4. Peer reviewed publications for cumulative doctoral thesis

This is a cumulative doctoral thesis based on four articles which were published after a peer-review process.

Article I:
A segmented cell measuring technique for current distribution measurements in Zn-air batteries,
A. Kube, J. Meyer, D. Kopljar, N. Wagner and K. A. Friedrich
Journal of the Electrochemical Society, Volume 168, Issue 12, 120530 (2021)
doi: 10.1149/1945-7111/ac4059
Contribution Alexander Kube: concept, supervision of experimental work, evaluation and writing. Rebuttal during peer-review process.

Article II:
Evaluation of electrochemical impedance spectra of metal-air batteries (Li-air/Zn-air) for aqueous electrolytes,
A. Kube, W. Strunz, N. Wagner and K.A. Friedrich
Electrochimica Acta, Volume 396, 139261 (2021)
doi: 10.1016/j.electacta.2021.139261
Contribution Alexander Kube: concept, GDE production, experiments, evaluation and writing. Rebuttal during peer-review process.

Article III:
Influence of organic additives for zinc-air batteries on cathode stability and performance,
A. Kube, N. Wagner and K.A. Friedrich
Journal of Electrochemical Society, Volume 168, Issue 5, 050531 (2021)
doi: 10.1149/1945-7111/abff63
Contribution Alexander Kube: concept, GDE production, experiments (except gas chromatography, SEM), evaluation and writing. Rebuttal during peer-review process.

Article IV:
Influence of Cycling onto electrolyte distribution inside a silver-based gas diffusion electrode for Zn-Air batteries,
A. Kube, N. Wagner and K.A. Friedrich
ACS Sustainable Chemistry, Volume 10, Issue 51, 17107-17115 (2022)

doi: 10.1021/acssuschemeng.2c04542
Contribution Alexander Kube: concept, GDE production, experiments (except current distribution map, SEM), evaluation and writing. Rebuttal during peer-review process.

Journal of The Electrochemical Society, 2021 **168** 120530

A Segmented Cell Measuring Technique for Current Distribution Measurements in Batteries, Exemplified by the Operando Investigation of a Zn-Air Battery

Alexander Kube,[1,z] Jens Meyer,[1] Dennis Kopljar,[1] Norbert Wagner,[1] and Kaspar Andreas Friedrich[1,2,*]

[1] *German Aerospace Center, 70569 Stuttgart, Germany*
[2] *University of Stuttgart, Institute of Building Energetics, Thermal Engineering and Energy Storage (IGTE), 70569 Stuttgart, Germany*

A transimpedance amplifier circuit as well as an instrumental amplifier circuit were used to measure current densities of a zinc-air battery with an integrated segmented current collector foil. Error calculation showed that the transimpedance amplifier is superior to the used instrumental amplifier, but both methods provide valuable and consistent results. They both showed comparable results with operando insight into the current distribution of the battery. The knowledge about those distributions is essential to avoid fast degradation of battery materials and irreversible capacity loss due to heterogeneous dissolution of the anode during discharge. In this work we showed that oxygen starvation as well as gas flow rate leads to large current gradients. It was also demonstrated that heterogeneous current distributions on cathode side induces also a heterogenous dissolution behavior on the anode, resulting in irreversible capacity loss.

 [DOI: 10.1149/1945-7111/ac4059]

Manuscript submitted October 20, 2021; revised manuscript received November 22, 2021. Published December 20, 2021.

Supplementary material for this article is available online

The transition from fossil fuel resources to technologies based on renewable energy is hampered by the lack of cost-effective grid-connected storage solutions. Still, an internalization of the external cost associated to the environmental impact of fossil fuel use is not foreseen. While renewable electricity is nowadays cost competitive to fossil energy production in many parts of the world and slowly displacing conventional generation, the attention is continuously shifting towards energy storage solutions. For short-term storage (<1 h for grid service) lithium-ion batteries are currently the technology of choice as they exhibit a good compromise between energy density and cost which has been dropping significantly over the last decades due to advances in cell and production technology as well as economy of scale. However, concerns in terms of safety, resource availability and sustainability have led to efforts to find alternatives. One particularly promising alternative is the zinc-air battery owing to its high theoretical energy density of 1353 $Wh \cdot kg^{-1}$ (excluding oxygen) from which a practical energy density of 300 $Wh \cdot kg^{-1}$ is suggested to be realistic for primary button cells,[1] low cost below 100 \$ $kW \cdot h^{-1}$ due to the use of low cost and abundant materials and inherent safety.[2] Although they are a mature technology already commercialized as primary batteries further development is needed to enable rechargeable Zn-air technology.[3] Great efforts and improvements are made on the catalyst development increasing cycle life and lowering over potentials.[4–7] Cycle life is also limited by precipitation of carbonates inside the cathodes porous system.[6,8] To minimize carbonate formation near neutral electrolytes[9–11] and ionic liquids are investigated lately.[8,12,13]

The critical component of the Zn-air battery is the gas diffusion electrode where oxygen reduction (ORR) and evolution (OER) proceeds during discharge and charge, respectively. During ORR, the co-existence of gaseous and liquid phase inside the electrode is essential to provide effective transport of the gaseous O_2 to the active sites wetted by the liquid electrolyte. Reaching and maintaining an optimal balance of wetting degree inside the electrode is therefore crucial but challenged by several factors during operation of the battery:

First the wetting changes during charge and discharge. Due to the volume increase of the zinc anode during discharge by a factor of 1.6 due to the conversion of zinc to zinc oxide, electrolyte might be pressed inside the porous system of the cathode, leading to a decreased active surface area between gas and liquid phase because of gradual flooding of the electrode structure. Importantly, during charging (OER) of the cell oxygen bubbles are evolved which isolates active areas in the cathodes porous system until the bubble are released.[14] Beside the effects of interaction between the electrodes and the gas evolution during OER the operation conditions especially the ambient humidity of the feed gas may change the water saturation level of the porous system of the cathode. If the ambient humidity is greater than the equilibrium relative humidity inside the Zn-air battery, water will be absorbed and might flood the porous system of the cathode. On the other hand, if ambient humidity is lower than the equilibrium humidity, the battery cell might dry out.[15]

The wetting is further subject to local variations owing to the cell architecture. By using a vertical cell design, the hydrostatic pressure is higher at the bottom of the cell and less at the top, which alters the electrolyte pressure onto the porous system of the cathode, resulting in inhomogeneous penetration depths along the electrode height. The anode suffers from these gravimetrical effects as well as due to a complex reorganization of material to the cell bottom during stripping and plating of the zinc.

The effects on the GDE can be avoided by specially designed cathodes with a gradient in pore size structure and/or in the hydrophobic agent distribution to accommodate for pressure differences.

Finally, unlike the fuel cell design, where current is transported through bipolar plates, Zn-air cells often use the cathode itself for current transport, which results in inhomogeneous current distributions over the electrode length due to ohmic losses.[16]

All of these effects lead to changes in the current distribution and inhomogeneous stress along the electrode geometry, which might affect electrochemical performance and accelerate the observed degradation mechanisms. A more elaborate understanding of these mechanisms phenomena and a visualization can help in optimizing components and cell design to identify where the components have to be improved.

*Electrochemical Society Member.
[z]E-mail: alexander.kube@dlr.de

A particularly powerful method to obtain information on inhomogeneities in operation and to elucidate local degradation is the use of the so-called segmented cell technique which is based on the use of segmented current collectors and printed circuit board technology. In contrary to post-mortem analysis of the electrode, this technique allows locally-resolved electrochemical measurements and can be performed during cell operation. This information is only accessible through simulation so far.[17] This method was first introduced for the application in fuel cell systems and since then extended for investigation of proton exchange membrane (PEM) and alkaline electrolysers as well as redox-flow batteries. For example, Sanchez et al. investigated the influence of temperature and humidification onto the performance of polymer electrolyte membrane fuel cells (PEMFCs)[18–21] and showed the feasibility of such investigations with the segmented cell technology. Segmented cells were also used to investigate Vanadium Redox Flow batteries to measure current distribution on electrode level and Li-Ion batteries on stack level.[19,22–27]

Numerous possible solutions to measure current distributions are reported in literature: the measuring of current distribution can be realized by several approaches such as measuring the voltage drop over a defined resistor or by using hall sensors. Both approaches are costly, prone to measurement errors and need a lot of time setting up the measurement.[28,29] Using printed circuit boards (PCB) shows less measurement errors and is very flexible in design but additional space is required due to the thick board inside the cell as well as on the equipment side where a multiplexer and digital multimeter are needed.[22,23,30]

In our work we use an approach with a segmented current collector printed onto a PEEK foil in which the gold segments are individually contacted to the external circuit. Additionally, the foil is very flexible and easy to process and the design can be easily adjusted to the specific needs. In principle, a dedicated and reduced segmentation can be implemented to monitor the behavior during operation, e.g. at positions which have been shown to degrade fastest. A more detailed explanation on the technique is given in sections cell assembly and segmented cell technique. Direct temperature measurements are not implemented so far, which is commonly used when using the PCB approach. Only indirect measurement via electrochemical impedance spectroscopy (EIS) can be performed with our setup.

By combining locally resolved impedance measurements and current distributions, the cause for local changes in the current density and the underlying degradation phenomena can be identified, further enhancing the possibilities and benefit of the segmented cell technology even further.[31,32]

The focus of this work is the validation of the new setup on Zn-Air battery cathodes and to establish the method for evaluation of metal-air batteries in general. The investigation as exemplary study demonstrating its feasibility. The influence of gas flow variations on how gas flow variation influences the uniformity of current density on such electrodes is investigated. In addition, it is shown how heterogeneous current distributions on the cathode side leads to equivalent non-uniform dissolution of the anode.

Materials and Methods

Electrode preparation.—Silver (Ag) electrodes consisting of 90 wt.% Ag (Ferro AG, type 311) and 10 wt.% PTFE (TF9207Z, 3 M Dyneon) were produced. For this purpose, the powders were physically mixed in a knife-mill, filled into a mossy frame and pressed at 300 kN m^{-2} for 1 min in a hydraulic press together with a metal mesh (0.125 mm, Haver & Boecker). After removal of the frame the electrode was pressed again using the same parameters. To achieve a mechanical stable electrode, it was heat treated in an oven

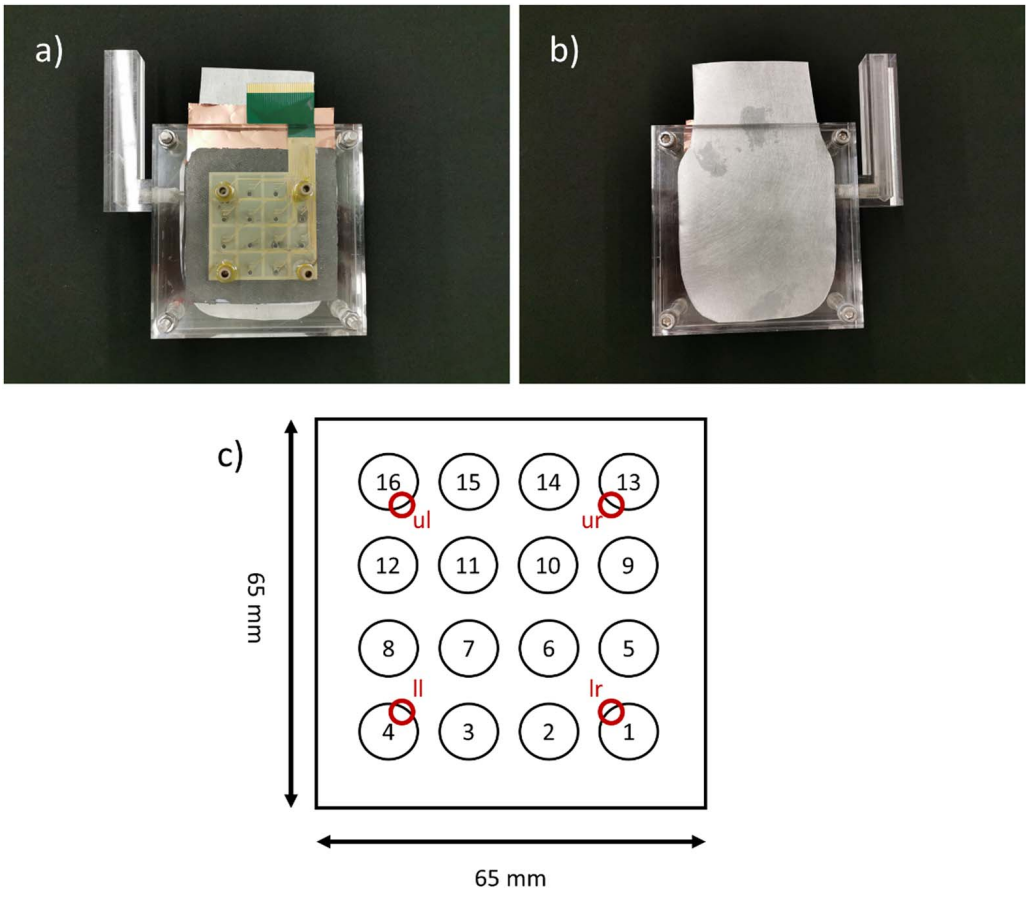

Figure 1. (a) and (b) show the assembled test cell, (c) shows the segment numbers and the gas inlets (upper left, ul; upper right, ur; lower left, ll; lower right, lr) referred to in this work.

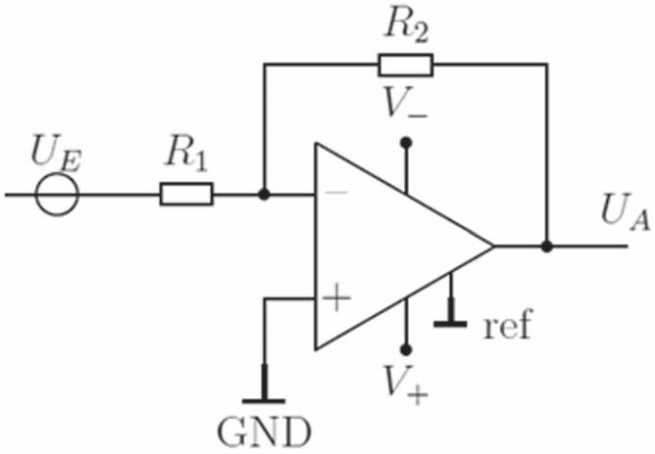

Figure 2. Circuit diagram of a transimpedance amplifier.

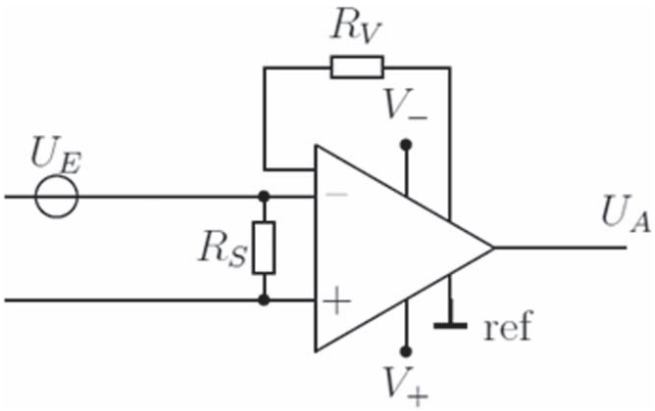

Figure 3. Circuit diagram of an instrumental amplifier.

for 1 h at 340 °C as described by Wittmaier et al.[33] A punching tool with a diameter of 12 mm was used to obtain the electrodes for cell assembly. Ag was used as catalyst due to its high activity and thus, to avoid effects ascribed to inhomogeneous electrode performance.

Gas diffusion layer preparation.—80 wt.% Timcal Timrex T150 with 20 wt.% PTFE (TF9207Z, 3 M Dyneon) were physically mixed using a knife mill for 30 s. The powder mixture was filled into a frame, calendared at 30 Kg and heat treated for 1 h at 340 °C.

Cell assembly.—The test cell was build using Poly(methyl methacrylate) (PMMA). It consists of a solid back plate on the anode side, a ring-shaped electrolyte compartment with a thickness of 1 cm and a plate with four connections for gas supply. The gas supply is placed at the four electrode corners (see Fig. 1).

A zinc foil (250 μm thick) was used as anode. The produced Ag electrodes were pressed into a PTFE frame and mounted into the cell, together with the GDL and the segmented current collector. As segmented current collector a PEEK foil (100 μm thickness) with printed gold contacts (40 μm thickness) was used. Airflow was realized through the segmented current collector by four holes marked in Fig. 1c as red circles.

The cathode consisted of the 12 mm Ag electrodes pressed inside a 0.5 mm thick PTFE frame. Between the electrolyte and the cathode assembly a rubber foil and a PMMA plate, both with 11 mm holes were mounted. This was done to better seal the edges of the cathodes and provide homogenous pressure onto the cathode to reduce contact problems.

The cell was either operated with ambient air or pure oxygen. The gas flow was led to a 3 cm high water column and set to 1 bubble per second. Compared to fuel cells, batteries exhibit much lower currents densities and therefore a homogenous gas distribution can be achieved more easily. As a consequence, no forced convection by pumps is necessary, however, a sufficient gas supply is mandatory which was accomplished by providing enough gas inlets/holes. In our case up to four inlets were integrated.

Segmented cell technique.—Due to the fact, that potential can be measured more precisely than current, a core element of the segmentation diagnostics is the current to potential conversion. In this work it was carried out by using two different kinds of operational amplifiers (OpAmp) circuits. The transimpedance amplifier (TIV) and the instrumental amplifier (InAmp). The following part is divided into the description of the setup, the functionality and the main advantages and disadvantages of the certain amplifier circuits.

Transimpedance amplifier (TIV):

The TIV, depicted in Fig. 2 is an inverted amplification circuit, based on the signal source being connected to the inverted input. U_E describes the input and U_A the output signal. All existing resistances before the inverted input are condensed in an equivalent resistor R_1. R_2 is the feedback resistor. The negative input is called inverted and the positive none inverted. $\perp$ symbolizes ground potential (GND). The bipolar potential source of the operational amplifier is marked by V_- and V_+.

The non-inverted input is connected to ground (GND). As a consequence of the non-inverted input being connected to GND and the input potentials are set to the same potential both input signals and the output potential U_A share the same potential. An incoming potential coming from the input (U_E) increases the potential according to the ohmic law. The current flow through the feedback resistor R_2 is connected to an internal circuit of the amplifier and with this is connected to the negative power source. The amplifier evens out the amplified potential by supporting a current flow over the feedback wiring to V_-. As a consequent there is a potential drop at the amplifier output U_A. The resistor R_2 and the new output potential U_A results in an equivalent current compared to the input current. These currents balance each other out at the inverted input. The amplifier maintains the potential between the potential source and the inverted input. Since the potential drop of R_2 is controlled by the operational amplifier, the signal source is not being influenced by R_2 which avoids errors commonly present with shunt resitors setups.

The amplification is calculated with the following formula:

$$U_A = -U_E \cdot \frac{R_2}{R_1} \quad [1]$$

Instrumentation amplifier (InAmp):

The InAmp is a differential amplifier (Fig. 3). U_E describes the input and U_A the output signal. R_S describes the shunt resistor and R_V the setting resistor. $\perp$ symbolizes ground potential (GND). The bipolar potential source of the operational amplifier is marked by V_- and V_+.

The current from the signal source is flowing through the shunt resistor R_S. There is a potential drop over the resistor dependent on the incoming current and the resistor value, which is measured by the OpAmp. The potential then is amplified by a factor, which is determined by the setting resistor R_V. The output potential is raised respectively. Table I gives an summary and comparison of the TIV and InAmp circuit.

The above described characteristics of both circuits determine the sources for errors. These errors were calculated by error propagation (see supporting information) and showed an approximately 10 times smaller error for the TIV. This is mostly due to the shunt and variable resistors. In the following experiments the TIV is mainly used because of the lower errors.

Measurement techniques.—A Zahner electric Im6 equipped with 4 PAD4 (Parallel Analog-Digital 4) cards for parallel voltage measurements was used to record the current distributions. During

Table I. Comparison of the advantages (pro) and disadvantages (con) of both the InAmp and the TIV setup.

	TIV	InAmp
Pro	•The measured signal source is not being influenced by a sense resistor. •Only one resistor is needed.	•The measurable current range is only restricted by the temperature dependence of the resistor.
Con	•The measurable current and potential range is limited by the OpAmp. •OpAmp which are designed for current ranges higher than 100 mA are expensive.	•The shunt resistor contributes to signal source error. •A minimum of two resistors is needed. The error tolerance assigned to the resistors propagate through the shunt- and amplification resistor.

charge and discharge constant currents were applied and the sampling rate was set to 2 s.

Results and Discussion

Influence of electrolyte level.—For the validation of the setup, an experiment with a variation of the electrolyte level which leads to a varying amount of electrochemically active electrode segments was performed and the current distribution was measured. Furthermore, two different types of operational amplifier circuits were compared in their ability to measure and resolve currents from the segmented current collector. The aim was to identify an electronic design with signal of high quality and resolution. For a description of the circuits with the corresponding features, see section segmented cell techniqu.

Figure 4 shows the comparison of the transimpedance amplifier (TIV) and the instrumentation amplifier (InAmp) circuit board connected to the cell for an increasing electrolyte level. 16 electrically isolated silver electrodes were used in a 4 × 4 arrangement. The electrolyte level was raised 4 times (15 mm, 30 mm, 45 mm, 65 mm), with each level adjusted to fully contact the next row of electrodes and the current distribution was recorded at a fixed current of 160 mA. Since the electrochemical reaction can only take place where electrolyte is in contact with the electrodes, the applied current will flow through the wetted electrode segments. This results in locally high current densities (depicted in yellow) for low electrolyte levels, as the total current is fixed for all measurements. When the electrolyte level is raised up to the next row of electrodes the contacted segments become active leading to a more homogeneous current distribution. At full contact deep blue regions vanish and the overall current distribution is homogeneous with modest local current densities. As expected both circuit boards show this behavior demonstrating the functionality of the setup.

While the TIV and the InAmp circuit show comparable results for an electrolyte level of 15 mm and 65 mm, both electrolyte levels of 30 mm and 45 mm show some deviations. The formation of a homogeneous current distribution seems to be better for the TIV circuit. Especially in the center region of the InAmp circuit measurement only low currents were recorded. The use of 16 single electrodes placed in the PTFE frame could inflict contact problems since during mounting the electrodes it was not possible to place them completely in plane with the PTFE frame. This can be seen for the InAmp circuit at segment 6 (cf Fig. 1 red circle), which always shows very low currents, e.g. for the fully filled cell segment 6 shows around 6 mA compared to 10 mA at the other electrodes. In further studies this electrode arrangement consisting of 16 single electrodes will be replaced by one electrode which covers the whole measured area. In this respect it has to be mentioned that for all segmented measurement techniques the local resolution is determined by the in-plane electric conductivity which counteracts the heterogeneity of current distributions. Since silver exhibits very high electronic conductivity we needed to have an insulating frame. The following results in the following figures were recorded with the TIV set up.

Influence of gas supply location.—To further validate the setup and demonstrate its capabilities, the effect of gas supply location was investigated. To this end, three gas ports were sealed (Fig. 5 red crosses), only the gas port at the lower right was left open (Fig. 5 green circle). Figure 5 shows the current distribution at the start of the measurement (left figure) and the normalized current distribution at the end of the measurement after reaching 0.5 V vs Zn (right figure). The normalization was done by subtracting the initial current distribution from the current distribution of interest and was done to better identify changes between start and operation and to mitigate small deviations in the initial state most probably ascribed to contact problems. During the measurement a clear shift of current to the lower right corner with the open gas port can be identified while the rest of the electrode shows a decrease of current indicating the depletion of oxygen and therefore lower reaction rates. The three corners with closed gas inlets still show higher current densities than the center of the electrode. This could be explained by diffusion of oxygen through the sealing.

Influence of gas flow rate.—To investigate the influence of the flow rate in more detail, the flow was increased 3-fold from 0.065 ml s^{-1} increased to 0.327 ml s^{-1} and set back to the initial 0.065 ml s^{-1}. At each rate the flow rate was maintained for 2 min. The flow direction was adjusted by using only one gas port as inlet and another one as outlet. Accordingly, the gas flowed either from the lower right (lr) to the upper right (ur), or from the upper left (ul) to

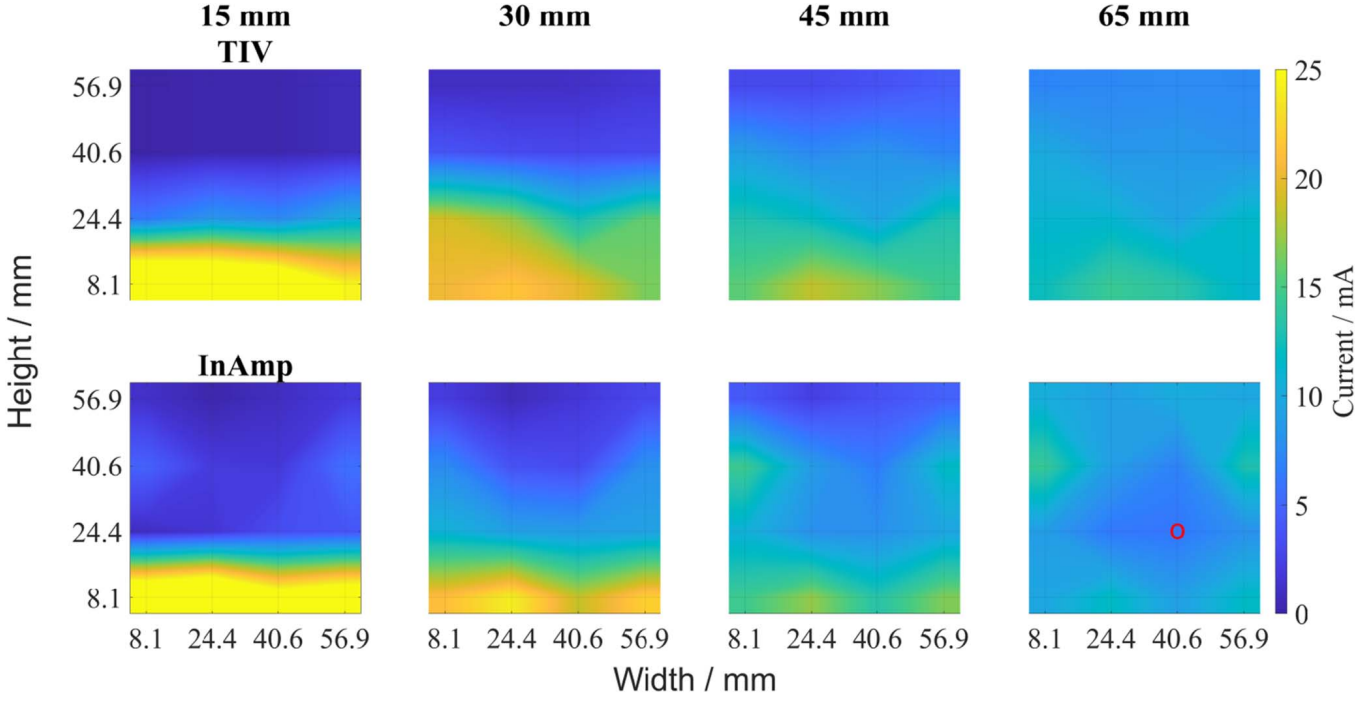

Figure 4. Variation of electrolyte level for the transimpedance amplifier (TIV, top) and the instrumental amplifier (InAmp, bottom). The red circle marks segment 6.

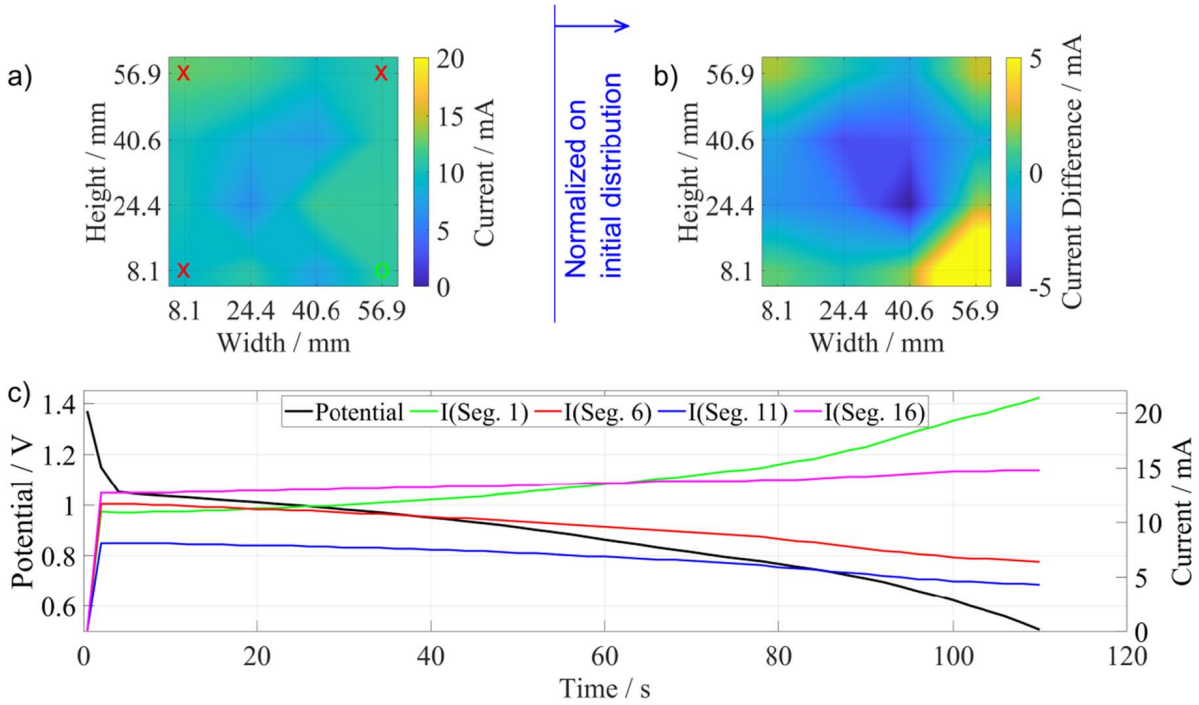

Figure 5. Influence of gas distribution if only the gas port at the lower right (green circle) is open for the transimpedance amplifier (TIV). The red crosses mark the closed gas ports. The current distribution in figure (b) shows the normalized current distribution at t = 110 s. Figure (c) shows the current over time.

the lower left (ll), respectively. Both tests were done on the same setup including the same electrodes. First the gas flow was set to the right side (lr→ur) and afterwards to the left side (ul→ll). The results are shown in Fig. 6.

The current distribution at t = 0 shows an acceptable homogeneity. For the gas flow from lower right (lr) to the upper left (ul), segment 16 (upper left corner) shows a slightly higher current than the other segments which is ascribed to the position of the inlet (Fig. 6 upper line). This effect increases with the increase of the flow rate as can be seen in the middle figures for high gas flow rate. For the flow on the right side the reaction shifts to the left, while for flow on the left side the reaction shifts to the right. In our setup the gas flowed through the GDL which inflicts resistance to the gas flow and therefore led to increased gas pressures for higher flow rates. The

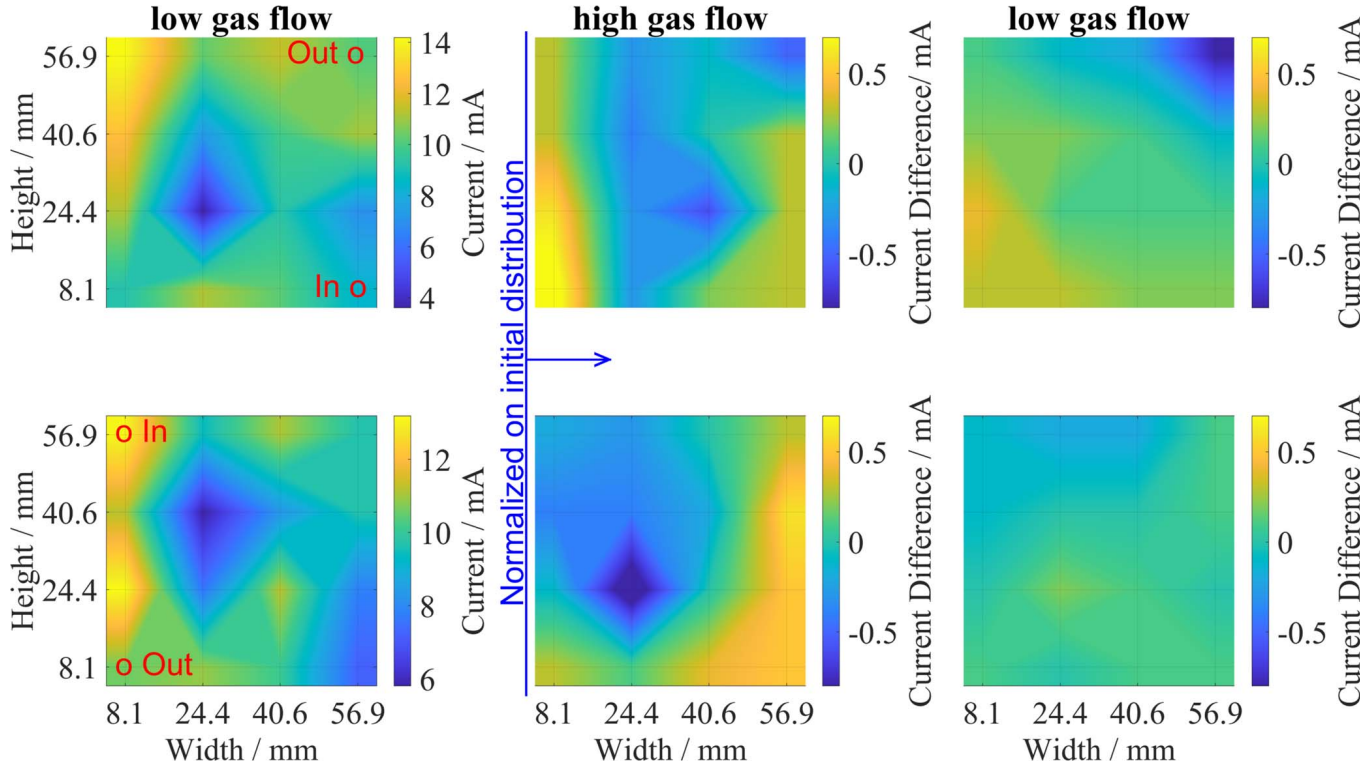

Figure 6. Variation of gas flow rate for the transimpedance amplifier. Upper figures show gas flow from lower right (lr) to upper right (ur), lower figures the gas flow from upper left (ul) to lower left (ll). Both left figures show the initial distribution after 2 min of gas flow. All other diagrams are normalized to this initial distribution.

increased gas pressure shifts the location of the three-phase boundary away from the gas towards the electrolyte side of the GDE, thereby reducing the electrochemically active surface area. After reducing the gas flow again to the initial value, the current distribution levels off and exhibits a more homogeneous distribution again. This can be seen clearly for the ul→ll test while for the lr→ur test the initial state was not achieved again. For all segments a small drop in current density was observed after around 1 min (see Fig. S1 in supp. Information (available online at stacks.iop.org/JES/168/120530/mmedia)). This drop might explain the deviation from the initial state as the system might not have been in equilibrium state. This is because changes in current density also lead to changes in the surface coverage with reactants as well as changed electrolyte saturation of the surface due to changed electrowetting.

It has to be mentioned, that the pressure inside the porous system which builds up as a result of the change in the gas flow is more severe than what is commonly observed for membrane electrode assemblies (MEAs) in fuel cells. The cell used in this study did not have a flow field, but instead uses gas ports which lead the gas directly through the GDL. Flow fields could homogenize the gas pressure throughout the channel system, and reduce the pressure inside the porous structure as the gas would not have to be transported through the GDL to its full extent. An additional difference is the thickness of MEAs compared to our electrodes. That said, the presented technique can serve as a valuable tool in evaluating and optimizing cell design and flow-field structure in future work.

The observed current inhomogeneities cause heterogeneous aging. For fuel cells such degradation investigations were carried out by e.g. Durst et al. and showed that fuel starvation under the land compartment of the flow field leads to decreased degradation.[34] This is because oxygen has to diffuse from areas with channels to areas without channels. In our case the forced heterogeneous gas distribution has the same effect. In areas with low concentration of reactant lower reaction rates are present, whereas in areas with sufficient supply of oxygen the current densities are high. These regions show faster degradation.

Influence of heterogenous cathode current distribution on anode dissolution.—Inhomogeneities on the cathode side might also inflict inhomogeneities on the anode side. These inhomogeneities can be due to several reasons like gas flow and distribution, as it was shown above but also due to different penetration depths of electrolyte in the porous system. The wetting behavior affects the active surface inside the porous electrode. To investigate the influence of inhomogeneities on the anode, the battery was discharged to 0.5 V vs Zn. The current was set to 240 mA and the gas flow was set from both lower gas ports to both upper gas ports. The result is depicted in Fig. 7. The first row shows the normalized state at 2.78 h and was used to normalize the current distribution for better visualization of changes, as at this point the system was in a stable condition (the non-normalized distribution can be found in the supporting information Fig. S3). Row 2 shows the result at the first visible hole in the anode at 7.37 h. This is accompanied by a shift of current to the bottom of the cell where the anode is still intact. At 9.43 h the hole in the anode grew larger and the current shift to the bottom has advanced further. At the end of the test (11.5 h) the anode is almost completely dissolved and the cathode can be seen through the cell. A potential and current diagram over time is shown in the SI in Fig S4.

The faster dissolution of the anode is due to higher currents at the top of the cell. Reason for this might be either the hydrostatic pressure of the electrolyte or the pressure induced by the gas flow. The influence of the gas flow was investigated in Fig. 5. As we used the low flow rate from bottom to top on both sides the influence of the gas flow rate onto the current distribution should be negligible. The hydrostatic pressure on the other hand inflicts higher electrolyte pressure at the bottom of the cell and therefore higher penetration depths. This reduces the active area and therefore has a similar effect than the high gas flow rate would show.

This inhomogeneous dissolution of the anode hinders high cycle life since the structure of the anode is disintegrated at some areas, while on others is still intact. During charging inhomogeneous currents inflict higher local currents resulting in dendrite growth,[3] which short circuits the battery.

Parker et al. proposed a structured zinc sponge consisting of zinc with interconnected pores in between. The capacity of such electrodes cannot be used completely since a backbone structure is needed to precipitate metallic zinc during charging back onto the structure. Inhomogeneous current distributions during discharge, like observed by us, would destroy such host structures resulting in reduced capacity and cycle life.[3,35,36] The loss of usable zinc is accompanied by gravimetrical forces in vertical cells, like the one used by us. This is due to the reaction pathway where first zinc hydroxide is formed. After reaching the solubility limit zinc oxide formation takes place. Therefore, the current distribution should be optimized to accommodate for hydrostatic pressure influences on cathode side as well as gravimetrical forces on anode side.

Conclusion

Two different kinds of operational amplifiers (OpAmp) circuits were shown and compared to measure a segmented current collector printed on a thin foil. The transimpedance amplifier circuit showed smaller errors than the instrumental amplifier circuit, as shown by error calculation. To verify both amplifier circuits the electrolyte level was slowly filled and the resulting current distribution was measured, showing that both amplifier circuits can give valuable in-operando information about the system. The used cell setup already showed good current homogeneity.

The influence of the gas distribution and the flow rate was investigated. For this only one gas port was left open and the oxygen starvation was observed in the rest of the cell, showing that enough gas access points must be provided for good current homogeneity. Variation of gas flow rates showed that a low flow rate gives a smoother current distribution than higher flow rates. This is probably due to the higher gas pressures inflicted by the flow through the porous system which reduces the electrolyte saturation level inside the porous system and therefore the active area on the side of the high gas flow.

In a last experiment the influence of non-uniform current distribution on the cathode side on the dissolution rate on the anode side was investigated. It was shown that due to higher currents on the upper part of the cathode the anode dissolved faster in this area. This inhomogeneous dissolution inflicts lower cycle life due to the loss of host structures to reprecipitate the zinc.

In further investigation the influence of humidification and aging must be further investigated with this cell setup and a modified version with a flow field. A heterogeneity of material degradation (GDL, GDE, Anode) needs to be considered as well for further studies and has to be examined.

As conclusion it can be mentioned, that the knowledge about current distributions can be used for material development, performance enhancement, investigation of degradation, cell and flow field development and optimizing operating conditions. This setup can be used in other battery applications like Li-Ion and metal-sulfur batteries as the shown setup can accurately measure the low current densities used and can therefore be used for system and material development in these as well.

Acknowledgments

This research was supported by funding of the DLR in the frame of the project “Next Generation Car.”

ORCID

Alexander Kube https://orcid.org/0000-0002-8042-326X

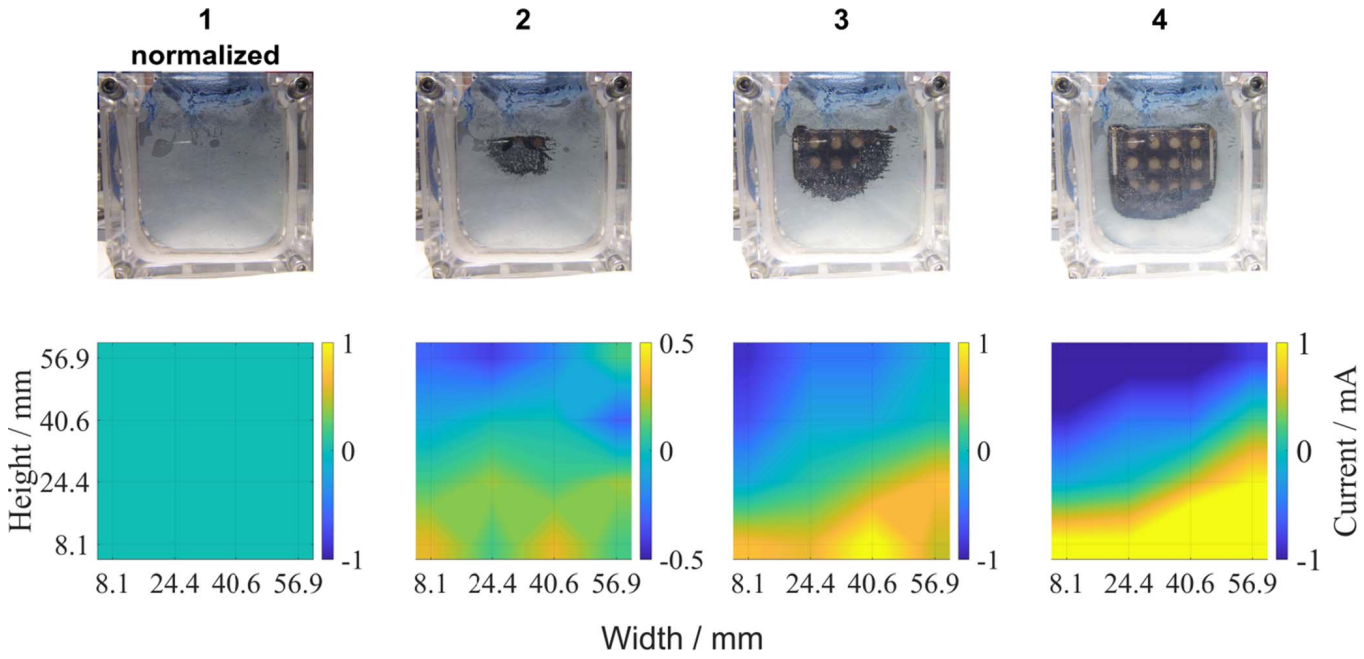

Figure 7. Discharge of Zn-air battery until 0.5 V vs Zn. Upper figures show the anode at 2.78 h (1), 7.37 h (2), 9.43 h (3) and 11.5 h (4). Lower figures show the corresponding current distributions on cathode side.

Norbert Wagner https://orcid.org/0000-0002-2596-8689
Kaspar Andreas Friedrich https://orcid.org/0000-0002-2968-5029

References

1. J. Stamm, A. Varzi, A. Latz, and B. Horstmann, *J. Power Sources*, **360**, 136 (2017).
2. J. Zhang, Q. Zhou, Y. Tang, L. Zhang, and Y. Li, *Chem. Sci.*, **10**, 8924 (2019).
3. S. Hosseini, S. Masoudi Soltani, and Y.-Y. Li, *Chem. Eng. J.*, **408**, 127241 (2021).
4. H.-X. Zhong, J. Wang, Q. Zhang, F. Meng, D. Bao, T. Liu, X.-Y. Yang, Z.-W. Chang, J.-M. Yan, and X.-B. Zhang, *Advanced Sustainable Systems*, **1**, 1700020 (2017).
5. F. Meng, H. Zhong, J. Yan, and X. Zhang, *Nano Res.*, **10**, 4436 (2017).
6. F.-L. Meng, K.-H. Liu, Y. Zhang, M.-M. Shi, X.-B. Zhang, J.-M. Yan, and Q. Jiang, *Small*, **14**, 1703843 (2018).
7. F. Meng, H. Zhong, D. Bao, J. Yan, and X. Zhang, *J. Am. Chem. Soc.*, **138**, 10226 (2016).
8. Wei Sun, Fei Wang, Bao Zhang, Mengyi Zhang, Verena Küpers, Xiao Ji, Claudia Theile, Peter Bieker, Kang Xu, Chunsheng Wang, and Martin Winter et al., *Science*, **371**, 46 (2021).
9. A. Kube, N. Wagner, and K. A. Friedrich, *J. Electrochem. Soc.*, **168**, 050531 (2021).
10. S. Clark, A. R. Mainar, E. Iruin, L. C. Colmenares, J. A. Blázquez, J. R. Tolchard, Z. Jusys, and B. Horstmann, *Adv. Energy Mater.*, **10**, 1903470 (2020).
11. A. Sumboja, X. Ge, G. Zheng, F. W. T. Goh, T. S. A. Hor, Y. Zong, and Z. Liu, *J. Power Sources*, **332**, 330 (2016).
12. Peng Chen, Keyi Zhang, Dejian Tang, Weilin Liu, Fancheng Meng, Qiuwei Huang, and Jiehua Liu, *Frontiers in Chemistry*, **8**, 372 (2020).
13. P. Ingale, M. Sakthivel, and J. F. Drillet, *J. Electrochem. Soc.*, **164**, H5224 (2017).
14. K. Wang, P. Pei, Z. Ma, H. Chen, H. Xu, D. Chen, and H. Xing, *J. Power Sources*, **296**, 40 (2015).
15. P. Pei, K. Wang, and Z. Ma, *Appl. Energy*, **128**, 315 (2014).
16. P. Pei, Z. Ma, K. Wang, X. Wang, M. Song, and H. Xu, *J. Power Sources*, **249**, 13 (2014).
17. M. Xiong, M. Alipour, and D. G. Ivey, *ECS Trans.*, **85**, 769 (2018).
18. D. G. Sanchez, T. Ruiu, K. A. Friedrich, J. Sanchez-Monreal, and M. Vera, *J. Electrochem. Soc.*, **163**, F150 (2015).
19. D. G. Sanchez, T. Ruiu, I. Biswas, M. Schulze, S. Helmly, and K. A. Friedrich, *J. Power Sources*, **352**, 42 (2017).
20. Y. Wang et al., *J. Power Sources*, **449**, 227542 (2020).
21. N. Rajalakshmi, M. Raja, and K. S. Dhathathreyan, *J. Power Sources*, **112**, 331 (2002).
22. J. T. Clement, D. S. Aaron, and M. M. Mench, *J. Electrochem. Soc.*, **163**, A5220 (2015).
23. T. Gerber, P. Fischer, K. Pinkwart, and J. Tübke, *Batteries*, **5**, 15 (2019).
24. G. Zhang, C. E. Shaffer, C.-Y. Wang, and C. D. Rahn, *J. Electrochem. Soc.*, **160**, A610 (2013).
25. A. Phillips, M. Ulsh, J. Porter, and G. Bender, *Fuel Cells*, **17**, 288 (2017).
26. S. J. C. Cleghorn, C. R. Derouin, M. S. Wilson, and S. Gottesfeld, *J. Appl. Electrochem.*, **28**, 663 (1998).
27. M. W. Kim, M. J. Son, H. Park, J. Y. Park, and H. T. Lim, *Fuel Cells*, **20**, 212 (2020).
28. M. Schulze, E. Gülzow, S. Schönbauer, T. Knöri, and R. Reissner, *J. Power Sources*, **173**, 19 (2007).
29. S. V. Erhard et al., *J. Electrochem. Soc.*, **164**, A6324 (2017).
30. I. Biswas, D. G. Sánchez, M. Schulze, J. Mitzel, B. Kimmel, A. S. Gago, P. Gazdzicki, and K. A. Friedrich, *Energies*, **13** (2020).
31. J. Mitzel et al., *Fuel Cells*, **20**, 403 (2020).
32. D. Gerteisen, N. Zamel, C. Sadeler, F. Geiger, V. Ludwig, and C. Hebling, *Int. J. Hydrogen Energy*, **37**, 7736 (2012).
33. D. Wittmaier, N. Wagner, K. A. Friedrich, H. M. A. Amin, and H. Baltruschat, *J. Power Sources*, **265**, 299 (2014).
34. J. Durst, A. Lamibrac, F. Charlot, J. Dillet, L. F. Castanheira, G. Maranzana, L. Dubau, F. Maillard, M. Chatenet, and O. Lottin, *Appl. Catalysis B*, **138–139**, 416 (2013).
35. J. F. Parker, C. N. Chervin, E. S. Nelson, D. R. Rolison, and J. W. Long, *Energy Environ. Sci.*, **7**, 1117 (2014).
36. J. F. Parker, E. S. Nelson, M. D. Wattendorf, C. N. Chervin, J. W. Long, and D. R. Rolison, *ACS Appl. Mater. Interfaces*, **6**, 19471 (2014).

Electrochimica Acta 396 (2021) 139261

Contents lists available at ScienceDirect

Electrochimica Acta

journal homepage: www.elsevier.com/locate/electacta

Evaluation of electrochemical impedance spectra of - batteries (Li-air/Zn-air) for aqueous electrolytes

Alexander Kube [a,*], Werner Strunz [b], Norbert Wagner [a], K. Andreas Friedrich [a,c]

[a] German Aerospace Center, TT-ECE, Pfaffenwaldring 38-40, Stuttgart 70569, Germany
[b] ZAHNER-Elektrik GmbH and Co.KG, Thüringer Straße 12, Kronach 96317, Germany
[c] Institute of Building Energetics, Thermal Engineering and Energy Storage (IGTE), University of Stuttgart, Pfaffenwaldring 31, Stuttgart 70569, Germany

ARTICLE INFO

Article history:
Received 19 May 2021
Revised 16 August 2021
Accepted 12 September 2021
Available online 16 September 2021

Keywords:
Electrochemical impedance spectroscopy
Zn-air battery
Distribution of relaxation times

ABSTRACT

Electrochemical impedance spectroscopy (EIS) is a powerful tool for investigating electrochemical systems such as fuel-cells and batteries. But because of the overlapping of processes due to similar time constants, it is necessary to understand the system well to set up a correct equivalent circuit for analysis of the measured spectra. Distribution of relaxation times (DRT) offers a model-free approach for impedance analysis. In this work DRT was used to analyze a Ni/Co_3O_4 gas diffusion electrode (GDE) for metal-air batteries. To identify the corresponding process for the identified peaks temperature, current density, gas composition, electrolyte concentration and electrode material composition were varied. In total five processes could be identified. Four were observed both during oxygen reduction reaction (ORR) and oxygen evolution reaction (OER). A fifth could only be recognized during OER. In particular the charge transfer coupled with an adsorption process and the porous structure could be identified. Furthermore, it could be shown that having a bimodal pore size distribution, consisting of two different materials, the correct calculation of the DRT spectra is inhibited, resulting in two peaks instead of the characteristic number of peaks that are getting smaller towards smaller time constants.

1. Introduction

Today's electrochemical energy storage is dominated by Li-ion batteries. Li-ion batteries do have many advantages like high energy density, low self-discharge and superior energy efficiencies. Even though this technology is mature, Zn-air batteries are an attractive alternative because they promise superior cost-efficiency and safety.

Zn-air batteries as primary batteries are well established as button cells for hearing aids, but the development of secondary Zn-air batteries still lacks behind due to low cycle life of the cells. This is due to the dimensional changes and passivation at the anode [1]. But also the instability of cathode materials in the wide potential range during operation is a problem, which causes oxidation and corrosion of cathode materials [2]. Furthermore, the formation of carbonates inside the alkaline electrolyte through uptake of CO_2 can lead to precipitates inside the pores of the cathode and clog them [3].

To protect cathode materials from the extremes of the wide potential window a three-electrode configuration could be used, with one cathode for charging and a second for discharging [1]. But more volume and mass is needed for this approach, reducing the energy density of the system. Therefore, bifunctional cathodes are preferable and could be improved by a multilayer design. In this several layers with different porosities, hydrophobicity and/or catalysts may be used [4].

An understanding of the relevant loss mechanisms during operation is crucial for commercialization of secondary Zn-air batteries. This will help to identify optimization potential for production of the electrodes as well as help in the mitigation of aging effects.

In this respect suitable *in-situ* characterization techniques are crucial to study the buried interfaces where the reaction takes place. EIS offers nonintrusive information on most relevant parameters without altering the system under investigation. In particular the influence of important parameters, like gas composition, current density and temperature can be studied. A drawback of the obtained EIS spectra is the need for equivalent circuit models (ECM) to analyze the spectra, because prior system knowledge about the physical processes inside the cell is needed. Due to the lack of knowledge about the number of involved processes, the presumptions strongly affect the obtained result. It is also noted that ECM analysis is not unambiguous as numerous ECs can de-

* Corresponding author.
E-mail address: alexander.kube@dlr.de (A. Kube).

https://doi.org/10.1016/j.electacta.2021.139261
0013-4686/

scribe an observed spectrum and the determination of parameters are interrelated.

Many works, in particular for studying alkaline fuel cells, have used ECM to characterize GDEs, like e.g. catalyst poisoning by CO [5], humidity and electrolyte saturation of porous electrode structures [6] and optimization of electrodes with EIS [7–9].

A general agreement about processes could be established, but separation of individual electrode processes and their corresponding polarization losses is not straight-forward with ECM, since the overlap, shape and size of arcs in the Nyquist plot can change with the variation of operation conditions.

Using physical principles generalized models can be derived. Although this approach is more challenging than the ECM, generalized models from physical principles give access to information about the actual physics and chemistry of the investigated system [10]. This approach was already applied to fuel cells [11,12] and Li-ion batteries [13,14] and showed its practicability. The computational speed and informative gain depend on the differential equations used for these simulations.

Another approach is the EIS spectra analysis by distribution of relaxation times (DRT) [15]. The use of DRT offers the possibility to analyze the characteristics of a system without presumptions. Since systems are modeled by a quasi-infinite series of R||C elements, elements can be identified without prior knowledge of the systems, if spectra consist mainly of R||C elements. DRT helps to identify processes and their dependency on operation conditions and thereby facilitates the understanding of the system and to construct physical models. Beside the amount of processes, one can extract the resistance and capacitance from the peaks and therefore obtain starting values for ECM fitting which is essential for good fitting procedures.

A drawback of DRT is, that the gained information depends on a proper choice of the regularization parameter λ. λ is used to suppress oscillations due to the ill-posed problem in Hadamardś nomenclature solving the DRT equations when using the solving approach of Tikhonov regularization [16]. While small values for λ lead to oscillations and therefore a large number of peaks, large values for λ lead to a merging of peaks and therefore to a loss of information. The optimal value depends on the signal-to-noise ratio, the number of measured data points and the algorithm used to solve the equations.

In this work DRT was applied to study impedance spectra of bifunctional GDEs for metal-air batteries, consisting of Ni/Co_3O_4 GDEs with PTFE as binder and as a hydrophobic agent. Operation conditions are varied in a defined manner to identify internal processes by their dependencies, based on their characteristic time constants and peak areas.

2. Materials and methods

2.1. Electrode preparation

Two types of gas diffusion electrodes were used in this work. A commercial silver electrode (Covestro AG) consisting of silver oxide and PTFE as hydrophobic agent and binder. This electrode was reduced electrochemically prior to tests. Furthermore, self-made electrodes were produced. One electrode with the mixture of 70 wt.-% Ni (StremChem, 3–7 µm), 20 wt.-% Co_3O_4 (SigmaAldrich, <50 nm) and 10 wt.-% PTFE (3M, Dyneon TF3057) was produced. This optimal mixture was developed in a work of Wittmeier et. al [17]. A second electrode consisting of 70 wt.-% Ag (Ferro AG, Typ 311) 20 wt.-% Co_3O_4 (SigmaAldrich, <50 nm) and 10 wt.-% PTFE (3M, Dyneon TF3057) was produced. For electrode preparation, all materials were mixed in a knife mill, then filled in a flexible form (inner diameter 3 × 7 cm) and pressed onto a stainless-steel mesh (0.125 mm, Haver&Boecker) in a hydraulic press with 300 kN/m² for 1 minute. Afterwards the flexible form was removed and the electrode pressed again with the same conditions followed by a thermal treatment in an oven for 1 h at 340 °C. For tests the electrode was cut by a scalpel into pieces of 2 × 2 cm.

2.2. Cell assembly

A homemade half-cell with 3-electrode configuration was used, as presented in former works [17]. The cell is made of PMMA with an active area of 1 cm² and placed inside a 1 L 32-wt% KOH (AlfaAesar) electrolyte bath. A reversible hydrogen electrode (Gaskatel RHE) is used as reference electrode and connected to the cathode by a Haber-Luggin capillary. As counter electrode a platinum foil was used. The prepared electrode was placed inside the half cell and a GDL (Sigracet 39BC) was mounted between the electrode and the current collector to allow for better gas distribution and electrical contact.

2.3. Measurement techniques

Electrochemical measurements were conducted using a Zahner electrochemical workstation (Zennium).

The electrolyte vessel was placed in a water bath to keep the temperature constant during operation.

The feed gas was either pure O_2, or a mixture of 70 vol.-% O_2 and either 30 vol.-% He or N_2. Additionally, a pump was used for flow of ambient air behind the electrode. The pressure of all gas flows was controlled by bubbling through a 3 cm high water column with 1 bubble per second.

Prior to all tests with the self-made electrode 20 cyclic voltammetry cycles between 0.3 V vs. RHE and 1.8 V vs. RHE were performed to activate the electrode and a polarization at 300 mV vs. RHE for 1 h for ORR tests or 1.8 V vs. RHE for OER tests was conducted to ensure a completed oxidation or reduction processes.

For each temperature increasing current density steps (5 $mAcm^{-2}$, 10 $mAcm^{-2}$, 20 $mAcm^{-2}$, 30 $mAcm^{-2}$, 40 $mAcm^{-2}$, 50 $mAcm^{-2}$ for ORR) were recorded for 1 h, followed by an EIS measurement in a frequency range of 10 mHz to 1 MHz with an amplitude of 5 mA. After completing the current variation, the feed gas was changed. For each temperature (25 °C, 35 °C, 45 °C, 55 °C, 65°C) the current variation was performed as well as the gas variation in the order O_2, He/O_2, N_2/O_2, ambient air. Variation of electrolyte concentration was performed at 25 °C with pure O_2.

2.4. Analysis techniques

The distribution of relaxation times $G(\tau)$ is linked with the complex impedance $Z(\omega)$ by the expression

$$Z(\omega) = R_0 + R_{pol} \int_0^\infty \frac{G(\tau)}{1 + j\omega\tau} d\tau \quad ((1)$$

With

$$\int_0^\infty G(\tau) d\tau = 1$$

Where R_{pol} describes the dc polarization and R_0 the ohmic resistance [16].

To calculate a DRT from EIS data an inverse problem has to be solved, which is ill-posed [18]. This Hadamard ill-posed problem of Eq. (1) has the requirement that $\gamma(\tau)$ is always positive. It can be solved by the use of different techniques, with different parameters to obtain the solution. By using a Fourier transformation, a frequency window function is needed, which requires several parameters to be set to obtain a solution [19,20]. Multi-(RQ) CNLS fit models the data with an increasing number of R-CPE elements, until a satisfactory match between the fit and the measurement is obtained [21]. Maximum entropy needs an adjustment of

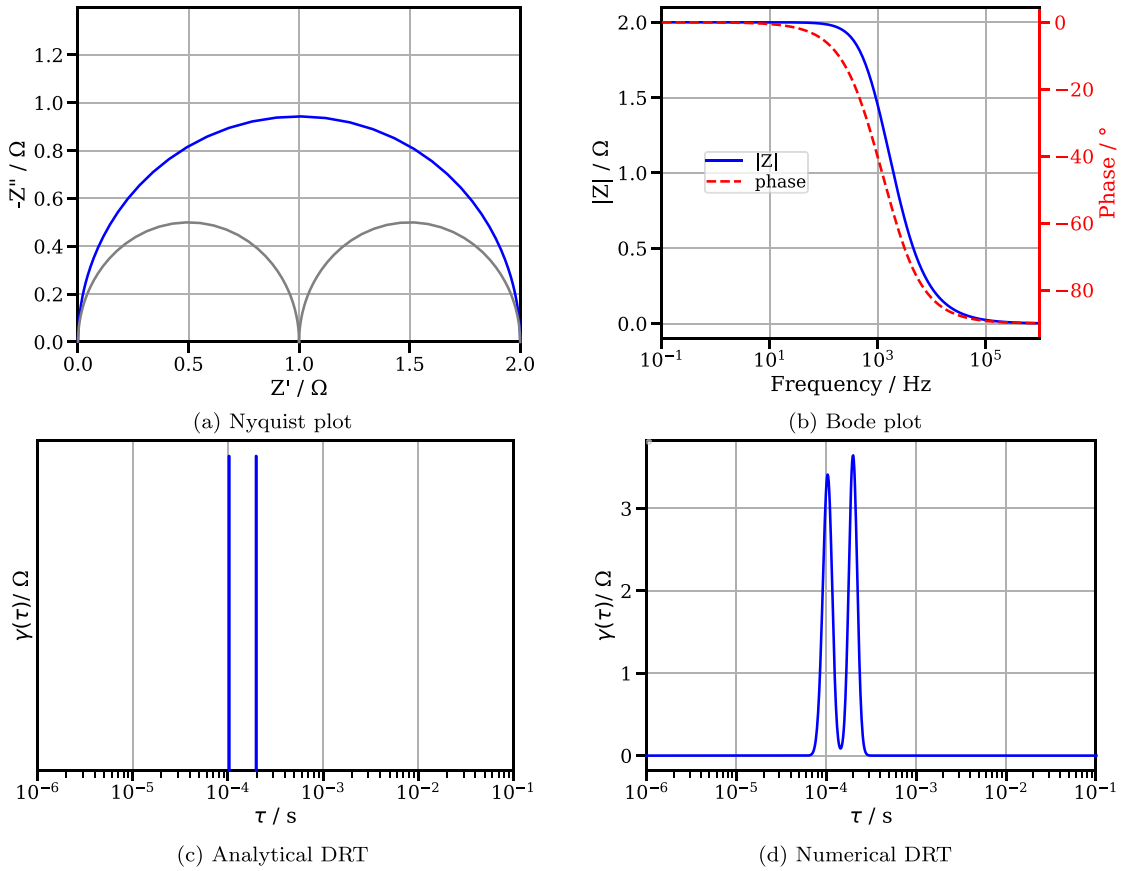

(a) Nyquist plot (b) Bode plot (c) Analytical DRT (d) Numerical DRT

Fig. 1. A theoretical calculated impedance spectrum consisting of two RC-elements, (a) shows the Nyquist plot, (b) the Bode plot, (c) the analytical and (d) the numerical calculated DRT spectra.

a smoothing operator [22,23], as well as Tikhonov regularization, which is used in this work and uses the regularization parameter λ to suppresses oscillations [24–26]:

$$\underbrace{\min}_{\bar{\gamma}} = \left\{ \|\boldsymbol{H}\overline{\boldsymbol{\gamma}} - \boldsymbol{z}\|^2 + \lambda \|\overline{\boldsymbol{\gamma}}\|^2 \right\}$$

In this **H** is a N x M matrix composed of coefficients of equations and $\bar{\gamma}$ the vector with the unknown values. The vector **z** consists of the measured impedance values [18].

Fig. 1 shows exemplarily the Nyquist plot (1a) and the corresponding Bode plot (1b) of two RC elements with $\tau_2 = 2\tau_1$ and $R_2 = R_1$ where neither in the Nyquist nor in the Bode plot these two processes can be distinguished. An analytical calculated DRT spectrum with Eq. (2) is shown in Fig 1c which shows how a perfectly calculated DRT spectrum would look like [27].

$$G(x) = \frac{R_{pol}}{2\pi} \frac{sin((1-n_Q)\pi)}{cosh(n_Q(x+ln\tau_{RQ}) - cos(1-n_Q)\pi)}, \; with\, x = ln(1/\tau) \tag{2}$$

Eq. (3) describes the analytical DRT spectrum of an RQ-element and converts for $n_Q = 1$ to a RC-spectrum. τ_{RQ} describes the time constant of the RC element. Fig. 1d shows the calculated numerical DRT using the theoretical impedance data of Fig. 1a, b and the Tikhonov regularization described above. One can imagine a DRT spectrum as a fit with weighting factors of an infinite amount of serial connected RC elements to the measured impedance data. A numerical calculated DRT spectrum shows a characteristic broadening in the time domain whereas the analytical DRT spectrum consist of Dirac delta functions.

For the commonly used Tikhonov regularization, for instance, a weighting factor (regularization parameter λ) has to be preselected by the user. The quality of the result of this method depends on the choice of this weighting factor and the choice of it has to be done carefully as it can also determine the number and shape of identifiable peaks. Fig. 2 shows the calculated numerical DRT spectra for one RC element (Fig. 2a) and of two RC elements (Fig. 2b) with the same parameter set as used for calculations in Fig 1a, b.

For one RC element the peak becomes smaller and wider for an increase of λ while for the two RC elements this behavior is the same for both peaks until they merge and only on wide peak is observable.

A more detailed description on the mathematics and theory is given by Boukamp [20,21,24], Evers-Tiffee [16,28,29] and Ciucci [15,26,30].

In this work all EIS spectra were tested for a regularization parameter which shows all peaks without oscillation, which occurs for values too small, or merging of peaks, which occurs for λ values to high. A variation to determine an optimal value was performed for all tests with the Relaxis software and is shown exemplarily for the current variation with O_2 as feed gas in Fig. 3.

A cross check with fitting an ECM with the obtained values for resistance, capacitance and amount of processes was done to ensure a proper choice. Since this parameter also changes the peak shape, it was kept constant for all spectra.

3. Results and discussion

The impedance spectra measured for different current densities are shown in Fig. 4 (a), as well as the corresponding DRT spectra calculated from these. Fig. 4 (a) shows typical impedance spectra

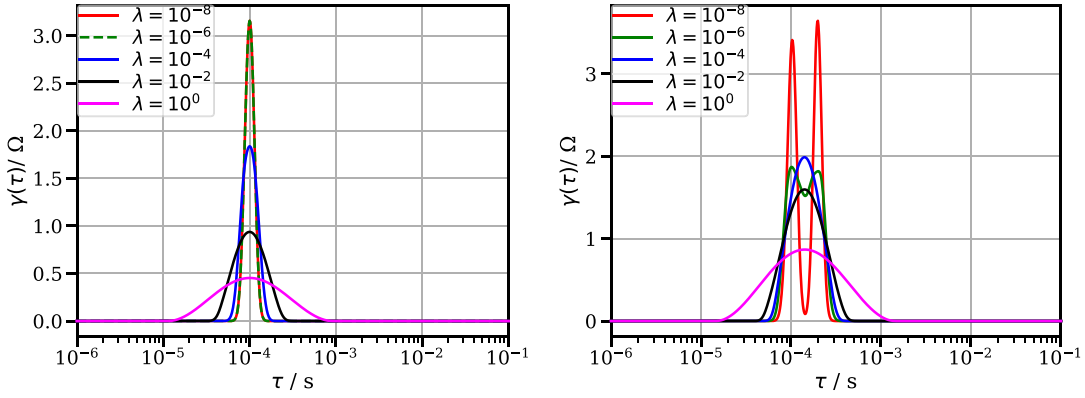

(a) 1 RC (b) 2 RC

Fig. 2. DRT spectra from synthetic impedance spectra for (a) one RC element and (b) two RC elements.

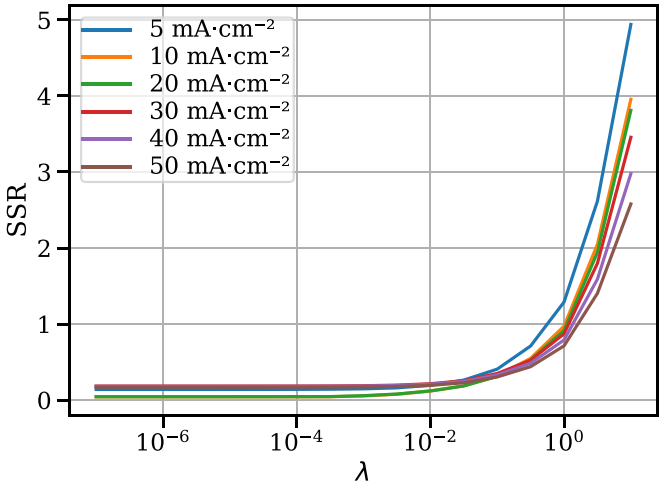

Fig. 3. Sum of squared residuals (SSR) over λ.

for this kind of electrodes, where two semicircles can be observed. Both semicircles seem to be depressed, giving already the idea that each semicircle is built by more than one process. For varying current densities, the Nyquist plots in Fig. 4 (a) show changes only in the low frequency domain, but it is unclear how many processes are influenced by this. DRTs reveal 4 processes, were processes P3 and P4 show a decrease in peak height with increase of current density and can therefore be linked to the lower frequency semicircle. While Process P4 shifts to lower τ with increase of current density, no such behavior is observed for P3. The area under each peak corresponds to the ohmic resistance of the RC-element. The capacity is linked by $\tau = RC$.

Charge transfer resistance can be calculated from the Butler-Volmer-Equation for ORR to [31,32]:

$$R_{ct} = \frac{\eta_D^{\sim}}{i_D^{\sim}} = \frac{RT}{zF} \frac{1}{\left(\alpha i_D^{=} + j_0 exp\left(-(1-\alpha)\eta^{=}\frac{zF}{RT}\right)\right)} \tag{3}$$

Where $\eta_D^{\sim}$ represents the alternating overpotential and $i_D^{\sim}$ the alternating current. While $i_D^{=}$ represents the direct current and $\eta^{=}$ the corresponding overpotential. T describes the temperature, R the gas constant, F the faraday constant, z the number of electrons involved in the electrode reaction, α the charge transfer coefficient and j_0 the exchange current density.

With this equation it can be assumed that P3 or P4 correspond to a charge transfer reaction. Since the reaction is coupled by adsorption of educts and products to the active surface it can be further assumed that one of these processes describes the adsorption coupled to the charge transfer and can be expressed with the following equations for area resistance and capacitance [33]:

$$R_{ad} = \frac{RT}{n^2F^2c_sAk_r},\ C_{ad} = \frac{n^2F^2c_sA}{RT} \tag{4}$$

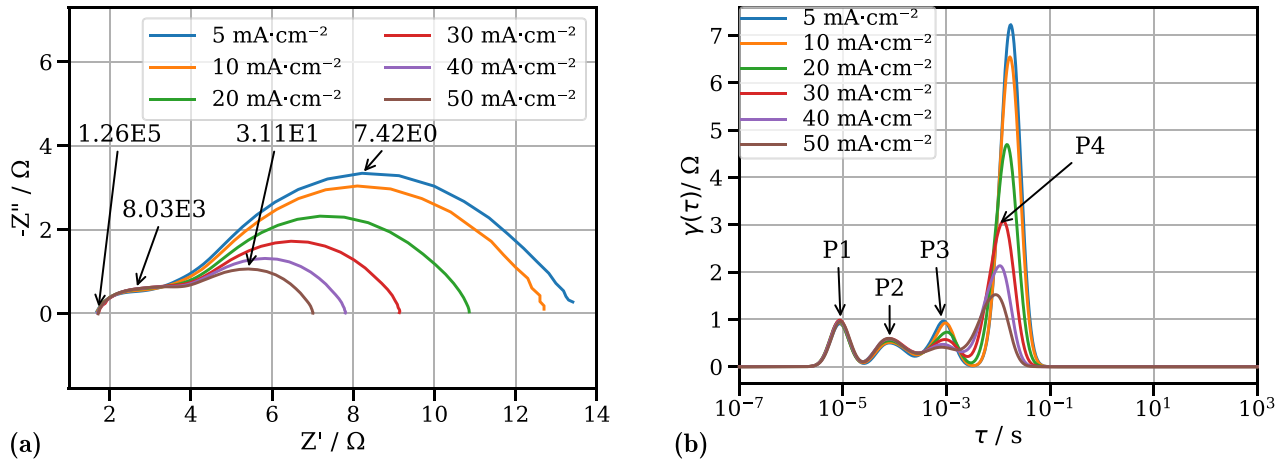

Fig. 4. Current density variation of a Ni/Co_3O_4 electrode at 25 °C in 32 wt.-% KOH, (a) shows the measured Nyquist diagram with some frequency markers, (b) the calculated DRT spectra.

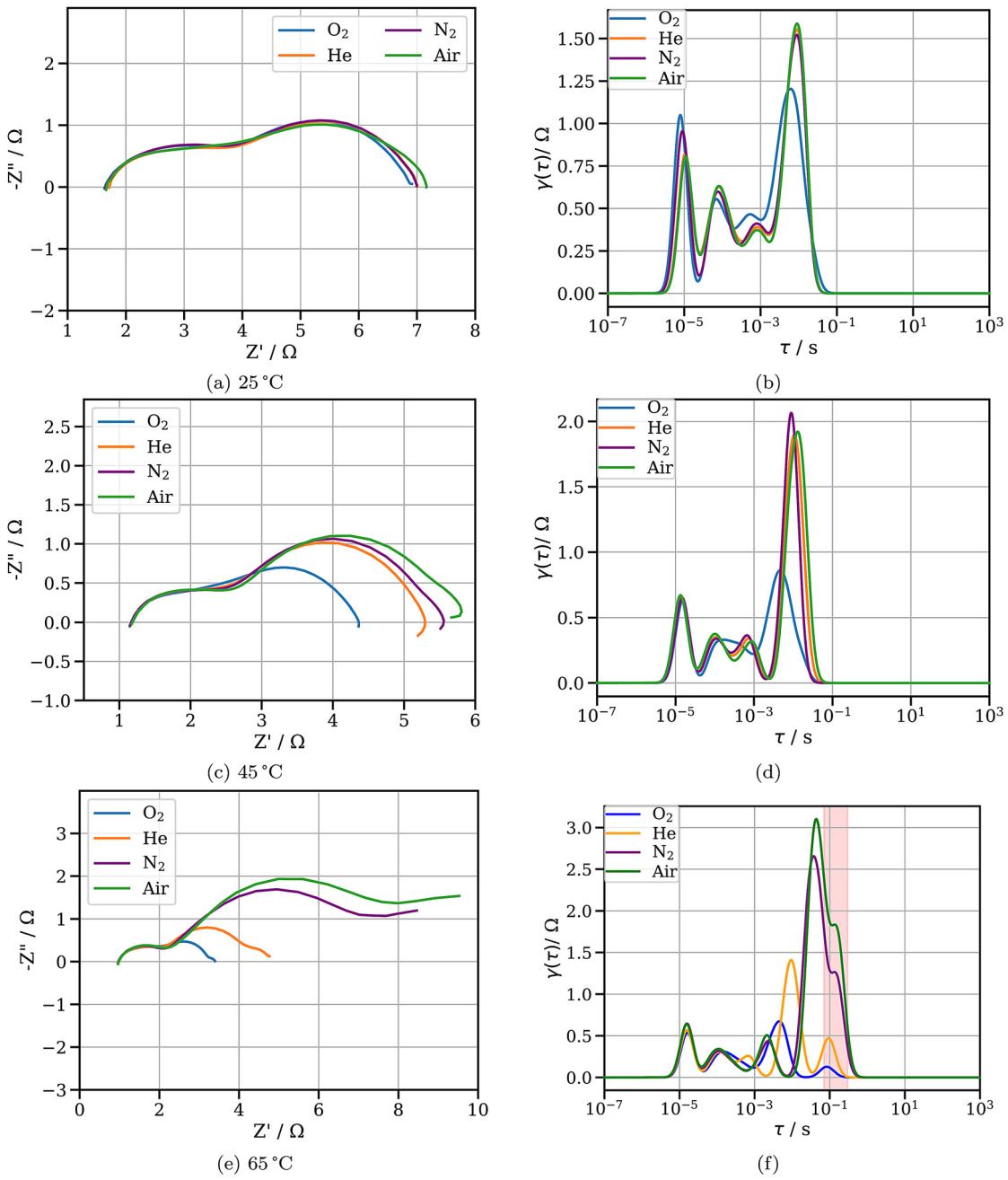

Fig. 5. Gas variation of a Ni/Co_3O_4 electrode at –50 mA/cm^{-2} in 32 wt.-% KOH and varying feed gas for 25 °C (a, b), 45 °C (c, d), 65°C (e, f). (a), (c) and (e) show the measured Nyquist plot, (b), (d) and (f) show the calculated DRT spectra. N_2 and He both are mixed with 30 vol.-% O_2, air describes the ambient air supplied by a pump.

Where k_r represents the first order rate constant, A the electrode surface and c_S the surface concentration. With increase of current density, the driving force for the reaction increases, resulting in a higher rate constant. The capacity on the other hand is only slightly influenced because only the surface coverage might change with higher reaction rates. Due to the fact that P3 shows only slight changes in τ and a considerably decrease of the resistance, the adsorption process can be linked to P3. The charge transfer is therefore described by P4.

Process 1 and 2 show no current dependency and therefore no potential dependency and could be associated to the electronic properties of the hydroxide layers of the metals [34], or the ionic and electric transport in the porous system.

A gas variation is shown in Fig. 5 for three different temperatures (25 °C, 45 °C and 65 °C) for ORR. As can be seen for 25 °C in Fig. 5 (a) and the corresponding DRT spectra in Fig. 5 (b), the charge transfer increases with reduction of oxygen partial pressure. With increase of temperature the difference between the charge transfer of pure oxygen and gas mixtures is getting bigger and a splitting up between the different gas mixtures can be observed.

The diffusion constants of oxygen in the different gas mixtures varies in a wide range. Bultel [35] gives a diffusion coefficient of oxygen in helium ($D = 1.3{*}10^{-4}$ m^2 s^{-1}) and states that the diffusion coefficient in N_2 is one decade lower and observed a comparable behavior of his polymer electrolyte fuel cell cathodes for different gas compositions. Due to the lower effective diffusion rate of O_2 in N_2 the O_2 concentration is smaller near the active center compared to the He/O_2 mixture. The higher effective diffusion of O_2 from the gas compartment to the active centers for the He/O_2 mixture compared to the N_2/O_2 mixture leads to different charge

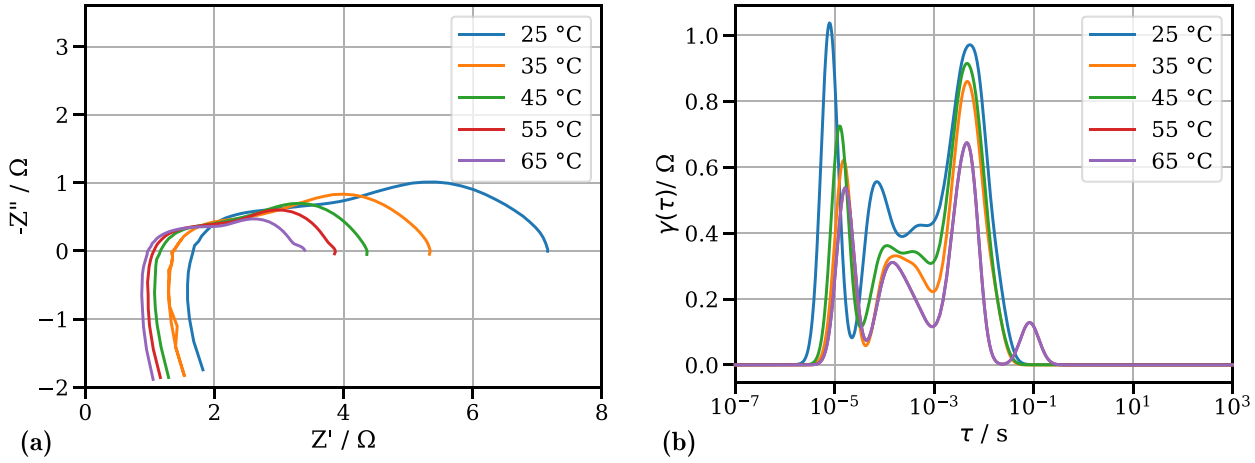

Fig. 6. Temperature variation of a Ni/Co_3O_4 electrode at –50 mA/cm^{-2} in 32 wt.-% KOH and O_2 as feed gas. (a) shows the measured Nyquist diagram, (b) the calculated DRT spectra.

Table 1
calculated oxygen partial pressures for the tested gas compositions at 20 °C in kPa

O_2	O_2 / He	O_2 / N_2	Ambient air
108.7468	35.8862	35.8868	21.5386

transfer resistances. A diffusion limitation of the reaction would be resembled by an additional diffusion contribution in the low frequency domain which was not observed for 25 °C or 45 °C, only the spectra recorded at 65 °C show such a diffusion contribution. Consequently, the observed differences between the different gas compositions are not due to a diffusion limitation which is plausible due to the low current densities as it is explained in more detail in literature [36,37].

The used gas mixtures also influence the partial pressure of oxygen in the system. The lower partial pressure reduces the O_2 concentration in the electrolyte leading to a lower surface coverage which reduces the exchange current density and therefore the Butler-Volmer curve [38]. However, it is to mention, that the differences in impedance of the He and the N_2 mixture cannot be explained by this, as they are almost the same (Table 1).

The higher tendency of nitrogen to adsorb on the electrode surface than that of helium could be the reason to the higher observed impedance for the N_2/O_2, compared to the He/O_2 mixture. This adsorption influences the exchange current density j_0 and therefore the Butler-Volmer curve by reducing the number of active sites. This leads to the assumption that the observed increase in impedance is due to a combination of both the partial pressure and the nitrogen adsorption.

The spectra for 45 °C show an inductive loop in the low frequency domain, which could be due to adsorbed species, or formation of intermediates. But inductive contributions cannot be resolved by DRT properly and therefore no additional process can be identified in the DRT spectra. Only if negative DRT values are permitted, an analysis of such processes can be performed [39]. As these inductive contributions cannot be resolved by DRT the calculated spectra might be distorted somewhat. As shown in other publications [16], derivations of measurement points influence the gained DRT spectra. For 65 °C an additional impedance contribution can be seen for all gases, but is the smallest for pure oxygen and highest for ambient air. This arc is reflected in the DRT with an additional process (red area in DRT spectrum) and can be attributed to oxygen diffusion [29]. Due to the elevated temperature inside the electrolyte container, water starts to evaporate. As described by Wagner the amount of water vapor inside the gas influences the charge transfer resistance [33]. This water vapor changes the gas composition inside the porous system leading to a decrease of oxygen partial pressure and therefore to a higher charge transfer resistance as described above. The time constant of P4 for the tested gas compositions between 25 °C and 45 °C does not show a drift, meaning that the active area does not change. Only for 65 °C a small shift to higher time constants can be noticed indicating a small change of active area. Pasaogullari et al. found that by an increase of liquid saturation level of the porous system the electrochemical performance is determined by the transport of oxygen [40]. The reduced number of active centers contributes less to the lower electrochemical performance for increased saturation levels of the porous system. This assumption is also aided by the additional diffusion related peak. This mass transport limitation can occur either in plane or through plane, but no distinction between these two could be obtained by these tests in the used measurement setup. Further experiments with locally resolved impedance spectra would be necessary.

To identify the role of the temperature itself, Fig. 6 shows the temperature variation for pure oxygen. The Nyquist spectra (Fig. 6 (a)) shows a decrease in the overall impedance, which is also reflected in the DRT spectra (Fig. 6 (b)). DRT shows clearly that all 4 processes are affected by temperature. While adsorption and charge transfer resistance do not show changes in the time regime, P1 and P2 show a clear shift to higher τ.

The temperature dependency of the charge transfer resistance is linked with the exchange current density j_0 as described by Eq. (3). For increasing temperatures j_0 increases as well, which decreases R_{CT}, as can be observed for P4 in Fig. (6). This increase of exchange current density is accompanied by an increase of the open circuit potential [41]. On the other hand, it is known, that an increase of temperature decreases the onset potential, while the transfer coefficient does not change. Together with the higher reaction rate, which is inversely proportional to the charge transfer resistance, the charge transfer resistance decreases [42]. The reduction of peak size of P3 can be explained by a decrease of surface coverage of adsorbed hydrogen on the active sites [42]. The increased reaction speed leads to the observed decrease of the adsorption related resistance of P3. Contributions from diffusion could only be seen for 65 °C as additional peak at around $\tau = 10^{-1}$ s. This peak could arise from the above described mechanism of water vapor inside the porous system. The increase of the effective diffusion rate with elevated temperatures is not observable, probably due to the use of pure oxygen where no mass transport limitations are to be expected.

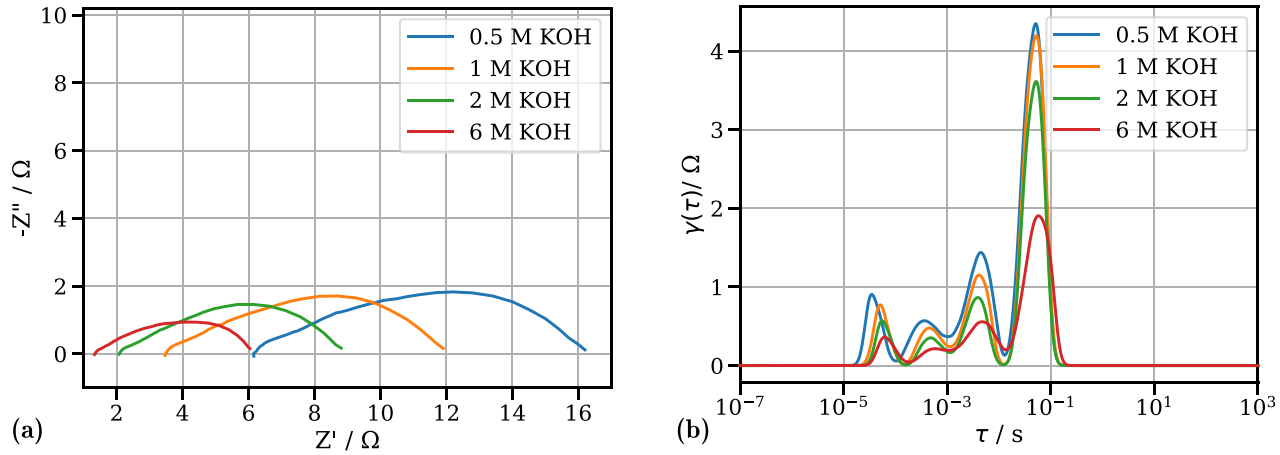

Fig. 7. KOH variation with a Ni/Co_3O_4 electrode at 25 °C, -50 mA/cm^{-2} and O_2 as feed gas. (a) shows the measured Nyquist diagram, (b) the calculated DRT spectra.

Fig. 7 shows the variation of electrolyte molarity from 0.5 M to 6 M KOH, which shows the same trend as temperature variation. All 4 processes are affected by electrolyte concentration. Reason for this can be of different nature. Oxygen solubility and diffusion constant decreases with increase of KOH molarity, while on the other hand the exchange current density increases with increase of KOH molarity [43]. This dependency of the exchange current density j_0 is due to the dependence on the concentration of reaction products and therefore on the KOH molarity.

In the tested range up to 6 M KOH an increase of KOH concentration increases the ionic conductivity of the electrolyte. As can be seen in Fig. 7, higher KOH concentrations lead to smaller peaks for P1 and P2 and a shift to higher time constants and could therefore be related to electric and ionic transport inside pores.

One of the features of transport inside a porous structure is a 45° rise in the high frequency domain in the Nyquist plot. This electric and ionic transport and can be described by a transmission line model [44]. To our knowledge no theoretical DRT calculation of transmission line models for transport in porous media was performed, but since the characteristic features of other transmission line models are similar we compare a calculated Gerischer impedance with the calculated porous electrode model. The impedance of a porous electrode (Z_{PE}) was calculated using the porous electrode model described by Eq. (5) [45]. In this equation σ stands for electric and κ for the ionic conductivity, L describes the length and a_s the reactive surface.

$$Z_{PE} = P_1\left(1 + \frac{2 + P_2\cosh(\nu)}{\nu\sinh(\nu)}\right) \tag{5}$$

With

$$\nu = \frac{L\,P_3}{\sqrt{\frac{R}{1+j\omega\,R\,C}}} \tag{6}$$

$$P_1 = \frac{L}{\sigma + \kappa} \tag{7}$$

$$P_2 = \frac{\sigma}{\kappa} + \frac{\kappa}{\sigma} \tag{8}$$

$$P_3 = \sqrt{\frac{a_s}{\sigma} + \frac{\sigma}{a_s}} \tag{9}$$

The Gerischer impedance was calculated using Eq. (10) [46].

$$Z_{Gerischer} = \frac{\tilde{R}}{\sqrt{1 + j\omega\,R\,C}} \tag{10}$$

$$\tilde{R} = \frac{P_1(P_2+2)}{P_3}\sqrt{R} \tag{11}$$

The result of both calculations is shown in Fig. 8 as Nyquist spectra. It can be seen, that both models result in the same spectra and therefore the DRT of both models should be comparable.

A theoretical DRT calculation was done by Boukamp and Rolle[21] and is shown in Fig. 8 (b), calculated with Eq. (12) and the parameters $\tau_0 = 1$, $\gamma = 0.5$, $R_0 = 1$, $\beta = 0.9$.

$$R_0\,G_{HN}(\tau) = \frac{R_0}{\pi}\left(\frac{\tau}{\tau_0}\right)^{\beta\,\gamma}\frac{\sin(\gamma\,\theta)}{\left(1 + 2\cos(\pi\beta)\left(\frac{\tau}{\tau_0}\right)^{\beta} + \left(\frac{\tau}{\tau_0}\right)^{2\beta}\right)^{\gamma/2}} \tag{12}$$

with

$$\theta = \frac{\pi}{2} - atan\left(\frac{\left(\frac{\tau}{\tau_0}\right)^{\beta} + \cos(\pi\beta)}{\sin(\pi\beta)}\right) \tag{13}$$

This DRT shows the characteristic features of a steep signal rise, coming from the higher values for τ and a slow attenuation towards smaller τ values. By using impedance data and not the theoretical formulas DRT spectra of transmission line models do not show the continuous decrease of signal height towards higher values of τ. Instead they are characterized by a series of peaks that are becoming smaller towards higher values of τ as it is reported in literature [47,48].

In contrast to this, none of the spectra in Figs. 4–7 show such a behavior. Instead only two single peaks are observable and do show the same tendencies. But by having a look at the Nyquist spectra in these pictures the 45° slope can be identified. Fig. 9 shows spectra with and without Co_3O_4 in a nickel- (Fig. 9 a, b) and silver-based electrodes (Fig. 9 c, d). Interestingly both electrodes without Co_3O_4 do clearly show the features described above for transmission line models and therefore P2 can be linked to the electric and ionic transport. By adding the Co_3O_4 P1 appears and the transport characteristics are not visible anymore. This is more pronounced for the nickel-based electrode.

The reason for this might be due to the high amount of Co_3O_4 inside the electrode, resulting in a bimodal pore size distribution. Fig. 10 shows the EDX mapping of an electrode cross section image, where the Co_3O_4 agglomerates are visible. Fig. 10 c) exhibits the result of mercury porosimetry of a nickel-based electrode with and without Co_3O_4, where the bimodal pore size distribution with added Co_3O_4 is clearly visible. This bimodal pore size distribution

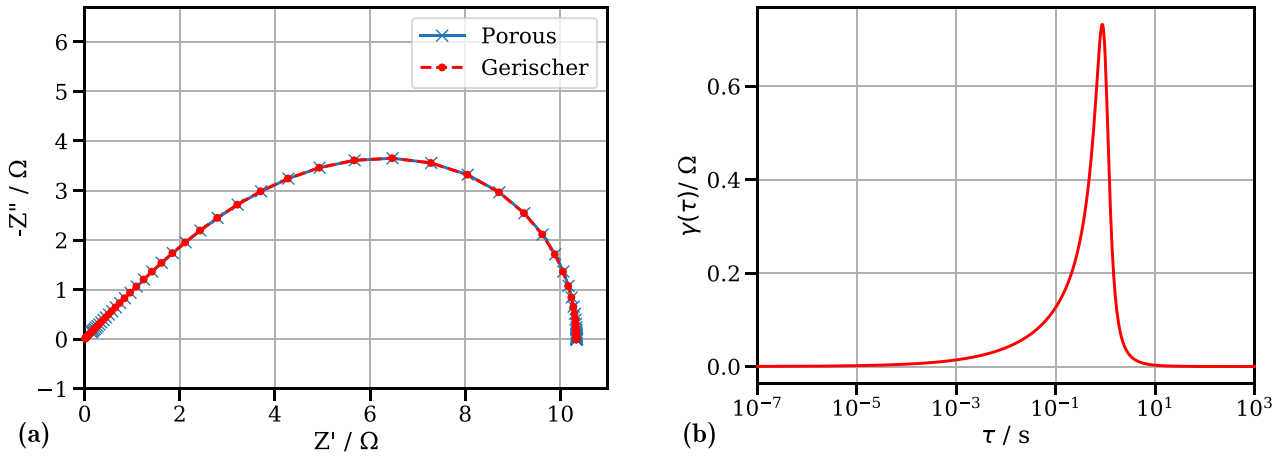

Fig. 8. (a) shows the comparison of theoretical calculated Nyquist spectra for a Gerischer element and ionic and electric transport in a porous structure. (B) shows a analytical DRT spectrum for a Gerischer element.

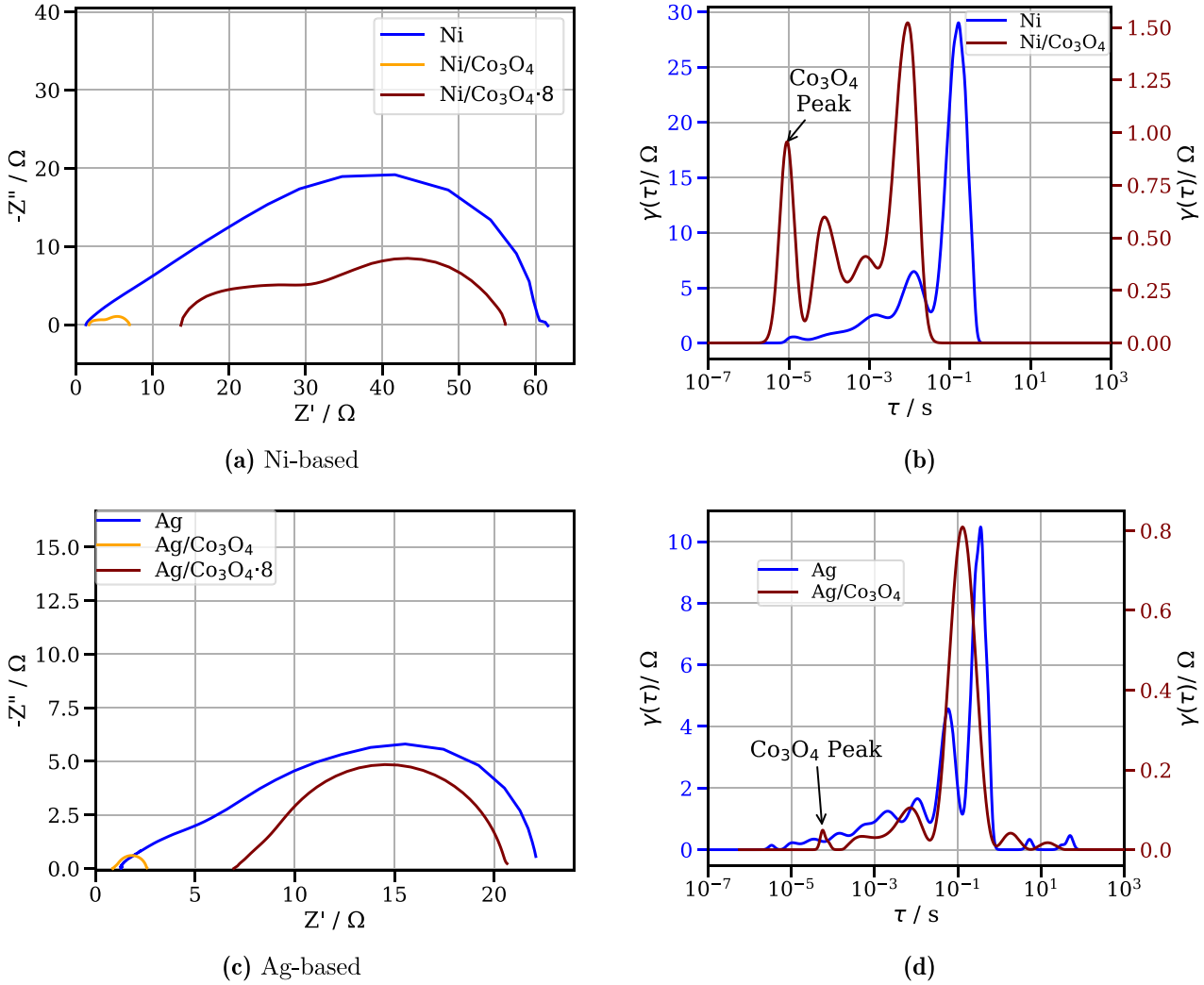

Fig. 9. Comparison of electrodes with and without Co_3O_4 added. Nyquist spectra show values for electrodes with Co_3O_4, as measured and multiplied by a factor of 8 for better comparability of spectra. Both numerical DRT spectra show a number of peaks that are getting smaller towards smaller values of τ for electrodes without Co_3O_4 added, but do not show this characteristic for electrodes with Co_3O_4 added.

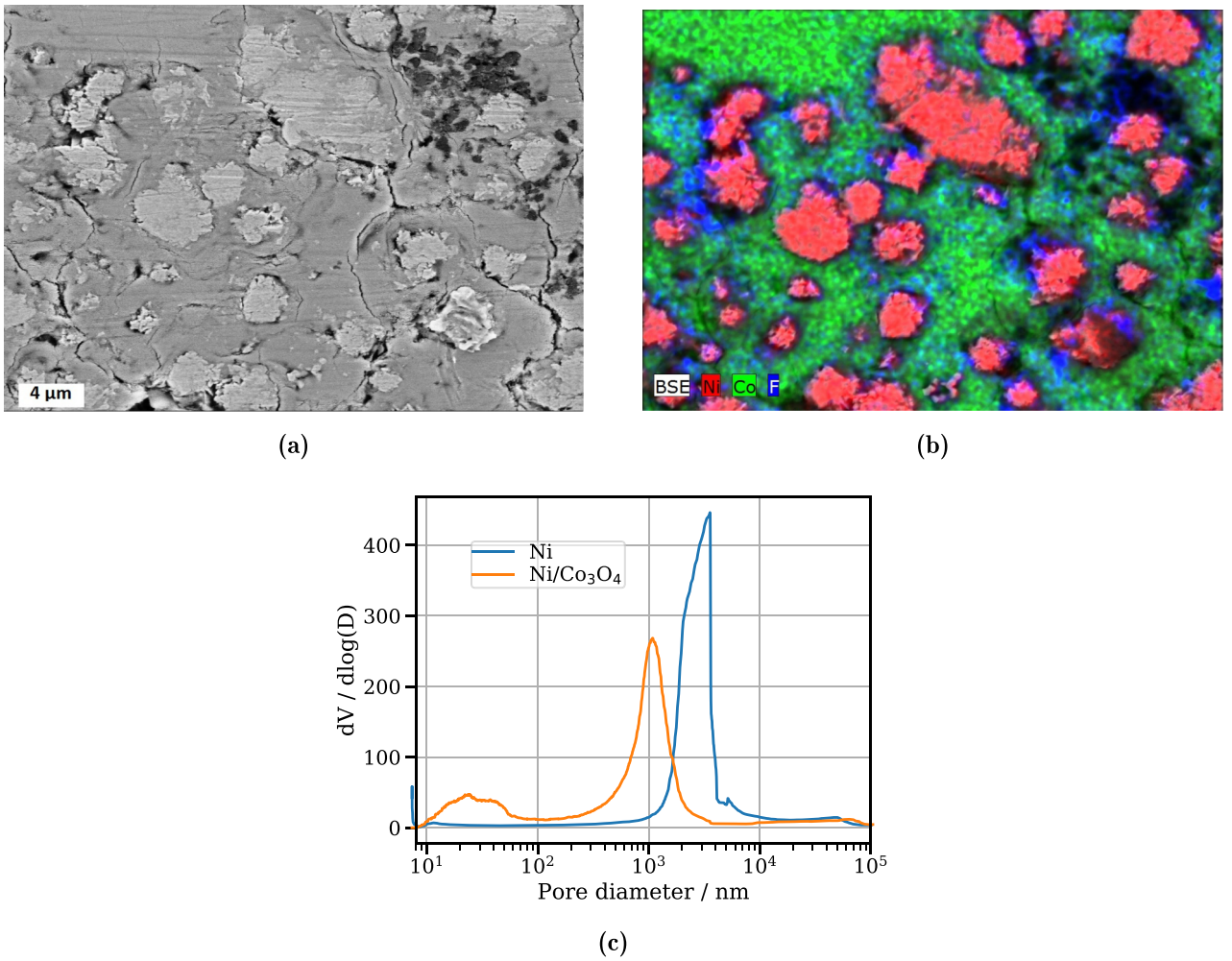

Fig. 10. SEM image of a Ni/Co_3O_4 electrode is shown in (a), the corresponding EDX mapping in (b). Red shows Ni particles, green Co and blue F. In (c) the pore size distributions of a Ni/Co_3O_4 electrode (orange) and a Ni electrode (blue) are shown.

might inflict some conflicts in the mathematical deconvolution of EIS spectra.

In the case of the electrodes used in this work, this bimodal pore size distribution is realized by two materials with great differences in electric conductivity and reactive surface. Additionally, the smaller pores change the effective diffusion constant, which might result in changed ionic conductivity. All three are important parameters to describe the ionic and electric transport in Eq. (5). To estimate the influence of the Co_3O_4 agglomerates and mimic the bimodal pore size distribution two descriptions to describe the transport in pores were set as parallel ($\frac{Z_{PE\_1} * Z_{PE\_2}}{Z_{PE\_1} + Z_{PE\_2}}$). For Z_{PE_1} the electric conductivity of Ni was used as well es the BET values obtained for the powder (0.1018 m²/g). For Z_{PE_2} the electric conductivity of Co_3O_4 was used as well es the BET values obtained for the powder (43.9570 m²/g). The calculated Nyquist spectrum shown in Fig. 11 (a) in blue. As comparison a single Z_{PE} is shown in this figure in orange. Fig. 11 (b) shows DRT spectra calculated from this theoretical impedance data. The single equation shows the peaks as described above, characterizing the electric and ionic transport in a porous system. By adding the second Z_{PE} in parallel to this the descending order of peaks is not visible anymore, but instead two main peaks and two side peaks are visible. This result is comparable to the observed two peaks in our measured data and the absence of the characteristic peak behavior might be explained by the bimodal pore size distribution of the two different materials. The smaller peaks might not be visible in our data, since there are more elements than just the transport present, or they are too small to be seen. Furthermore, the theoretical description might not be perfect since only the electrical conductivity and reactive surface were varied, as well as bigger pores are also accompanied by Co_3O_4 and not just Ni particles.

Anodic operation / OER:

During the charging of the battery, positive currents are applied leading to gas evolution. Fig. 12 shows the Nyquist and DRT spectra for a current variation, which show the same trend as for the discharge, with an additional process in the low frequency domain.

Due to the pre oxidation step before recording the EIS this additional proces cannot be due to the formation of NiOOH. This additional process could be a potential dependent reaction intermediate [49], which might originate from the rate-determining step described by Eq. (16) [50].

$$OH^- \rightleftharpoons OH_{ad} + e^- \tag{14}$$

$$OH_{ad} + OH^- \rightleftharpoons O^-_{ad} + H_2O \tag{15}$$

$$CoO_2 + O^-_{ad} \rightarrow CoO_2 \cdot O + e^- \tag{16}$$

$$CoO_2 \cdot O \rightarrow CoO_2 + O_{ad} \tag{17}$$

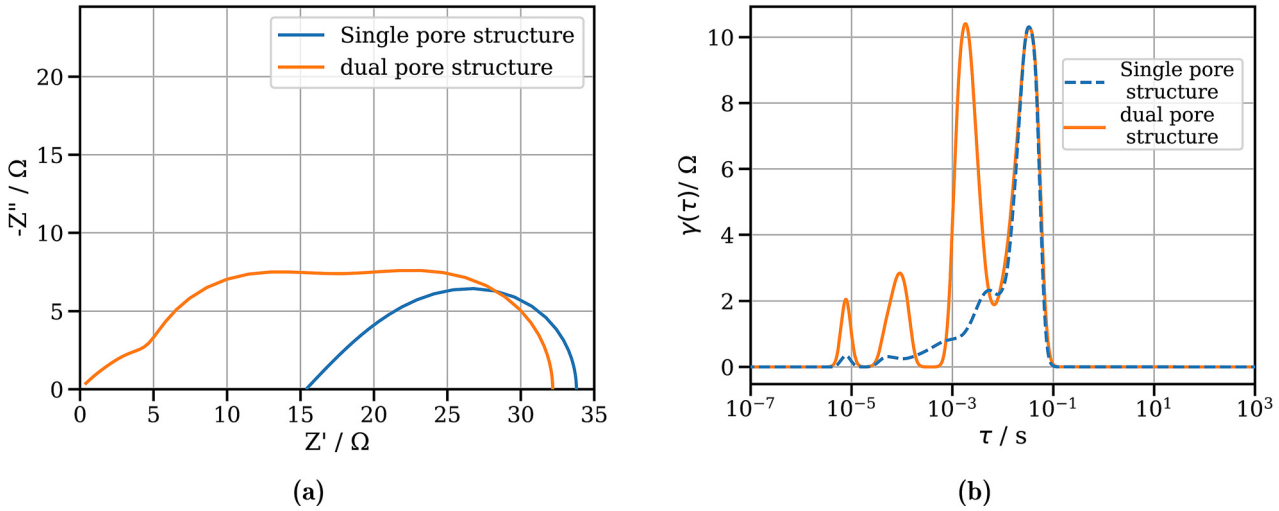

Fig. 11. Orange shows DRT of two materials with different properties. One with a high electrical conductivity and low surface area and one with low electrical conductivity and high surface area. In blue the spectrum for only one single material is shown.

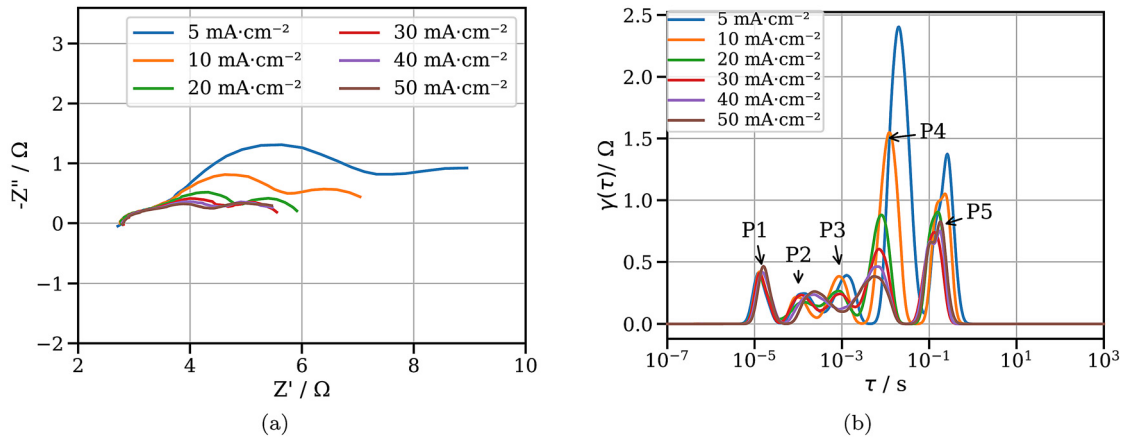

Abbildung 1: Stromvariation für den anodischen Betrieb bei 7,5 M, 25 °C und reinem O_2 a) Nyquist Auftragung , b) die daraus berechneten DRT-Spektren

Fig. 12. OER Current density variation of a Ni/Co_3O_4 electrode at 25 °C in 6 M KOH and O_2 as feed gas. (a) shows the measured Nyquist diagram, (b) the calculated DRT spectra.

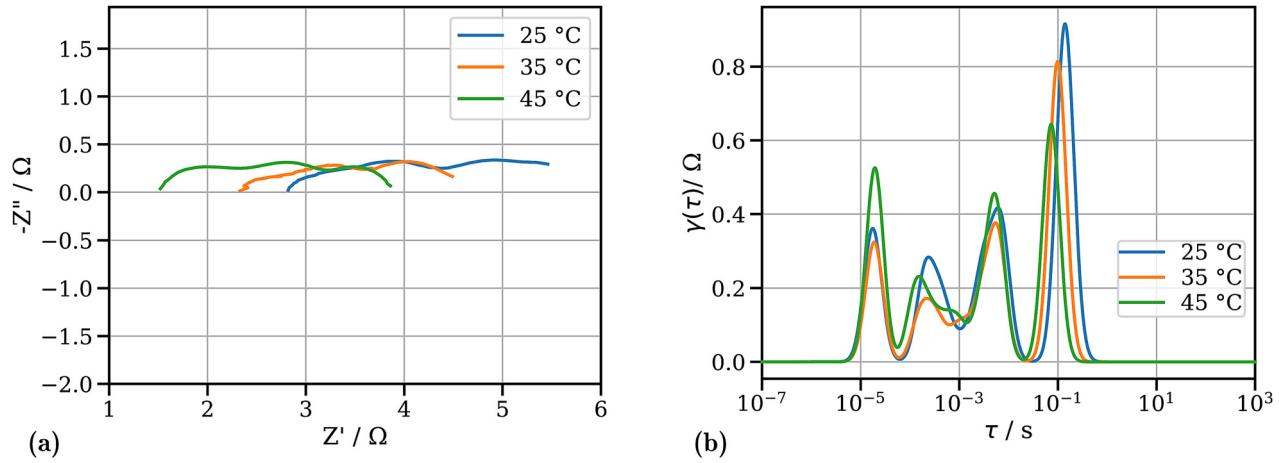

Fig. 13. OER temperature variation of a Ni/Co_3O_4 electrode at 50 mA/cm^{-2} in 6 M KOH and O_2 as feed gas. (a) shows the measured Nyquist diagram, (b) the calculated DRT spectra.

$$2O_{ad} \rightarrow O_2 \quad (18)$$

Another possible explaination could be a diffusion of charge species (H^+/OH^-) into the oxide film through defects and pores [51] and therefore a diffusion limitation.

In Fig. 13 the temperature dependence is investigated. P4 which has been associated to the charge transfer shows no clear shift in τ for increasing temperature, similar as it was observed in Fig. 6 for oxygen reduction. In contrast, the additional process P5 shows a clear shift to smaller values of τ for temperature increase. This indicates that this additional process is not due to a charge transfer. The exact origin of this peak, however, is not clear and identifying the underlaying process needs more investigations.

4. Summary

The deconvolution of EIS by DRT unveiled 4 processes for the Ni/Co_3O_4 electrode during oxygen reduction. P3 could be assigned to an adsorption while P4 is correlated to charge transfer the charge transfer. The dependencies of P1 and P2 correlate to the expected behavior of electronic and ionic transport as they depend strongly on the temperature and electrolyte concentration, but not on the current density. This leads to the conclusion, that both are due to the porous structure. But all electrodes do only show two peaks instead of the characteristic number of peaks that are getting smaller towards smaller values of τ. It was shown that such characteristic behavior can be expected from transmission line models describing ionic and electric transport in a porous system. By comparing electrodes consisting only of Ni/PTFE and Ag/PTFE with electrodes with 20 wt.-% Co_3O_4 added, electrodes without Co_3O_4 showed this expected behavior. Adding Co_3O_4 induces a bimodal pore size distribution where only two peaks can be observed Theoretical calculations showed that this behavior can also be expected for a bimodal pore size distribution consisting of two materials with different electric conductivity and surface area and therefore P1 and P2 could be correlated to the ionic and electric transport in the porous network.

During OER an additional process in the low frequency domain could be registered. Due to its temperature dependence this process does not describe an additional charge transfer process through the oxidation layer of the Ni/Co_3O_4 electrode, but may describe a diffusion of charged species (H^+/OH^-) into the oxide film.

Declaration of Competing Interest

The authors declare that they have no known competing financial interests or personal relationships that could have appeared to influence the work reported in this paper.

Credit authorship contribution statement

Alexander Kube: Conceptualization, Methodology, Investigation, Writing – original draft. **Werner Strunz:** Writing – review & editing, Data curation, Software. **Norbert Wagner:** Funding acquisition, Supervision. **K. Andreas Friedrich:** Writing – review & editing, Supervision.

Funding

The authors would like to thank the European Commission through the project ZAS: “Zinc Air Secondary Innovative Nanotech Based Batteries for Efficient Energy Storage” (Grant Agreement 646186) for financial support. Additionally, I would thank Werner Seybold for building and maintaining the test setup and Alexandra Kube for the fruitful discussions.

References

[1] P. Pei, K. Wang, Z. Ma, Technologies for extending zinc–air battery's cyclelife: a review, Appl. Energy 128 (2014) 315–324.
[2] P. Wang, T. Jia, B. Wang, Review – recent advance in self-supported electrocatalysts for rechargeable zinc-air batteries, J. Electrochem. Soc. 167 (2020) 110564.
[3] Y. Li, H. Dai, Recent advances in zinc–air batteries, Chem. Soc. Rev. 43 (2014) 5257–5275.
[4] K. Harting, U. Kunz, T. Turek, Zinc-air batteries: prospects and challenges for future improvement, Z. für Phys. Chem. 226 (2012) 151–166.
[5] N. Wagner, E. Gülzow, Change of electrochemical impedance spectra (EIS) with time during CO-poisoning of the Pt-anode in a membrane fuel cell, J. Power Sources 127 (2004) 341–347.
[6] J.M.Le Canut, R.M. Abouatallah, D.A. Harrington, Detection of membrane drying, fuel cell flooding, and anode catalyst poisoning on PEMFC stacks by electrochemical impedance spectroscopy, J. Electrochem. Soc. 153 (2006) A857.
[7] V.A. Paganin, C.L.F. Oliveira, E.A. Ticianelli, T.E. Springer, E.R. Gonzalez, Modelisticinterpretation of the impedance response of a polymer electrolyte fuel cell, Electrochim. Acta 43 (1998) 3761–3766.
[8] J.M. Song, S.Y. Cha, W.M. Lee, Optimal composition of polymer electrolyte fuel cell electrodes determined by the AC impedance method, J. Power Sources 94 (2001) 78–84.
[9] A. Sumboja, X. Ge, G. Zheng, F.W.T. Goh, T.S.A. Hor, Y. Zong, Z. Liu, Durable rechargeable zinc-air batteries with neutral electrolyte and manganese oxide catalyst, J. Power Sources 332 (2016) 330–336.
[10] F. Ciucci, Modeling electrochemical impedance spectroscopy, Curr. Opin. Electrochem. 13 (2019) 132–139.
[11] G.A. Futter, P. Gazdzicki, K.A. Friedrich, A. Latz, T. Jahnke, Physical modeling of polymer-electrolyte membrane fuel cells: understanding water management and impedance spectra, J. Power Sources 391 (2018) 148–161.
[12] T. Reshetenko, A. Kulikovsky, PEM fuel cell characterization by means of the physical model for impedance spectra, J. Electrochem. Soc. 162 (2015) F627–F633.
[13] S. Buteau, J.R. Dahn, Analysis of thousands of electrochemical impedance spectra of lithium-ion cells through a machine learning inverse model, J. Electrochem. Soc. 166 (2019) A1611–A1622.
[14] P.J. Weddle, R.J. Kee, T. Vincent, A stitching algorithm to identify wide-bandwidth electrochemical impedance spectra for li-ion batteries using binary perturbations, J. Electrochem. Soc. 165 (2018) A1679–A1684.
[15] T.H. Wan, M. Saccoccio, C. Chen, F. Ciucci, Influence of the discretization methods on the distribution of relaxation times deconvolution: implementing radial basis functions with DRTtools, Electrochim. Acta 184 (2015) 483–499.
[16] E. Ivers-Tiffee, A. Weber, Evaluation of electrochemical impedance spectra by the distribution of relaxation times, J. Ceram. Soc. Japan 125 (2017) 193–201.
[17] D. Wittmaier, S. Aisenbrey, N. Wagner, K.A. Friedrich, Bifunctional, carbon-free nickel/cobalt-oxide cathodes for lithium-air batteries with an aqueous alkaline electrolyte, Electrochim. Acta 149 (2014) 355–363.
[18] A.L. Gavrilyuk, D.A. Osinkin, D.I. Bronin, The use of Tikhonov regularization method for calculating the distribution function of relaxation times in impedance spectroscopy, Russ. J. Electrochem. 53 (2017) 575–588.
[19] N. Florsch, C. Camerlynck, A. Revil, Direct estimation of the distribution of relaxation times from induced-polarization spectra using a Fourier transform analysis, Near Surf. Geophys. 10 (2012) 517–531.
[20] B.A. Boukamp, Fourier transform distribution function of relaxation times; application and limitations, Electrochim. Acta 154 (2015) 35–46.
[21] B.A. Boukamp, A. Rolle, Use of a distribution function of relaxation times (DFRT) in impedance analysis of SOFC electrodes, Solid State Ion. 314 (2018) 103–111.
[22] T.V.D. Noot, Maximum entropy deconvolution of dielectric and impedance data, J. Electroanal. Chem. 386 (1995) 57–63.
[23] T. Hörlin, Maximum entropy in impedance spectroscopy of non-inductive systems, Solid State Ion. 67 (1993) 85–96.
[24] B.A. Boukamp, A. Rolle, Analysis and application of distribution of relaxation times in solid state Ionics, Solid State Ion. 302 (2017) 12–18.
[25] A.L. Gavrilyuk, D.A. Osinkin, D.I. Bronin, On a variation of the Tikhonov regularization method for calculating the distribution function of relaxation times in impedance spectroscopy, Electrochim. Acta 354 (2020) 136683.
[26] F. Ciucci, C. Chen, Analysis of electrochemical impedance spectroscopy data using the distribution of relaxation times: a Bayesian and hierarchical Bayesian approach, Electrochim. Acta 167 (2015) 439–454.
[27] S. Dierickx, A. Weber, E. Ivers-Tiffée, How the distribution of relaxation times enhances complex equivalent circuit models for fuel cells, Electrochim. Acta 355 (2020) 136764.
[28] H. Schichlein, A.C. Müller, M. Voigts, A. Krügel, E. Ivers-Tiffée, Deconvolution of electrochemical impedance spectra for the identification of electrode reaction mechanisms in solid oxide fuel cells, J. Appl. Electrochem. 32 (2002) 875–882.
[29] M. Heinzmann, A. Weber, E. Ivers-Tiffée, Advanced impedance study of polymer electrolyte membrane single cells by means of distribution of relaxation times, J. Power Sources 402 (2018) 24–33.
[30] M. Saccoccio, T.H. Wan, C. Chen, F. Ciucci, Optimal regularization in distribution of relaxation times applied to electrochemical impedance spectroscopy: ridge and lasso regression methods - a theoretical and experimental study, Electrochim. Acta 147 (2014) 470–482.
[31] R. Holze, in: Impedanzmessungen an Porösen Elektroden, Rheinische Friedrich Wilhelms-Universität, Bonn, 1983, p. 148.

[32] X. Yuan, C. Song, H. Wang, J. Zhang, Electrochemical Impedance Spectroscopy in PEM Fuel Cells, Springer-Verlag, London, 2010.
[33] N. Wagner, Electrochemical power sources – fuel cells, in: Y. Barsukov (Ed.), Impedance Spectroscopy: Theory, Experiment, and Applications, Wiley, US, 2018, pp. 497–537.
[34] T. Kessler, W.E. Triaca, A.J. Arvia, Kinetics and mechanism of the oxygen evolution reaction at oxide-coated Co-Ni amorphous alloy electrodes, J. Appl. Electrochem. 24 (1994) 310–315.
[35] Y. Bultel, K. Wiezell, F. Jaouen, P. Ozil, G. Lindbergh, Investigation of mass transport in gas diffusion layer at the air cathode of a PEMFC, Electrochim. Acta 51 (2005) 474–488.
[36] M. Röhe, F. Kubannek, U. Krewer, Processes and their limitations in oxygen depolarized cathodes: a dynamic model-based analysis, ChemSusChem 12 (2019) 2373–2384.
[37] D. Franzen, M.C. Paulisch, B. Ellendorff, I. Manke, T. Turek, Spatially resolved model of oxygen reduction reaction in silver-based porous gas-diffusion electrodes based on operando measurements, Electrochim. Acta 375 (2021) 137976.
[38] J. Fleig, R. Merkle, J. Maier, The $p(O_2)$ dependence of oxygen surface coverage and exchange current density of mixed conducting oxide electrodes: model considerations, PCCP 9 (2007) 2713–2723.
[39] M. Schönleber, E. Ivers-Tiffée, Approximability of impedance spectra by RC elements and implications for impedance analysis, Electrochem. Commun. 58 (2015) 15–19.
[40] U. Pasaogullari, C.Y. Wang, Liquid water transport in gas diffusion layer of polymer electrolyte fuel cells, J. Electrochem. Soc. 151 (2004) A399.
[41] A. Parthasarathy, S. Srinivasan, A.J. Appleby, C.R. Martin, Temperature dependence of the electrode kinetics of oxygen reduction at the platinum/Nafion® interface–a microelectrode investigation, J. Electrochem. Soc. 139 (1992) 2530–2537.
[42] M.H. Miles, G. Kissel, P.W.T. Lu, S. Srinivasan, Effect of temperature on electrode kinetic parameters for hydrogen and oxygen evolution reactions on nickel electrodes in alkaline solutions, J. Electrochem. Soc. 123 (1976) 332–336.
[43] L.X. Jinli Qiao, Lei Ding, Penghui Shi, Lei Zhang, Ryan Baker, Jiujun Zhan, Effect of KOH concentration on the oxygen reduction kinetics catalyzed by heat-treated Co-pyridine/C electrocatalysts, Int. J. Electrochem. Sci. 8 (2013) 1189–1208.
[44] S. Cruz-Manzo, P. Greenwood, An impedance model based on a transmission line circuit and a frequency dispersion Warburg component for the study of EIS in Li-ion batteries, J. Electroanal. Chem. 871 (2020) 114305.
[45] J.P. Meyers, M. Doyle, R.M. Darling, J. Newman, The impedance response of a porous electrode composed of intercalation particles, J. Electrochem. Soc. 147 (2000) 2930.
[46] A. Dhanda, H. Pitsch, R. O'Hayre, Diffusion impedance element model for the triple phase boundary, J. Electrochem. Soc. 158 (2011) B877.
[47] M. Heinzmann, A. Weber, E. Ivers-Tiffée, Impedance modelling of porous electrode structures in polymer electrolyte membrane fuel cells, J. Power Sources 444 (2019) 227279.
[48] B.A. Boukamp, Distribution (function) of relaxation times, successor to complex nonlinear least squares analysis of electrochemical impedance spectroscopy? J. Phys. Energy 2 (2020) 042001.
[49] T. Kessler, J.R. Vilche, M. Ebert, K. Jüttner, W.J. Lorenz, Electrochemical impedance spectroscopy of oxygen and hydrogen evolution on amorphous alloys in 1 M KOH, Chem. Eng. Technol. 14 (1991) 263–269.
[50] H. Willems, A.G.C. Kobussen, J.H.W. De Wit, G.H.J. Broers, The oxygen evolution reaction on cobalt: part I. Reaction order experiments and impedance measurements, J. Electroanal. Chem. Interfacial Electrochem. 170 (1984) 227–242.
[51] E. Laouini, M. Hamdani, M.I.S. Pereira, J. Douch, M.H. Mendonça, Y. Berghoute, R.N. Singh, Electrochemical impedance spectroscopy investigation of spinel type cobalt oxide thin film electrodes in alkaline medium, J. Appl. Electrochem. 38 (2008) 1485.

Journal of The Electrochemical Society, 2021 **168** 050531
1945-7111/2021/168(5)/050531/8/$40.00 © 2021 The Electrochemical Society ("ECS"). Published on behalf of ECS by IOP Publishing Limited

Influence of Organic Additives for Zinc-Air Batteries on Cathode Stability and Performance

Alexander Kube,[1,z] Norbert Wagner,[1] and Kaspar Andreas Friedrich[1,2]

[1] *German Aerospace Center, 70569 Stuttgart, Germany*
[2] *University of Stuttgart, Institute of Building Energetics, Thermal Engineering and Energy Storage (IGTE), 70569 Stuttgart, Germany*

In this work, a theoretically predicted electrolyte composition comprising 6 M potassium hydroxide (KOH), 2 M citric acid, 1 M glycine, and 0.5 M zinc oxide is tested in terms of electrochemical performance, cathode stability, and electrolyte stability. It is shown that dissolved metal ions from the cathode reacted with the introduced organic additives, reduced the cathode stability, and blocked metal oxidation reactions. This was due to a Kolbe-like decomposition reaction that occurred because of the presence of potassium citrate, which formed because of the reaction of KOH and citric acid. Furthermore, intermediate products of this decomposition reaction appeared to block the cathode's surface, hindering oxygen (O_2) evolution and reducing the overall cell performance. The decomposition of potassium citrate starts above 1.7 V Zn. Additionally, it is shown that tribase citric acid behaves similarly to a dibase carbonic acid. Both decrease the onset potential for the O_2 reduction reaction from 0.9 V vs reversible hydrogen electrode (RHE) for pure 6 M KOH to 0.6 V vs RHE for KOH with these organic acids.
 [DOI: 10.1149/1945-7111/abff63]

Manuscript submitted November 11, 2020; revised manuscript received April 7, 2021. Published May 19, 2021.

The demand for clean energy has led to a growing need for high energy density, safe, and cost-effective energy storage solutions to prepare for periods when sunshine is lacking and no wind blows. This demand directed the attention to zinc (Zn)–air batteries, as they do possess these properties and have been well-established and developed as primary batteries in various applications, e.g., hearing aids. The challenge is to further develop these Zn–air batteries as secondary batteries because they have poor energy efficiency and low cycle life.[1] These negative traits arise from high overpotentials during charge and discharge, associated with the sluggish kinetics of oxygen (O_2) reduction and evolution. Particularly, the cathode, which requires bifunctionality in the form of a two-electrode cell design for Zn–air batteries, necessitates stringent material selection criteria to achieve both high activity and long durability during charge and discharge.

Passivation of the anode due to zinc oxide (ZnO) formation and dimensional changes of the electrode hinder the cycling stability of these batteries.[2] To mitigate the unstable anode, the electrolyte is supplemented with additives, which are reported to have a positive influence on Zn deposition and maintaining the fine-pored structure of the anode.[3–6] Besides the inhibition of dendrite growth, it was reported that additives decreased the hydrogen (H_2) evolution rate. Various additives, such as sodium dodecylbenzene sulfonate (SDBS),[6] polyethylene glycol,[7] tartaric/succinic/citric acid,[8,9] and tetra-alkyl ammonium hydroxides[8,10] have been investigated and showed the ability to inhibit both dendrite growth and H_2 evolution. Besides the inferior cycling stability of the anode, the electrolyte's CO_2 uptake, based on a high pH value, is a significant issue related to battery life. This uptake reduces the conductivity of the electrolyte and thus increases overpotentials; it also blocks the pores of the gas diffusion electrode due to the precipitation of carbonates, e.g., K_2CO_3 and $ZnCO_3$.[11–13] Stamm et al. found that the lifetime of Zn–air button cells was limited to approximately 40 days because of the uptake of CO_2.[14] Ko et al. showed that the uptake of CO_2 also passivated the anode's surface, leading to a decrease in capacity.[15]

To minimize battery performance loss in an alkaline system due to increasing CO_2 concentration, an electrolyte with a lower pH is required, whereby the pH value should be alkaline at all times during battery operation, enabling ZnO formation. The lower pH will reduce the CO_2 uptake rate;[16] as a representation of this effect, the equilibrium in Eq. 1 will shift to the left side of the reaction equation, whereas in the case of a higher pH, it will shift to the right.[17]

$$H_2CO_3 + 2KOH \rightleftharpoons K_2CO_3 + H_2O \quad [1]$$

Accordingly, lower pH values for electrolytes can enable a longer battery life because of the lower CO_2 uptake rate and the reduced formation of precipitates.

Despite the drawbacks of alkaline electrolytes, they are applied as standard in Zn-air batteries because of their high reaction rate. This is related to the exchange current density, which increases with an increase in potassium hydroxide (KOH) molarity[18] because of the dependence of the reaction rate on the concentration of reaction products. Additionally, alkaline electrolytes have high ionic conductivity,[19] and the electrode thickness is only limited by transport limitations due to the conversion of Zn to ZnO. Because of this conversion and the precipitation of ZnO, no solubility limits are applicable, as is the case for acidic electrolytes. There is also less H_2 gassing in an alkaline environment compared with an acidic environment. For this reason, we believe that alkaline systems are preferable for Zn-air batteries.

Acidic electrolytes show higher Zn solubility,[20,21] and are not prone to problems linked to the formation of carbonates since they exist within a protonated state (similar to H_2CO_3 or HCO_3^-) rather than CO_3^{2-}. This limits their tendency to precipitate in combination with Zn^{2+}. However, commercial batteries are manufactured without excess electrolytes, which limits battery capacity. This is due to the presence of solely Zn^{2+} and the absence of ZnO in acidic electrolytes, as denoted in the Pourbaix diagram.[22] Some commercial secondary Zn-air systems utilize flow batteries to mitigate problems related to solubility limits. However, given the need for additional equipment such as pumps, this technology requires additional space and weight. This limits their usability to applications where weight and space requirements are not crucial.[23] Another issue of using acidic electrolytes is that Zn is more susceptible to corrosion[24] and has a high solubility in acidic electrolytes.[25]

Electrolytes with a pH close to neutral are resilient against both carbonation and corrosion and have reasonable Zn solubility.[19] However, the pH can become unstable because of the low diffusion of ammonia, and non-ZnO products can precipitate; this was illustrated in a simulative work for an electrolyte comprising NH_4Cl and $ZnCl_2$.[26] Nonetheless, results by Jindra et al.[27] show that NH_4Cl-based electrolytes are remarkably promising in this context. Goh et al.[28] further developed this type of electrolyte for an electrolyte mixture of NH_4Cl and $ZnCl_2$ and showed an operation time of 100 h. Additional research by Clark et al. showed that this composition could indeed extend the lifetime of rechargeable Zn–air batteries; however, it also indicated that the pH can become strongly

[z]E-mail: alexander.kube@dlr.de

acidic during charging and that ZnO is not the dominant precipitate,[29] which may limit the capacity in the same manner as described for acidic electrolytes. Sumboja et al. showed in 2016 that a near-neutral electrolyte system, based on NH_4Cl and NH_4OH, demonstrated an operation time of 2,000 h and approximately 500 cycles. These results indicate the potential of such systems.[30]

For the stability of the cathnode materials, a pH value close to neutral indicates advantages and, accordingly, will increase the overall cycle stability of the battery. Beside the reduced carbon uptake in near-neutral electrolytes, lower pH values also influence the reaction kinetics. As noted above, the exchange current density depends on the concentration of reaction products, which also applies to near-neutral pH values where fewer reaction products are available.[27] A disadvantage of these near-neutral electrolytes is that they still are slightly acidic, which may limit the amount of usable and affordable catalysts. Iruin et al. investigated the stability of manganese dioxide (MnO2) in an $NH_4Cl/ZnCL_2$ electrolyte at pH 4 and 8 (the pH was adjusted using NH_4OH). Their results showed that the catalyst was unstable in the acidic environment but had good stability in a slightly alkaline media. Additionally, their results indicated higher overpotentials for the electrolyte set to pH 4.[31] This corrosion in an acidic environment had likely been due to the chloride-based electrolytes used.[19,25]

Clark et al. investigated a near-neutral electrolyte containing organic acids, which worked similar to the additives used in alkaline electrolytes.[32] This electrolyte was designed to maintain a stable pH in an alkaline regime and precipitate ZnO. The formulation that the study derived comprised citric acid, KOH, glycine, and ZnO. Citric acid was used for its high pH buffering capacity and its transport properties.[33] It was also reported that organic additives with hydrophilic carboxyl groups could inhibit dendrite growth.[19] Glycine served as the primary pH buffer because of its 9.6 pKa value for the amino acid group but showed only low ionic conductivity.[34] Zinc oxide was used to reduce the diffusion velocity of dissolved Zn from the anode into the bulk electrolyte and was instead precipitated near the location of dissolution location. The goal of this formulation was to address the shortcomings of NH_4Cl electrolytes by investigating the following: (i) avoiding the observed drop to extremely acidic pH values during charging due to NH_4 buffer limitations and (ii) precipitating ZnO instead of Zn chloride hydroxide and Zn ammonia chloride. Their study[33] demonstrated that these goals could be achieved. However, the researchers noted that the organic molecules likely oxidized at the cathode during the charging process and may even have replaced the electrolyte during the experiment. The oxidation of the organic components is not investigated in detail in their publication, only hypothetically discussed. The focus of the current work is to address this gap and experimentally show whether the oxidation of organic components takes place and whether this influences the stability and electrochemical performance of the cathodes. To do so, electrodes with either nickel (Ni) or silver (Ag) as a conductive additive; Co_3O_4, MnO_2, or $NiCo_2O_4$ as a catalyst; and Polytetrafluoroethylene (PTFE) as a binder and hydrophobic agent were used.

Experimental

Preparation of the electrolyte.—The electrolyte composition was based on the work of Clark et al. and included the following: 6 M KOH, 2 M citric acid, 1 M glycine (biotechnology grade, VWR International), and 0.5 M ZnO (Sigma Aldrich) but with the modification of directly using 2 M potassium citrate (⩾99%, Sigma Aldrich). This was due to the strongly exothermic reaction of KOH and citric acid while forming potassium citrate, as shown in Formula 2 below:

$$3KOH + C_6H_8O_7 \rightleftharpoons C_6H_5K_3O_7 + 3H_2O\ \Delta H = -4911.27\ \text{kJ mol}^{-1} \quad [2]$$

Citric acid was used to gel the electrolyte, thereby reducing anode shape changes during cycling. Additionally, citric acid was also used as a secondary pH buffer, whereas glycine served as a primary pH buffer. All components were stirred with a magnetic mixer until dissolved, and a clear solution was obtained. This electrolyte is abbreviated herein as the mixture with organics (mix-wo).

Electrode manufacturing.—The electrodes in this work comprised a 70 wt% conductive additive, a 20 wt% catalyst (<50 nm, Sigma Aldrich), and PTFE (TF9207Z, 3 M Dyneon). As a conductive additive, either Ni (3–7 μm, Strem Chemicals) or Ag (type 311, Ferro Ag) was used. Both of these materials were electrochemically active and helped the catalyst increase the overall performance of the electrode. For catalysts, either Co_3O_4 (<50 nm, Sigma Aldrich), electrolytic MnO_2 (Tosoh Hellas), or nickel cobalt oxide ($NiCo_2O_4$, Cerpotech) was tested.

Materials were physically mixed in a knife mill, and the obtained powder was filled into a mossy frame together with a metal mesh (0.125 mm, Haver & Boecker) and finally pressed at 300 kN m^{-2} for 1 min in a hydraulic press. Next, the mossy frame was removed, and the electrode was again pressed using the same parameters. The obtained electrode was heat treated in an oven for 1 h at 340 °C as described by Wittmaier.[35]

Electrochemical half-cell tests.—Electrodes were tested in a homemade half-cell setup.[36] To improve electrical contact and gas distribution, a gas diffusion layer (GDL, Sigracet 29BC) was mounted between the gas compartment and the. The cell was submerged in a 1 l electrolyte container and placed in a heatable water bath set to 25 °C. The cell was connected to a potentiostat (Zahner-Elektrik, Germany). A Gaskatel reversible H_2 electrode (RHE) was used as a reference electrode, and O_2 was used as the pure feed gas. Cyclic voltammetry (CV) was performed in a range of 0.3–1.8 V vs RHE with a scan rate of 1 mV s^{-1}.

Gas chromatography.—Gas chromatography (GC) measurements were performed in a homemade full-cell with a 4 ml electrolyte compartment. A circular, 250-μm-thick Zn foil, 18 mm in diameter, was used as an anode; a gas diffusion electrode comprising 70 wt% Ni, 20 wt% Co_3O_4 and 10 wt% PTFE was applied as a cathode. The cell was operated at room temperature with N_2 as a feed gas and connected to a potentiostat (Zahner-Elektrik, Germany).

A Varian-CP-4900 micro-GC with three channels was used with N_2 as a feed gas. Channel 1 was used with a 20 M molecular sieve (MS5) to measure O_2 and carbon monoxide (CO), and channel 2 was used with a 10 M molar sieve (BBQ) for CO_2 detection. Both channels were internally used with helium, whereas channel 3 was used with argon and a 10 M molar sieve (MS5) to measure H_2.

X-ray diffraction (XRD) spectra were measured with a Bruker D8 Discover mounted with a CuK_α source. Scanning electron microscope (SEM) images were taken using a Zeiss Ultra Plus microscope.

The ionic conductivity was measured using a Philips PW9512/01 electrode with a potentiostat. Electrochemical impedance spectroscopy spectra were recorded at the open circuit potential (OCP).

Results and Discussion

Influence of additives on electrochemical performance.—For a first comparison of the mixture with organics mix-wo (comprising 2 M potassium citrate, 1 M glycine, and 0.5 M ZnO) and KOH, and for reviewing the influence of the components on electrochemical performance, CV measurements using the above-described parameters were recorded for the electrolytes listed in Table I.

Figure 1a shows the CVs of cathodes with Ni as a conductive additive and Co_3O_4 as a catalyst in the mix-wo, the mix-wo without ZnO, as well as glycine and potassium citrate at pH 9. Figure 1b shows 6 M KOH and mixtures of 6 M KOH with the single electrolyte components. These mixtures were used to distinguish between the influences evoked by different electrolyte conductivities and the effects due to the nature of the additives.

Table I. List of used electrolyte compositions and corresponding ionic conductivities and pH values at 25 °C.

Number	KOH (M)	Potassium citrate (M)	Glycine (M)	ZnO (M)	Ionic conductivity (mS cm^{-1})	pH
1	6	—	—	—	585	>14
2	6	—	—	0.5	452	>14
3	6	—	1	—	584	>14
4	6	2	—	—	218	>14
5	6	2	1	0.5	209	11.1
6	—	—	1	—	91	9
7	—	2	—	—	242	9
8	6	2	1	—	209	10.6

For all mixtures with an excess of KOH in Fig. 1b, except the one with potassium citrate, oxidation and reduction peaks of nickel were observed, which are described in more detail by Lyons et al.[37] Conversely, none of the mixtures with an excess of organics showed these oxidation and reduction peaks.

The comparison of electrochemical performance using 6 M KOH and the mix-wo was accomplished by evaluating the maximum current reached for the oxygen evolution reaction (OER) and oxygen reduction reaction (ORR) in the CVs. Figure 1 shows that adding the organic elements drastically decreases the electrochemical performance. In the 6 M KOH for instance, 200 mA cm^{-2} was achieved for OER and 77 mA cm^{-2} for ORR; only 2.9 and 0.16 mA cm^{-2} were achieved for OER and ORR in the mix-wo.

Moreover, the onset potential for ORR shifted from 0.9 V vs RHE for KOH-based systems to 0.55–0.6 V vs RHE for the organic mixtures without an excess of KOH. This finding resulted in an increased overpotential during the discharge of the battery.

When excluding ZnO in the mixture (as shown in Fig. 1a), an increase in current density was observed for both reactions but with less effect on the ORR than on the OER. This increase in electrochemical performance can be explained by the formation of complexes between the organic compounds. This phenomenon is known to occur in the presence of glycine and ZnO,[38] but the same applies for potassium citrate and ZnO. Due to bivalent Zn ions, complexes with several organic groups might be possible. The formation of complexes of the molecules increases the viscosity of the electrolyte and may influence ionic transport; however, this is not represented by the measured conductivities (Table I). It is shown that both the mix-wo without ZnO and the potassium citrate at pH 9 showed higher activities for OER, whereas the reaction began at approximately 1.2 V vs RHE, which is a rather low potential. This may indicate that decomposition of the organics occurs as a side reaction to the charge transfer in the case in which the stabilization of the complexes formed with the ZnO is absent.

Glycine at pH 9 showed a comparable current density to the mixture with organics for OER but had higher current densities during ORR and only half the ionic conductivity. This indicated that the complete mixture with all its components appeared to inhibit both reactions.

Besides a higher viscosity, due to complex formation by the organic molecules with ZnO, several other reasons could explain the electrochemical performance loss. A blockade of active centers, which is known for fuel cells,[39–41] may potentially occur by adsorption of organic molecules onto the surface of the active cathode material, leading to suppressed O_2 and hydroxide ions' adsorption. Because of the high concentrations of organics, particularly potassium citrate, such adsorption was feasible. Citric acid is often used as a ligand for metal nanoparticles because it forms stable complexes with them.[42,43] Potassium citrate may react in a reaction similar to Kolbe electrolysis (Eqs. 3–5), in which adsorbed intermediate products block the surface.

$$2RCOO^- \rightarrow 2RCOO\cdot + 2e^- \quad [3]$$

$$2RCOO\cdot \rightarrow 2R\cdot + 2CO_2 \quad [4]$$

$$R\cdot + R\cdot \rightarrow R - R \quad [5]$$

This surface coverage may result in either the changed steady-state coverage of O and OH^-, which will alter the reaction rate. Alternatively, the presence of such intermediate products may raise the activation energy of O_2 evolution by weakening the bonding of adsorbed intermediate species.[44] Additionally, adsorbed species may block the surface coverage of water molecules. This hypothesis is supported by the test of potassium citrate in 6 M KOH, as shown in Fig. 1b. Although ZnO and glycine did not indicate a significant influence on electrochemical performance or ionic conductivity, the addition of potassium citrate to 6 M KOH drastically reduced the

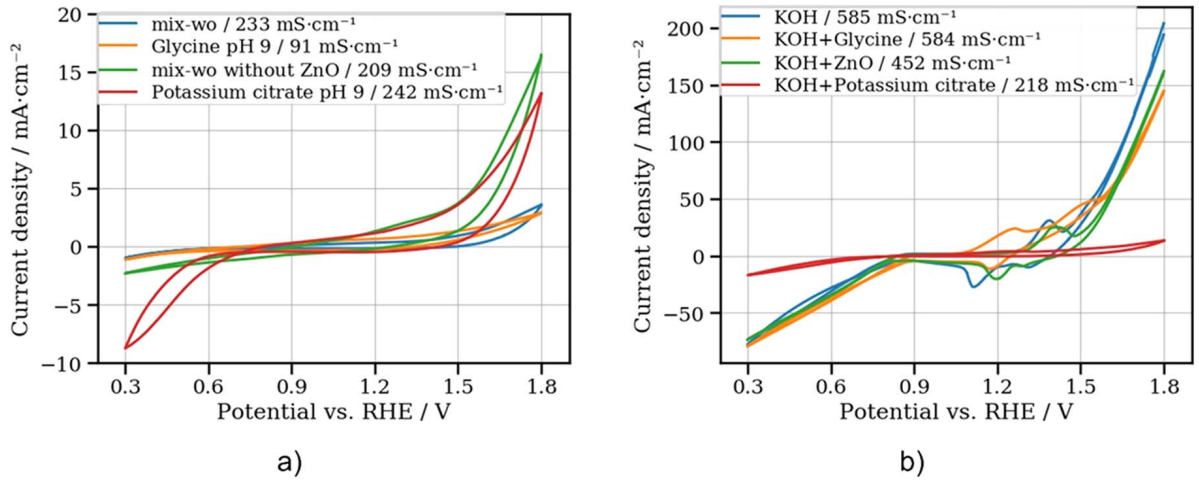

Figure 1. Cyclic voltammograms at 1 mv*s^{-1} for different electrolyte compositions at pH 9 (a) and in 6 M KOH (b) at 25 °C with O_2 as feed gas and 1 l electrolyte.

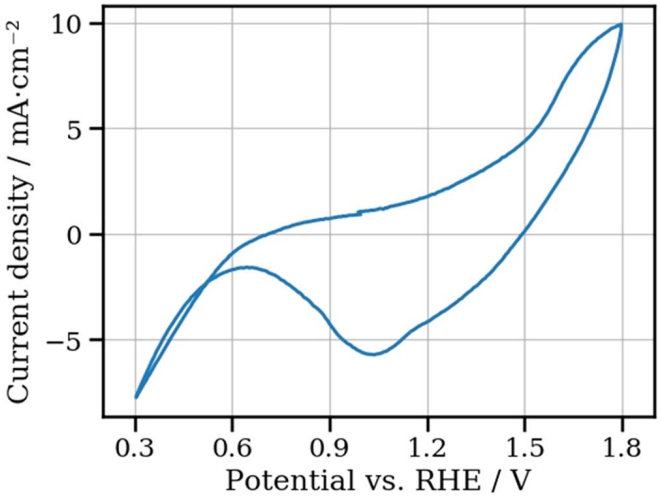

Figure 2. Cyclic voltammograms for 6 M KOH saturated with CO_2 at 25 °C with O_2 as feed gas and 1 l electrolyte.

electrochemical performance. Concurrently, the ionic conductivity was reduced and was comparable with the ionic conductivity of the mixture with organics. This may have been due to the suppression of the extraordinary conductivity of the KOH electrolyte. The well-known extraordinary conductivity and ionic transport capabilities of hydroxide ions are related to structural diffusion, an effect known as the Grotthus mechanism.[45] Carbon dioxide, evolved by the decomposition of organics by Kolbe electrolysis, forms the dibasic carbonic acid that consumes hydroxide ions,[46] as shown in Eqs. 6–8.

$$CO_2(g) \rightleftharpoons CO_2(aq) \quad [6]$$

$$CO_2(aq) + H_2O(l) \rightleftharpoons H_2CO_3(aq) \quad [7]$$

$$H_2CO_3(aq) + OH^-(aq) \rightleftharpoons HCO_3^- + H_2O(l) \quad [8]$$

The consumption of hydroxide ions reduces ionic concentration and has a strong effect on lowering the conductivity of the electrolyte, thereby enabling the achievable power density (see Fig. 2) for CO_2-saturated KOH. This shift in ionic transport, from the high concentrations of extremely mobile hydroxide ions to lower concentrations of less mobile organic charge carriers, as well as the higher viscosity of the electrolyte, may explain the lower ionic conductivity. Besides the comparable current density of the mixture with organics and the CO_2-saturated KOH, Fig. 2 shows the same onset potential for ORR at approximately 0.6 V vs RHE, as well as the absence of characteristic oxidation and reduction peaks.

Since citric acid is a tribase acid, it behaves similarly to dibase carbonic acid. Besides there being the same mechanisms between carbonic and citric acid, the oxidation of organics during anodic operation can lead to CO_2 evolution and, as such, could explain the same observed behavior. Since 1 l electrolyte was used for each test, this effect would not initially have been observable. Instead, it would have arisen slowly, if oxidation of the organics had been the cause. This was not the case for all tests conducted; thus, it can be assumed that the investigated acids do have the same reaction mechanisms.

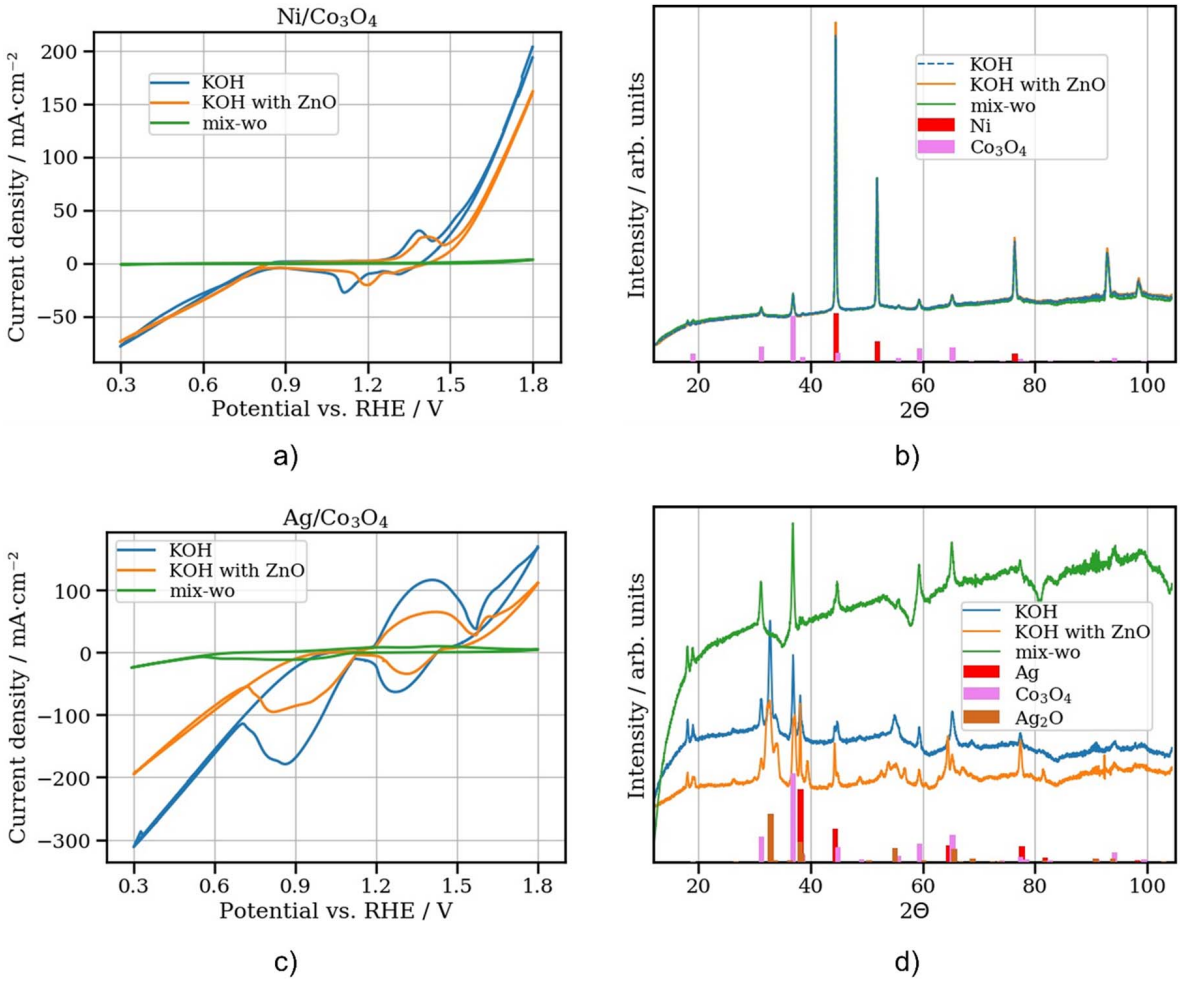

Figure 3. Cyclic voltammograms at 25 °C with O_2 as feed gas and 1 l electrolyte for a Ni/Co_3O_4 electrode (a) and an Ag/Co_3O_4 electrode (c) and X-ray diffraction spectra for the Ni/Co_3O_4 electrode (b) and the Ag/Co_3O_4 electrode (d).

By adding potassium citrate, ionic conductivity was decreased to 218 mS cm^{-2}, which is still almost double the value of CO_2-saturated KOH (118 mS cm^{-2}). Since the achieved performance for the mixture with organics was lower than for CO_2-saturated KOH, it can be assumed that both described effects, namely the formation of surface coverage by organics as well as an inhibition of electrolyte conductivity, were responsible for performance loss.

Influence of additive deposits onto electrode components.— Besides the electrochemical performance, it is of great interest to determine if and how electrode materials react with the used additives. To review this, CV was performed for an electrode comprising 70 wt% Ni, 20 wt% Co_3O_4, and 10 wt% PTFE (Fig. 3a) and for an electrode comprising 70 wt% Ag, 20 wt% Co_3O_4, and 10 wt% PTFE for KOH, KOH with ZnO, and the mixture with organics (Fig. 3c). The XRD spectra and SEM images were recorded after the CVs. Both electrodes showed the same lower performance when the organic additives were used for OER. For ORR, the Ag-based electrode showed some electrochemical activity. Furthermore, no characteristic peaks for oxidation or reduction reactions were observed in the measured CVs for the Ni-based electrode, whereas for Ag, these peaks were observable but depressed. This indicates that Ag was only partially oxidized. During these oxidation and reduction processes for Ag, Ni, and cobalt oxide (Co_3O_4), metal ions may have partially dissolved, as was already established for Ag.[47]

As described above, citric acid is used as a ligand for nanoparticles and strongly adsorbs on metals. Consequently, the surface and, accordingly, the active sites were blocked, resulting in suppressed oxidation and reduction reactions. The depressed peaks indicate this blockage, as the peaks were associated with the formation of surface hydroxides. Another possible explanation is the formation of radicals because of the Kolbe electrolysis reaction of potassium citrate on the electrode's surface as described by Eqs. 3–5.[44] These radicals may attack the electrode material and, in doing so, induce a dissolution process for the catalyst. Postmortem analysis with XRD showed no significant difference in spectra between KOH and the mixture with organics for the Ni-based electrode (Fig. 3b); however, large differences were indicated for the Ag-based electrode (Fig. 3d). The observed increase of background for the Ag-based electrode may have occurred for several reasons. The highest background could be observed for the mix-wo electrolyte because of the amorphous precipitation of Ag and the fluorescence of the cobalt. The difference between KOH and KOH saturated with ZnO was smaller and could be explained by the lower diffusion coefficient of Ag ions in the electrolyte.

Because of this lower diffusion coefficient, solubility limits were achieved faster, and precipitation occurred near the area of dissolution. This would lead to a lower reorganization of the Ag particles during cycling.

Another possibility concerns the changed activity coefficients of Ag due to the presence of Zn ions, which may change the solubility limit of Ag, leading to slower diffusion coefficients for Ag ions as explained above. For pure KOH, the higher diffusion rate and higher solubility limits may have given rise to the precipitation of Ag onto, for example, the catalyst particles. In XRD images, these amorphous particles were shown to give rise to a higher background, as depicted in Fig. 3d. In comparison, the mixture with organics showed neither clear Ag nor Ag oxide peaks. Only the Co_3O_4 showed clear characteristic peaks, which were comparable with the other two measurements in KOH and KOH with ZnO. This absence of Ag

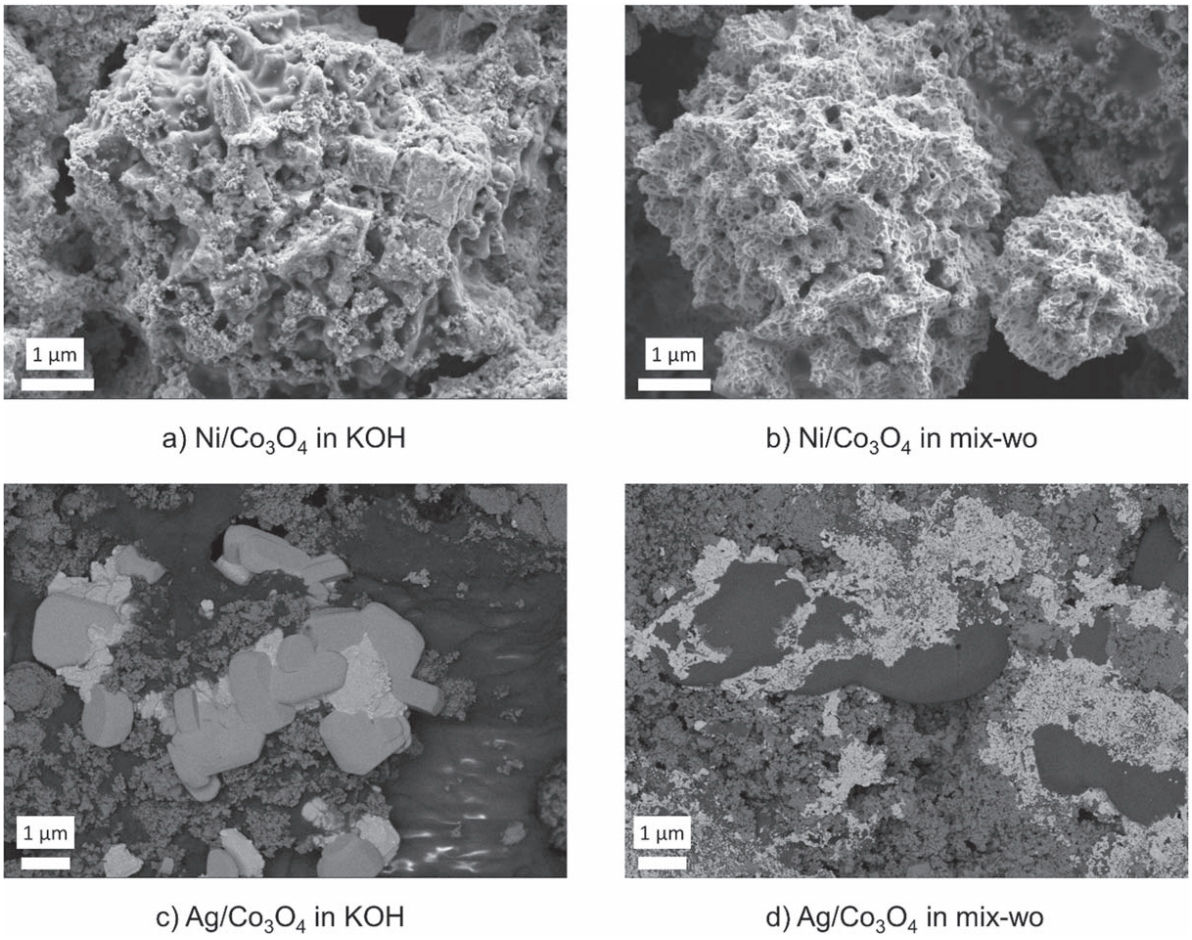

Figure 4. Scanning electron microscope imaged of Ni/Co_3O_4 electrodes operated in KOH (a) and the mix-wo (b), and for the Ag/Co_3O_4 electrode operated in KOH (c) and the mix-wo (d) after cycling.

peaks may have been due to amorphous precipitation with an increased background signal. Another possible explanation for the increased background could be precipitation and nucleation at <1 nm particles or partial dissolution of the Ag particles.

To further strengthen this conclusion, Fig. 4 shows the SEM spectra for electrodes operated in KOH and the mix-wo after cycling. The Ag-based electrode is shown in Fig. 4d as a back-scattered electron image after cycling in the mix-wo. In this image, the light gray color indicates Ag, and the darker part represents Co_3O_4. Although the image taken after KOH cycling clearly showed Ag particles in the micrometer range, no such particles can be observed in the mix-wo in the image taken after cycling. Instead, smaller Ag precipitations can be observed as brighter areas distributed across the surface.

For the Ni/Co_3O_4 electrode, Ni particles could still be found, without significant changes in size and observably exhibiting pitting corrosion. This explains why no changes in the XRD spectra were observable since XRD characterizes the bulk phase and not the surface. Accordingly, the measured spectrum appeared unchanged but, on closer inspection, clearly showed the deterioration of metallic materials in these organics. It can be assumed that the same applies to the Co_3O_4 because it has a comparable oxidation and reduction processes with Ag and Ni.

Up until this point, only Co_3O_4 had been used as a catalyst. Figure 5 shows the measurement for MnO_2 and $NiCo_2O_4$ mixed with Ni. Electrolytic manganese dioxide is one of the most-used catalysts for Zn–air batteries because it is abundant and cost-effective. Furthermore, $NiCo_3O_4$ shows good performance in KOH and high stability. All three catalysts showed the same low performance if the mix-wo is used. Furthermore, no clear oxidation or reduction peaks were observed for all three; however, Co-containing electrodes showed an increase in current density during OER, starting at 1.2–1.4 V vs RHE. This may be an indication that the decomposition reaction of the organics is favored for Co-containing electrodes.

Gas and pH analysis.—Besides the influence of additives on the cathode itself, the stability of organic additives in electrolytes for Zn–air batteries must be considered. To characterize this, a full-cell setup with 70 wt% Ni, 20 wt% Co_3O_4, and 10 wt% PTFE electrode as a cathode and a Zn foil as an anode was used to analyze the gas composition of the gas outlet (Fig. 6). In these instances, the color red represents the applied potential, blue is the O_2 signal, yellow is the H_2 signal, and green is the CO_2 signal. The potential was increased in a stepwise manner. Since the gas needed a few seconds to get through the pipes into the GC to be measured, a moderate time shift may have occurred. For both of the measured electrolytes, a decay of signal intensity was observed for O_2 and CO_2, indicating rest impurities derived in the pipes. After the stabilization of the signals, the KOH test (Fig. 6a) showed low O_2 evolution, starting at 1.7 V vs Zn, which increased with each potential step until the battery was fully charged at 37 h. After reaching 100% State of Charge, the amount of evolved O_2 dropped drastically, and combined O_2/H_2 evolution began. During the entire test, no CO_2 evolution was observed, in contrast to the test for the mixture including organics (Fig. 6b). This demonstrates that the used GDL was not the source of the observed CO_2 evolution; instead, this source was the decomposition of the organic components of the electrolyte. In Fig. 6b, no gas evolution can be observed for potentials below 1.7 V vs Zn. Above this potential, CO_2 began to evolve with increasing signal intensity for increased potentials. At 1.8 V vs Zn, H_2 evolution was observed besides the CO_2 signal. Both signals indicate the oxidation process of the organic compounds and thus the instability of the used electrolyte. Since the O_2 signal was stable during all potential steps and showed comparable values with the KOH measurement before O_2 evolution, it can be assumed that no O_2 had been produced during the measurement.

To further understand the stability of the organic additives, the same test was conducted with additional pH monitoring as depicted in Fig. 7. Figure 7a shows the measurement for the complete mixture with organics; Fig. 7b shows the measurement for potassium citrate. Potassium ions provide charge neutrality to balance the citrate ions. Therefore, 2 M of pure potassium citrate showed a pH value close to 7; the addition of glycine increased the pH to higher values. This indicates that the observed increase in pH during charging had been due to the decomposition of potassium citrate, which increased the number of hydroxide ions in the electrolyte. The degradation of glycine will result in a pH drop back to a value close to 7. As shown in Fig. 7a, at 1.8 V vs Zn, a small increase in pH is observable, whereas at 2 V vs Zn, a decrease is shown. This indicates that glycine is only stable for up to 2 V vs Zn. A comparison with Fig. 7b, where potassium citrate is measured without glycine, supports this interpretation. Here, an increase in pH can be observed starting with 1.7 V. vs Zn. This supports that the observed small increase in pH with a decrease at higher potentials is associated with the decomposition of potassium citrate. It is noted that the presence of glycine, which acted as a buffer, led to a rather small pH increase as depicted figure Fig. 7a). On the basis of these observations, the CO_2 evolution during the GC test can be explained by the decomposition of potassium citrate. The decomposition of potassium citrate and the resulting CO_2 evolution is an additional indicator of a Kolbe electrolysis-like reaction on the part of potassium citrate.

Comparison with other organic electrolytes for Zn–air batteries.—Because of the instability of potassium citrate, other organics should be used to favor smooth Zn deposition. Hosseini et al.[48] used 7 M KOH with a Dimethyl sulfoxide (DMSO) additive.

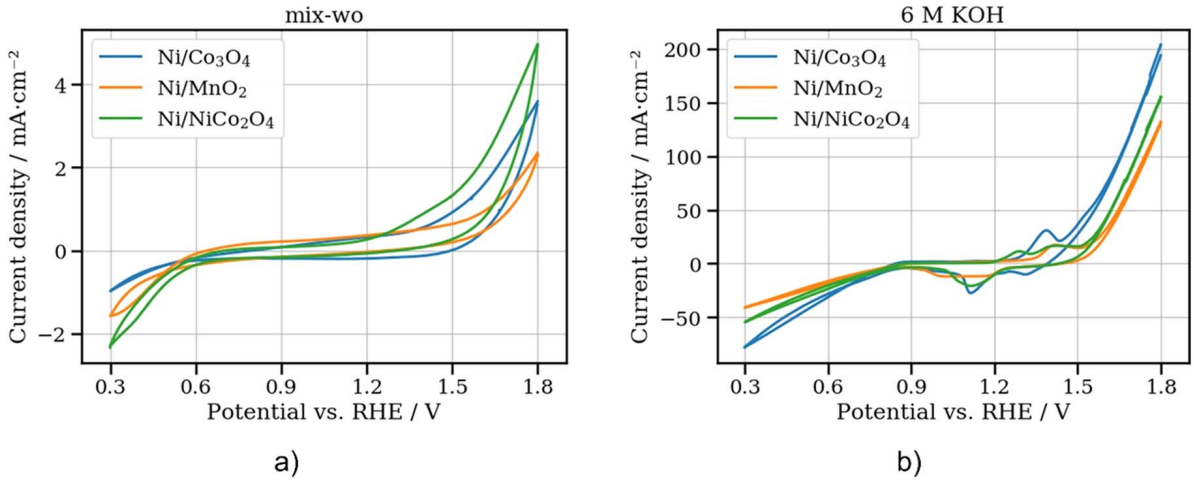

Figure 5. Cyclic voltammograms for MnO_2, CO_3O_4; and $NiCo_2O_4$ in 6 M KOH and the mixture with organics.

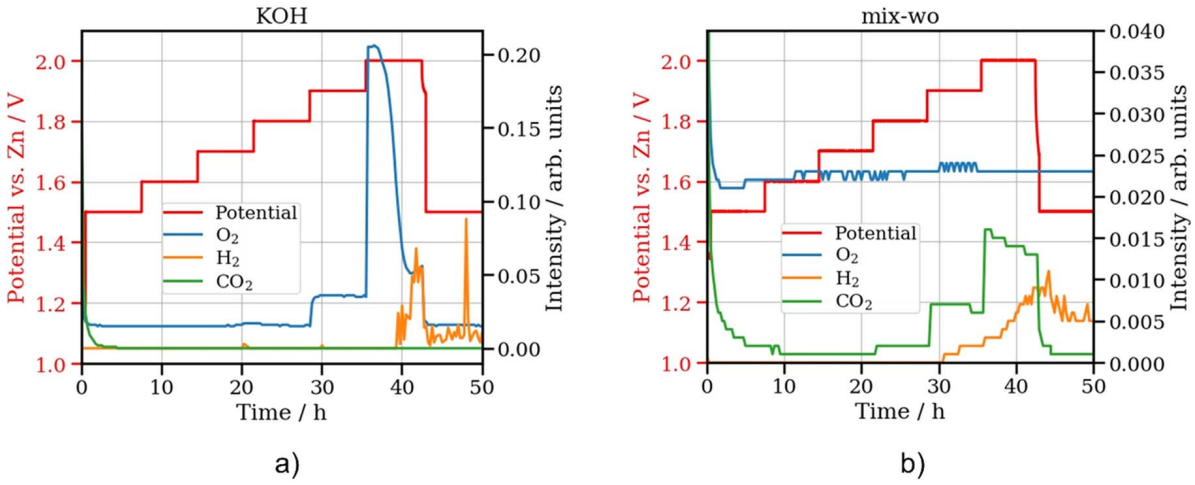

Figure 6. Gas analysis during charging with gas chromatography for 6 M KOH (a) and the mixture with organics (b) at room temperature with N_2 as feed gas.

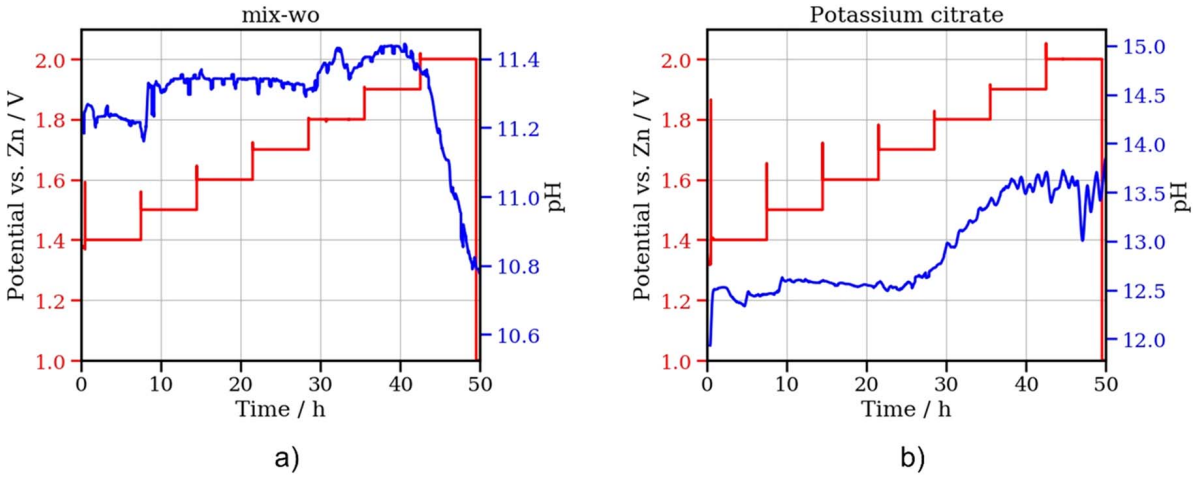

Figure 7. Monitoring of pH during charging for increasing potentials at room temperature, and ambient air as feed gas for the mixture with organics (a) and 2 M potassium citrate (b).

With this approach, a 20% increase in the discharge capacity was shown. Furthermore, the high cycle life of this mixture indicates very stable charge and discharge voltages for more than 500 cycles. Additionally, the DMSO in KOH formed long chains, thus acting as a gelling agent and, as such, reducing water loss.

Xiao et al.[49] investigated the influence of benzotriazole, thiourea, and SDBS as additives. These improved the cycle stability of a Zn–air battery and enhanced its discharge capacity. The study showed stable charge and discharge voltages for more than 60 cycles but with a high charge cut-off voltage above 2.4 V and a discharge cut-off voltage of 0.2 V, which is quite low and may lead to capacity loss due to type 2 ZnO formation, which is extremely dense compared with the mossy type 1 ZnO, and, as such, is not accessible for electrochemical conversion back to Zn during charging.

The above examples show that it is possible to include organic additives in Zn–air batteries and that these could enhance the cyclability and energy efficiency of such batteries. To improve the simulative approach in this work, the modeling group will apply the developed routine[33] and, with the knowledge gained, screen for new possible organic additives.

Conclusions

The results obtained in this work show that careful selection of electrolyte additives is required when considering electrolyte and electrode material stability, as well as achievable electrochemical performance. Furthermore, modeling predictions of suitable additives must consider full-cell setups and half-cell optimization but may fail to detect severe degradation effects. It was shown that the reaction of potassium citrate with metal ions reduced electrochemical performance and cathode activity. This behavior may apply to most carboxylic acids because the reaction mechanism for most of these acids is similar. Both Ni and Ag showed corrosion effects after cycling. Although these were severe for the Ag-based electrode, the Ni-based electrode retained its morphology and only showed pitting corrosion on its particles. The observed corrosion was likely due to the oxidation reaction of the used metals, which reacted with the intermediate species of the Kolbe-like reaction of the potassium citrate.

Furthermore, the tribase citric acid used in this work showed a similar reduced ionic conductivity as was observed for the dibase carbonic acid. Moreover, the onset potential in both acids decreased from approximately 0.9 V vs RHE to 0.6 V vs RHE, resulting in lower discharge voltages.

In the final part of this work, the electrolyte stability during OER was examined. It was shown that above 1.7 V vs RHE, CO_2 evolved and, concurrently, no O_2 evolution was observed for the entire investigated potential range. Additional tests with pH monitoring showed that the CO_2 formation resulted from the decomposition of potassium citrate. Glycine showed stability up to 2 V vs RHE before starting to decompose.

Acknowledgments

This research was supported by funding the European Commission in the frame of Horizon2020 through the grant agreement 646186-ZAS. Furthermore, I want to special thank Werner Seybold for building the test cells, Fabian Bienen for conducting the gas chromatography experiment, and Dr. Simon Clark for the valuable input.

ORCID

Alexander Kube https://orcid.org/0000-0002-8042-326X
Norbert Wagner https://orcid.org/0000-0002-2596-8689

References

1. J. Fu, R. Liang, G. Liu, A. Yu, Z. Bai, L. Yang, and Z. Chen, *Adv. Mater.*, **31**, 1805230 (2019).
2. Y. Li and H. Dai, *Chem. Soc. Rev.*, **43**, 5257 (2014).
3. R. Othman, W. J. Basirun, A. H. Yahaya, and A. K. Arof, *J. Power Sources*, **103**, 34 (2001).
4. O. Haas, F. Holzer, K. Müller, and S. Müller, *Handbook of Fuel Cells* (Wiley, Online Library) 42, 903 (2010).
5. S.-M. Lee, Y.-J. Kim, S.-W. Eom, N.-S. Choi, K.-W. Kim, and S.-B. Cho, *J. Power Sources*, **227**, 177 (2013).
6. H. Yang, Y. Cao, X. Ai, and L. Xiao, *J. Power Sources*, **128**, 97 (2004).
7. S. J. Banik and R. Akolkar, *J. Electrochem. Soc.*, **160**, D519 (2013).
8. C. W. Lee, K. Sathiyanarayanan, S. W. Eom, H. S. Kim, and M. S. Yun, *J. Power Sources*, **159**, 1474 (2006).
9. K. Kim, Y.-H. Cho, S. W. Eom, H.-S. Kim, and J. H. Yeum, *Mater. Res. Bull.*, **45**, 262 (2010).
10. C. J. Lan, C. Y. Lee, and T. S. Chin, *Electrochim. Acta*, **52**, 5407 (2007).
11. D. Schröder, N. N. Sinai Borker, M. König, and U. Krewer, *J. Appl. Electrochem.*, **45**, 427 (2015).
12. Y. Sato, H. Niki, and T. Takamura, *J. Electrochem. Soc.*, **118**, 1269 (1971).
13. D. C. W. Kannangara and B. E. Conway, *J. Electrochem. Soc.*, **134**, 894 (1987).
14. J. Stamm, A. Varzi, A. Latz, and B. Horstmann, *J. Power Sources*, **360**, 136 (2017).
15. H.-W. Ko and H.-K. Juang, *J. Appl. Electrochem.*, **13**, 725 (1983).
16. J. Boniface, Q. Shi, Y. Q. Li, J. L. Cheung, O. V. Rattigan, P. Davidovits, D. R. Worsnop, J. T. Jayne, and C. E. Kolb, *The Journal of Physical Chemistry A*, **104**, 7502 (2000).
17. M. Hofmann and H. J. Schellnhuber, *Energy Environ. Sci.*, **3**, 1883 (2010).
18. J. Qiao, L. Xu, L. Ding, P. Shi, L. Zhang, R. Baker, and J. Zhang, *Int. J. Electrochem. Sci.*, **8**, 1189 (2013).
19. S. Hosseini, S. Masoudi Soltani, and Y.-Y. Li, *Chem. Eng. J.*, **408**, 127241 (2021).
20. P. Delahay, M. Pourbaix, and P. V. Rysselberghe, *J. Electrochem. Soc.*, **98**, 57 (1951).
21. J. J. Jurinak and D. W. Thorne, *Soil Sci. Soc. Am. J.*, **19**, 446 (1955).
22. S. Thomas, N. Birbilis, M. S. Venkatraman, and I. S. Cole, *Corrosion*, **68**, 015009-015001 (2012).
23. J. Fu, Z. P. Cano, M. G. Park, A. Yu, M. Fowler, and Z. Chen, *Adv. Mater.*, **29**, 1604685 (2017).
24. M. Gmytryk and J. Sedzimir, *Corros. Sci.*, **7**, 683 (1967).
25. N. Borchers, S. Clark, B. Horstmann, K. Jayasayee, M. Juel, and P. Stevens, *J. Power Sources*, **484**, 229309 (2021).
26. S. Clark, A. Latz, and B. Horstmann, *Chem Sus Chem*, **10**, 4735 (2017).
27. J. Jindra, J. Mrha, and M. Musilová, *J. Appl. Electrochem.*, **3**, 297 (1973).
28. F. W. Thomas Goh, Z. Liu, T. S. A. Hor, J. Zhang, X. Ge, Y. Zong, A. Yu, and W. Khoo, *J. Electrochem. Soc.*, **161**, A2080 (2014).
29. S. Clark, A. R. Mainar, E. Iruin, L. C. Colmenares, J. A. Blázquez, J. R. Tolchard, A. Latz, and B. Horstmann, *J. Mater. Chem. A*, **7**, 11387 (2019).
30. A. Sumboja, X. Ge, G. Zheng, F. W. T. Goh, T. S. A. Hor, Y. Zong, and Z. Liu, *J. Power Sources*, **332**, 330 (2016).
31. E. Iruin, A. R. Mainar, M. Enterría, N. Ortiz-Vitoriano, J. A. Blázquez, L. C. Colmenares, T. Rojo, S. Clark, and B. Horstmann, *Electrochim. Acta*, **320**, 134557 (2019).
32. S. Clark, A. R. Mainar, E. Iruin, L. C. Colmenares, J. A. Blázquez, J. R. Tolchard, Z. Jusys, and B. Horstmann, *Adv. Energy Mater.*, **10**, 1903470 (2020).
33. A. Apelblat and J. Barthel, *Z. Naturforsch. A*, **46**, 131 (1991).
34. E. S. Hamborg, W. P. M. Van Swaaij, and G. F. Versteeg, *J. Chem. Eng. Data*, **53**, 1141 (2008).
35. D. Wittmaier, N. Wagner, K. A. Friedrich, H. M. A. Amin, and H. Baltruschat, *J. Power Sources*, **265**, 299 (2014).
36. D. Wittmaier, S. Aisenbrey, N. Wagner, and K. A. Friedrich, *Electrochim. Acta*, **149**, 355 (2014).
37. M. Lyons and M. Brandon, *Int. J. Electrochem. Sci. International Journal*, **3**, 1386 (2008).
38. Y. Hoppilliard, F. Gilard, and G. Ohanessian, *Int. J. Mass spectrom.*, **206**, 45 (2001).
39. S. K. Das, A. Reis, and K. J. Berry, *J. Power Sources*, **193**, 691 (2009).
40. D. T. Chin and P. D. Howard, *J. Electrochem. Soc.*, **133**, 2447 (1986).
41. D. Strmcnik, K. Kodama, D. van der Vliet, J. Greeley, V. R. Stamenkovic, and N. M. Marković, *Nat. Chem.*, **1**, 466 (2009).
42. D. S. Kilin, O. V. Prezhdo, and Y. Xia, *Chem. Phys. Lett.*, **458**, 113 (2008).
43. I. A. Mudunkotuwa, T. Rupasinghe, C. M. Wu, and V. H. Grassian, *Langmuir*, **28**, 396 (2012).
44. A. K. Vijh and B. E. Conway, *Chem. Rev.*, **67**, 623 (1967).
45. N. Agmon, *Chem. Phys. Lett.*, **244**, 456 (1995).
46. H. Zhong, K. Fujii, Y. Nakano, and F. Jin, *The Journal of Physical Chemistry C*, **119**, 55 (2015).
47. R. D. Giles and J. A. Harrison, *J. Electroanal. Chem. Interfacial Electrochem.*, **27**, 161 (1970).
48. S. Hosseini, A. Abbasi, L.-O. Uginet, N. Haustraete, S. Praserthdam, T. Yonezawa, and S. Kheawhom, *Sci. Rep.*, **9**, 14958 (2019).
49. Y. Xiao, J. Shi, F. Zhao, Z. Zhang, and W. He, *J. Electrochem. Soc.*, **165**, A47 (2018).

Sustainable Chemistry & Engineering

pubs.acs.org/journal/ascecg

Research Article

Influence of Cycling onto Electrolyte Distribution Inside a Silver-Based Gas Diffusion Electrode for Zn-Air Batteries

Alexander Kube,* Dennis Kopljar, Norbert Wagner, and Kaspar Andreas Friedrich

Cite This: https://doi.org/10.1021/acssuschemeng.2c04542

Read Online

ACCESS | Metrics & More | Article Recommendations | Supporting Information

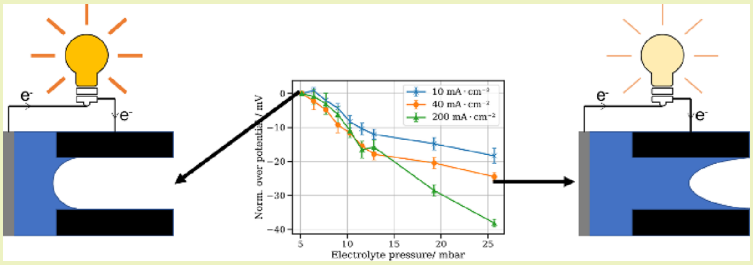

ABSTRACT: The understanding of the wetting behavior of gas diffusion electrodes (GDE) during operation is the key to developing gas diffusion electrodes with a stable triple-phase boundary and high electrochemical performance. In metal-air batteries, this is even more complex as the wide potential range during charge and discharge leads to several oxidation states with different molar volumes and wetting characteristics. In our work, we showed with a segmented cell the shift of current density to areas with less hydrostatic pressure for the oxygen reduction reaction and analyzed the hydrostatic pressure influence further with a cell enabling us to set the electrolyte pressure. We could also show the decrease of pore sizes and the influence of these smaller pores and higher wettability of the oxidized silver surface by using a pressure saturation setup. The knowledge of these findings offers the opportunity to design GDEs with lower tendency for flooding and therefore longer operation times.

KEYWORDS: *electrolyte distribution, GDE, wetting characteristics, Zn-air battery, liquid electrolyte distribution, charge transport*

INTRODUCTION

The increasing conversion of electricity production to renewable energies poses a challenge for grid stability due to their dependence on external factors such as sun, wind, and tides. To ensure continuous availability of electricity, base-load power plants or energy storage facilities are needed. Batteries are a suitable choice to cover short power peaks until suitable power plants can be ramped up. The state of the art for such energy storage facilities are Li-ion battery-based facilities like the 300 MW/1.2 GWh facility in Southern California and the 100 MW/129 MWh facility in Australia. Metal-air batteries, especially Zn-air batteries, are an attractive candidate for such storage facilities as they have high theoretical energy densities. That is because only one reactant is stored inside the battery whereas the other (oxygen) is provided from the atmosphere. Metal-air batteries are built of a metal anode, a separator, electrolyte, and the gas diffusion electrode (GDE). GDEs are hydrophobic porous structures allowing the electrolyte to penetrate the porous system but at the same time hindering the electrolyte from completely flooding the porous structure. Due to the partial flooding of the porous structure, there is a large interfacial region within the GDE, called the triple-phase boundary, where gas, electrolyte, and catalyst meet. The reaction takes place at this triple-phase boundary and defines the electrochemical performance. The knowledge and understanding about the behavior and distribution of the electrolyte inside the porous system is therefore crucial to developing electrodes with high electrochemical performance and high cycle life. Different approaches were taken to identify the penetration depth and reaction zone inside the GDE. As there is no direct measurement method, only indirect investigations were performed. Franzen et al. used a layered GDE for ORR with silver as active material and nickel as inactive material and could show that the electrolyte penetration is more than 75 μm into the GDE, which was the limit of the production technique used for this study.[1] Bienen et al. used a setup were they could alter the electrolyte pressure and film the backside of the GDE showing the droplet formation on the gas side due to electrowetting.[2] Both studies showed that the understanding and the control of the pore space and pore distribution is

Received: August 1, 2022
Revised: November 30, 2022

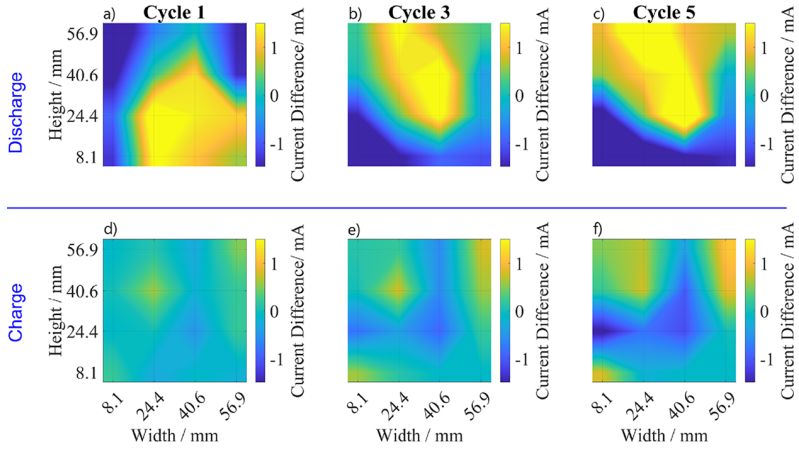

Figure 1. Normalized current distribution maps for the first five cycles. Upper row shows the distribution at the end of each discharge cycle (a–c), the lower row the current distribution at the end of each corresponding charge cycle (d–f).

essential for extended operation times and low degradation of such electrodes.

The focus of this work is based on the characteristics of the Zn-air battery. In comparison to previous studies where only the oxygen reduction reaction (ORR) during discharging was of interest in primary cells, recharging in secondary cells requires the optimization and study of the oxygen evolution reaction (OER) as well. Due to the wide potential range, the silver undergoes oxidation during charging and reduction during discharge. This is beneficial to provide high currents for short time periods as shown by Mainar et al.[3] However, different oxidation states of silver also show different wetting behavior and the molar volume of silver changes as well, altering the pore size distribution. Additionally, the electrolyte pressure inside the system varies as the zinc anode undergoes volume changes during charge and discharge. Both effects promote flooding of the porous structure resulting in reduced cycle life and electrochemical performance. To investigate the influence of the varying oxidation states and pore size distribution, we first identified parameters of interest and have built test cells enabling us to investigate these parameters. For this, we first used our segmented cell setup to visualize the influence of hydrostatic pressure in a vertical cell design. By using a three-electrode setup with the possibility to alter the hydrostatic pressure, we were able to investigate the influence of advancing electrolyte saturation on performance of the electrode. As mentioned above, the oxidized silver has a higher molar volume than silver resulting in a reduction of pore size. This influences transport of ions in the electrolyte, which depends on the tortuosity and porosity of the porous structure. Furthermore, it also influences the gas permeability and therefore gas transport. Both effects could be quantified and show the strong dependence of oxidation states onto the transport phenomena. By using a pressure saturation measurement, we were also able to show the strong dependence of the wetting behavior onto the oxidation states.

EXPERIMENTAL SECTION

Electrochemical Tests. Electrodes were tested in a homemade half-cell configuration as shown in Figure S1.

Silver oxide-based GDEs (31% porosity, 475 μm thickness with nickel mesh, supplier: Covestro) were cut out to 2 × 2 cm pieces, and a GDL Sigracet 29 BC (80% porosity, 5 wt % PTFE, 235 μm thickness, with MPL, depicted as green part in Figure S1) was mounted between the gas compartment and the electrode (red part in Figure 1). The cell, with its 1 L electrolyte container filled with 32 wt % KOH, was placed in a thermally controlled water bath, set to 25 °C, and connected to a Zahner Zennium potentiostat. As a reference electrode, a Gaskatel reversible hydrogen electrode (RHE) was used. In this electrode, the platinum is in contact with the bulk electrolyte of the cell and therefore no additional internal electrolyte is needed for this system. The potential is determined using the reaction of hydrogen and platinum in the electrolyte of interest. For this, a hydrogen cartridge is connected via a drilled hole to the platinum mesh. As feed gas, pure O_2 was used.

Prior to all electrochemical tests, the electrode potentials were scanned by cyclic voltammetry (CV) between 300 mV vs RHE and 1800 mV vs RHE with a scan rate of 1 mV•s^{-1} for 20 cycles.

For standard CV, the electrolyte height was set to 4 cm above the middle of the GDE. To investigate the influence of the hydrostatic pressure, the electrolyte was set to 4 cm and after each measurement cycle increased by 1 cm until 10 cm. 15 and 20 cm were measured additionally. Due to the density of 32 wt % KOH of 1.3, the measured pressure range was 5.2 mbar to 26 mbar.

Test cycles for hydrostatic influence measurements consisted of 1 h chrono voltammetry measurements at −10, −40, and −200 mA•cm^{-2}.

Current Density Distribution Maps. Current density distribution maps were obtained using our previously described setup with the transimpedance amplifier (TIV) setup.[4] The basis for all measurements is a current to potential conversion, as potential can be measured more accurate than current. The TIV setup was connected to the PAD4 (Parallel Analog-Digital 4) cards mounted in a Zahner IM6. As reference and counter electrode, a 250 μm-thick Zn foil was used, and as cathode, the silver electrode with a backing of a self-prepared GDL was used. For this, 80 wt % Timcal Timrex T150 was physically mixed with 20 wt % PTFE (TF9207Z, 3 M Dyneon) in a knife mill for 30 s. The obtained powder mixture was filled into a frame, calendared at 30 kg, and heat treated for 1 h at 340 °C.[4]

The charge and discharge cycles were done with a total current of 120 mA each for 8 h.

Effective Diffusion Constant. Electrodes were placed inside a vacuum flask together with deionized water. A vacuum was applied to the vacuum flask until no gas bubbles were visible at the electrode. This was done to ensure a complete filling of the porous system. The electrode was then mounted in the test cell (Figure S2), and one compartment was immediately filled with 1.2 × 10^{-2} M KOH. Each chamber can hold up to 40 mL of test liquid.

The cell was placed inside a water bath with a constant temperature of 25 °C, and the stirring in the filled compartment was started. The resistance was measured between two nickel rods (diameter of 3 mm, length inside the cell 2 cm; depicted in gray in Figure S2) until a stable value was achieved. For this, a current of 200 μA was applied

https://doi.org/10.1021/acssuschemeng.2c04542
ACS Sustainable Chem. Eng. XXXX, XXX, XXX−XXX

between at a phase angle of zero, to assure that only the ohmic resistance is measured. The stable resistance was used as indicator for an even temperature distribution inside the cell. Chamber two was filled at this point with 40 mL 32 wt % KOH, and the stirrer in this chamber was started as well. The data recording was stopped when the measured resistance has fallen to 100 Ω. In Figure S3a, one measurement is exemplarily shown with the resistance in red. The concentration can be calculated using the calibration curve depicted in Figure S3b. To obtain the effective diffusion constant D the first Fickian law with the concentration C and the diffusion flux J was used (eq 1).

(1)

Gas Permeability. The sample (red area in Figure S4) was mounted into the test cell, and the pressure vent on top of it was opened until the anemometer (Testo 405) showed first values. Nitrogen was used as test gas. One pressure transducer (BD Sensor, 1 bar) was used to measure the absolute pressure above the sample, and a second pressure transducer (BD Sensor, 1 Bar) was used to measure the difference in pressure between the part above and below the sample. The test area was 3.14 cm^{-2} (2 cm diameter).

The permeability k was calculated using Darcy's law for incompressible fluids:[5]

(2)

where L describes the sample thickness and A its area, Q the gas flow rate, P_1 the absolute pressure above the sample, and P_2 the absolute pressure below the sample. ΔP describes the pressure difference between above and below the sample.

Pressure Saturation Curves. Pressure saturation curves were recorded using the cell described in our previous publications (see Figure S5).[6,7] Deionized water was degassed and filled in the liquid vessel on top of the balance and the pipe system. All water-containing compartments were purged with degassed water until no gas bubbles were left. The hydrophilic membrane was placed on top of the water distributer and fixed with the corresponding cell part (further descriptions are given in ref 7). An underpressure of −300 mbar was applied on top of the liquid vessel inside the balance, and after a short waiting period, the electrode mounted inside a PTFE frame was placed on top of the hydrophilic membrane together with a hydrophobic membrane. The upper part of the cell was mounted and the electrode/hydrophobic membrane stack fixed with it. After the gas distribution unit was mounted, the cell was sealed with the syringe and pressure transducer holder.

The gas pressure inside the cell was set to 250 mbar, and the vacuum at the liquid vessel was removed prior to test start, as described in more detail in our previous work.[7]

SEM pictures were taken with a Zeiss Ultra Plus by using electrodes glued with conductive adhesive tapes on the sample holder. Electrode cuts where obtained using a JEOL IB-19520CCP Cryo Cross Section Polisher with an ion accelerating voltage of 8 kV (Figure 6.)

RESULT AND DISCUSSION

Current Distribution Changes during Cycling. In our previous work, we showed that during one discharge cycle non-uniform current distribution led to a non-uniform dissolution of the anode.[4] We assumed that this is due to the hydrostatic pressure of the electrolyte to further penetrate the porous media near the ground level and less at the top of the cell. To further evaluate hydrostatic pressure and its influence on the current distribution, Figure 1 shows the changes in the current density over the first five cycles. For better visualization of changes, the current distributions were normalized by subtracting the first current distribution of the according reaction after 8 s (depicted in Figure S6).

The upper row shows the current distribution at the end of the corresponding discharge cycle, the lower the same for the end of the corresponding charge cycles. While a clear shift of the current density from the lower to the upper region can be observed for the discharge cycles, the charge cycles do not show this clear trend. While during charge oxygen evolution takes place and all surface covered by the electrolyte is active, known as the two-phase boundary, for discharge the reaction takes place at the so-called triple phase boundary where electrolyte, catalyst, and gas are present. The observed shift might be because of inhomogeneous flooding of the GDE due to hydrostatic pressure, accompanied by several other mechanisms, which affect the saturation of the GDE. During operation, the applied potential results in an augmentation of the wettability of the GDE materials, denominated electrowetting, and therefore leads to a gradual flooding of the porous network.[8] Beside the electrowetting, the flooding of the porous network is governed by capillary force and wettability of the materials. For an idealized porous network consisting solely of pipe formed pores, capillary force P_c can be calculated by the Young−Laplace eq 3:

(3)

with the solid−liquid surface energy σ, the pore diameter d, and the contact angle θ. The capillary pressure is defined as the difference between the liquid and gas phases at equilibrium.[7] As there is a distribution of different pore sizes and throats in real electrodes, not one but several capillary pressures are present in the system leading to inhomogeneous flooding; for example, smaller, hydrophilic pores flood more easily than larger, hydrophobic pores. This might lead to a separation of some areas from gas supply, reducing the active surface. The same effect can occur if GDE materials are not homogeneously mixed during production. As a GDL consists normally of a catalyst, a conductive medium, and a hydrophobic binder (normally PTFE) with different wettability properties, non-homogeneous distribution leads to areas that are more easily flooded than others.

Due to the large potential range to which the cathode materials are exposed, oxidation and reduction reactions occur, which can change the wettability of the materials due to the different oxidation states.

Carbonate formation is not likely the reason for the observed shift, as the measurement time was too small for precipitation and blocking of pores and precipitation should have taken place homogeneously over the whole GDE area. Additionally, both ORR and OER should be affected by deactivation of active centers by carbonate formation.

The structural complexity of the GDL hinders the distinction of processes like flooding, gas entrapment, or product accumulation inside the GDE. Therefore, the influence of some of these parameters requires special setups.

Influence of Hydrostatic Pressure onto Electrochemical Performance. As the electrolyte pressure inside the cell increases during discharge due to anode volume increase and is not accommodated for by cell design, a flooding of the cathode will occur. This was mimicked by the use of the hydrostatic cell (depicted in Figure S1). Figure 2 shows the normalized overpotential vs the hydrostatic pressure for three applied current densities. For normalization, the measured

https://doi.org/10.1021/acssuschemeng.2c04542
ACS Sustainable Chem. Eng. XXXX, XXX, XXX−XXX

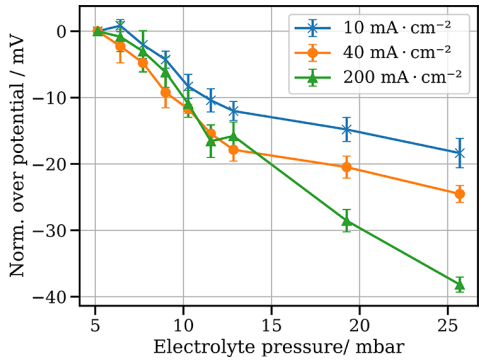

Figure 2. Normalized overpotential vs hydrostatic pressure at 25 °C with pure O_2 and 32 wt % KOH in the cell shown in Figure S1.

value for 5.1 mbar was subtracted from all values. Positive values mean a decrease in overpotential for the applied current density; negative values mean an increase of overpotentials. For all three applied current densities, an increase of overpotential can be observed, with the highest increase for 200 $mAcm^{-2}$. Two slopes can be identified for all three current densities: the first one with a faster decline until 13 mbar and a second with a slower decline until the end of the measurement.

Due to the penetration of electrolyte, gas channels are flooded, blocking gas from reaching into the depth of the porous system. This reduces the active surface resulting in higher overpotentials. Additionally, mass transport in the liquid phase is slower, which results in higher performance if the electrolyte front is close to the bulk electrolyte.[9] This was also shown by Franzen et al. with their investigations on the influence of the PTFE content in silver electrodes onto the electrochemical performance. They showed that with low PTFE loadings, mass transport issues related to higher saturation of the pores inside the GDE can be observed.[10] As it is known from literature, the electrolyte does not penetrate as an electrolyte front but instead small fingering occurs.[11,12] Additionally, bigger pores are filled first, as can be concluded by eq 1. Fingering and filling of big pores could lead for one to the described blockage of gas to reach into the depths of the electrode but could also result in filling pores through the whole thickness of the electrode, resulting in a flooding of the space between the electrode and the backing GDL. This would block the gas transport into the electrode depth even more. Additionally, a shift of the reaction zone from the GDE to the GDE could occur. For the tested case, the electrolyte penetration was less severe as this would result in much larger overpotentials due to the diffusion through the thick electrolyte film. Therefore, only partial flooding of the area between the GDE and the GDL can be assumed as well as the fingering of electrolyte.

An increasing saturation of the GDE porous structure leads to a decrease of permeability, as described by Rosén et al., and increases the diffusion path length.[13]

To further analyze the influence of the increasing saturation, EIS was performed after each current density measurement (see Figure 3a for 200 mA/cm^2). All of the measured semicircles show the characteristics of the electric transport, which is dominated by the ionic contribution.[14] As equivalent circuit, a transmission line model with an RQ-element describing the charge transfer and double-layer capacity was used together with a resistor to describe the ohmic resistance. In Figure 3a, the Nyquist plot of the measured spectra is depicted. It can be seen that for an increase of electrolyte pressure, the lower-frequency part increases as well as the ohmic resistance. This can be seen in Figure 3b as well where the calculated ohmic resistance and the resistance of the porous system are depicted. Both show the expected behavior

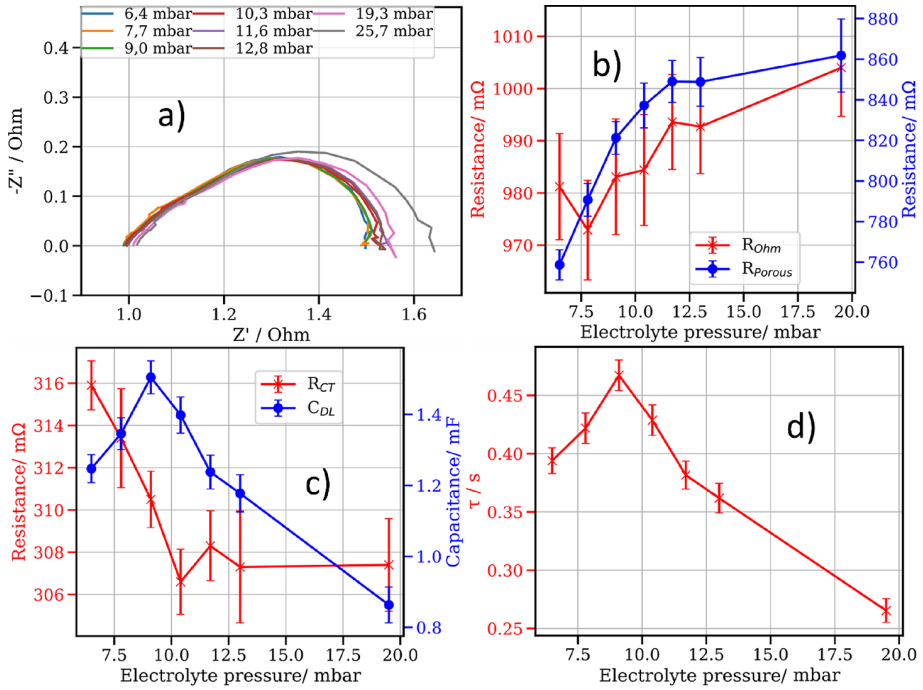

Figure 3. (a) Nyquist plot at the different electrolyte pressures; (b) the ohmic resistance (red) and the resistance of the porous system (blue). (c) Charge transfer resistance (red) and the corresponding double layer capacitance (blue). (d) Calculated time constant of the charge transfer resistance and double-layer capacity.

https://doi.org/10.1021/acssuschemeng.2c04542
ACS Sustainable Chem. Eng. XXXX, XXX, XXX−XXX

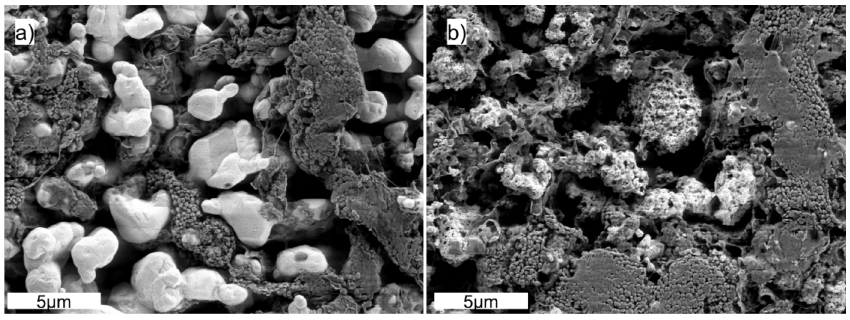

Figure 4. SEM pictures of a pristine silver electrode (a)) and the used electrode (b)).

of an increase due to the longer diffusion paths of ions inside the porous system. At around 11.5 mbar, the increase of ionic transport levels off, meaning that the filling of the electrode is almost finished in the applied pressure range.

Figure 3c shows the calculated values of the charge transfer resistance and the double-layer capacitance. While the charge transfer resistance decreases indicating an increase of active surface, the double-layer capacitance shows a decrease. This is unexpected, as with increasing electrolyte pressure, the saturation of the porous system increases and therefore an increase of the double-layer capacitance should appear. Figure 3d shows the time constant ($\tau = C \times R$), which should show a constant behavior if the active surface has the same properties. This is because the time constant is independent of the surface area. The observed change of τ could be due to several reasons. As the capacitance of the double layer is potentially dependent, the observed changes in Figure 2 could add to this change in the time constant, but below 9 mbar, they do not correlate. Additionally, the observed changes in potential with increasing electrolyte pressure are rather small and therefore only small contributions can be expected. Additionally, the ionic conductivity of the electrolyte and temperature do not change and therefore can be excluded as reasons for the observed trends.

During the activation process with 20 CV cycles in the range from 0.3 to 1.8 V vs RHE, the electrode was reduced and oxidized several times. The high mobility of silver ions in the electrode leads to morphology changes on the particle surface (see Figure 4) and even changes in the pore size distribution.[15] Figure 4 shows SEM pictures of an unused (a) and a used (b) electrode. The bigger particles depicted in light gray are silver particles, why the darker agglomerates are PTFE. The surface roughening of the silver particles can be seen clearly in these SEM pictures.

As the morphology and pore size changes occur only in wetted regions, the increase of electrolyte pressure leads to wetting of new surfaces inside the porous system without surface morphology changes and different pore sizes. As the current distribution inside the silver GDE is assumed to be homogeneous, the different surface morphologies can be seen as parallel circuit and therefore the capacity should increase ($C_{total} = C_1 + C_2$). As is described by the deLevie model (eq 4) for the impedance in a porous system with the length of each pore l, the electrolyte resistivity ρ, the pore radius r, and the interfacial impedance per surface unit Z_{eq},[16] the change in pore size could influence the capacity and might be a reason for the observed decay of the double-layer capacity.

(4)

Another explanation could be a combination of the double-layer capacities of the silver GDE and the GDL. As described above, the electrolyte infiltrates the porous system in a fingering way. This could lead to an early wetting of the GDL and the space between both. In this case, the current inside the system is divided to the GDL and GDE, and therefore, the capacities are connected in series ($1/C_{total} = 1/C_1 + 1/C_2$).

While the double-layer capacity measures the wetted area, it does not include the time-dependent progressing wetting inside an already wetted area as was observed by Bienen et al.[17] They observed a time-dependent wetting front with post-mortem analysis and found that the penetration followed a square root-like function, which did not follow the time dependence of the double-layer capacity from impedance data. We have to conclude that the double-layer capacity does not correlate with electrolyte intrusion and therefore a better descriptor may be R_{porous}, as it exhibits the expected behavior of electrolyte penetration into the porous system (Figure 3b blue curve). It can be seen that until around 11 mbar, a steep rise can be observed, and above 11 mbar the increase in resistance is very low and shows a saturation behavior. This might be due to changed wetting properties, e.g., if the electrolyte has reached the GDL, which is highly hydrophobic.

To investigate the influence of the GDE, the same test setup as in Figure 2 was used, but without a GDL as support between gas compartment and GDE (Figure S7). This test shows that the electrolyte penetrates the porous system even for low electrolyte pressures limiting the performance. This indicates that in our test case with a GDL, the electrolyte is held back to some extent favoring gas transport to the active centers. Additionally, it shows that during the impedance measurement, the wetted GDL takes part in the reaction giving another hint that the capacities are connected in series and therefore might be the reason for the observed decreasing double-layer capacitance.

Another possible explanation could be a redistribution inside the porous system. As shown below, during the activation process the system changes between wider pores with lower wettability and smaller pores with higher wettability. During the test with varying hydrostatic pressures, the system is held in the state with wider pores and lower wettability. As the penetration into the porous system follows favored paths, these could lead to inhomogeneous pressure distributions inside the porous system and that can even lead to de-wetting of internal regions. This will be subject of a follow up study for a more detailed view.

https://doi.org/10.1021/acssuschemeng.2c04542
ACS Sustainable Chem. Eng. XXXX, XXX, XXX−XXX

Beside the observed lower electrochemical performance, the flooding of electrolyte leads to other negative effects, which are not easily studied. A formerly wetted region can be freed by higher gas pressures or other methods, but carbonate salts as well as KOH salts left after a flooding event aid the next electrolyte intrusion as they are highly hygroscopic.[18]

Influence of Oxidation and Reduction Processes onto Pore Size Distribution and Transport. Figure 5 shows a CV of a silver GDE, and the different oxidation states are marked by numbers. The reaction at position 1 can be associated with the dissolution of Ag and the formation of $[Ag(OH)_2]^-$:[19−21]

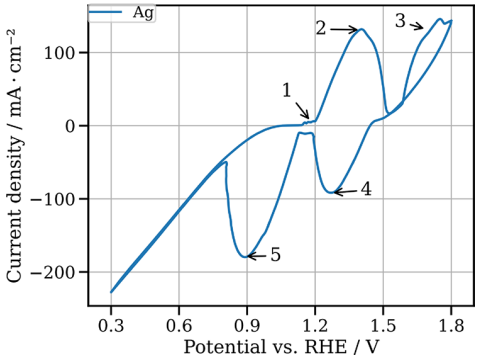

Figure 5. Cyclic voltammogram of a silver electrode at 25 °C with pure oxygen and 32 wt % KOH with markings of the different oxidation states.

(5)

(6)

As dissolved $[Ag(OH)_2]^-$ can migrate into the bulk electrolyte, which in our case is 1 L KOH, solubility limits do not apply and therefore the dissolution of AG to $[Ag(OH)_2]^-$ does not show a clear peak but instead a voltage-dependent current flow.

The broad peak at point 2 consists of two peaks where silver is oxidized to Ag_2O. One inner hydrous Ag_2O layer and a more compact outer Ag_2O layer is formed:[21]

(7)

The transition from metallic silver (V_m = 1.03E-05 m^3/mol) to Ag_2O (V_m = 3.25E-05 m^3/mol) is accompanied by an increase of the molar volume by a factor of around 3.

The peak at point 3 can be assigned to the formation of a mixed oxide consisting of Ag_2O and Ag_2O_3.[22,23]

(8)

Wittmaier et al. investigated the stability of this mixed oxide and found that Ag_2O_3 is not stable and decays back to Ag_2O.[22]

If the potential is further increased, no further oxidation can be observed and the OER starts. If the potential decreases from the oxidized states, the reduction from the mixed oxide from eq 8 is reduced to Ag_2O at point 4 and is further reduced to metallic silver at point 5, after which only ORR takes place.

The above-described increase in molar volume leads to a decrease of pore sizes, as depicted in Figure 6. The left figure shows a cut of an electrode in the reduced state while the right figure shows the electrode in the oxidized state. As the cutting process included a lot of heat, the PTFE was evaporated in the process and is therefore not visible anymore.

This increase in volume reduces the pore sizes and therefore influences transport parameters. To further understand the gas permeability and the effective diffusion constant for three different electrodes for the reduced and oxidized states of silver electrodes that were measured, see Figure S8. For the untreated oxidized electrode, the averaged permeability value is 2.80 ± 0.10 mD, and for the reduced electrode, the averaged permeability value is 11.74 ± 0.07 mD. Due to the smaller molar volume and the resulting larger average pore distribution, the reduced electrode shows a permeability that is five times higher. The same behavior can be observed for the effective diffusion constant with $3.36 \times 10^{-6} \pm 0.22 \times 10^{-7}$ m^2 s^{-1} for the oxidized electrode and $3.29 \times 10^{-5} \pm 0.38 \times 10^{-6}$ m^2 s^{-1}, where the reduced state shows an around one order of magnitude higher effective diffusion constant. While both show a decrease for the oxidized electrode, these values are only representative of non-wetted GDEs. Under operation, the GDE is partially wetted with a blockage of a considerable part of the porous system leading to reduced permeability.

Wetting Behavior of Silver during Cycling. As explained above, a GDE consists of a mixture of materials with different wettability, resulting in a mixed wettability. Inside the porous network, this results in pores with higher wettability for smaller pore size diameters or lower PTFE contents as well as pores with lower wettability for larger pores or regions with higher PTFE content. Due to the very large potential range used during charging and discharging, different oxidation states of the individual materials occur during operation of the electrodes. In the case of the electrode used in this work, only silver changes its oxidation states.

Figure 7a shows the pressure saturation curve for the first filling of the oxidized and electrochemically reduced electrode. Starting with a capillary pressure of −30 mbar, a penetration of water into the pore space can be observed for both electrodes.

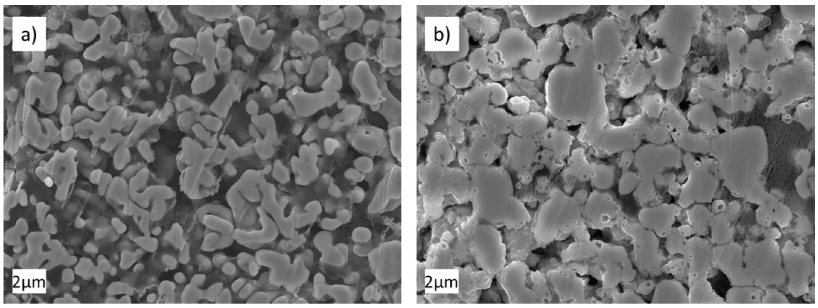

Figure 6. SEM pictures of electrodes cut with an ion beam. (a) Metallic silver; (b) the oxidized state.

https://doi.org/10.1021/acssuschemeng.2c04542
ACS Sustainable Chem. Eng. XXXX, XXX, XXX−XXX

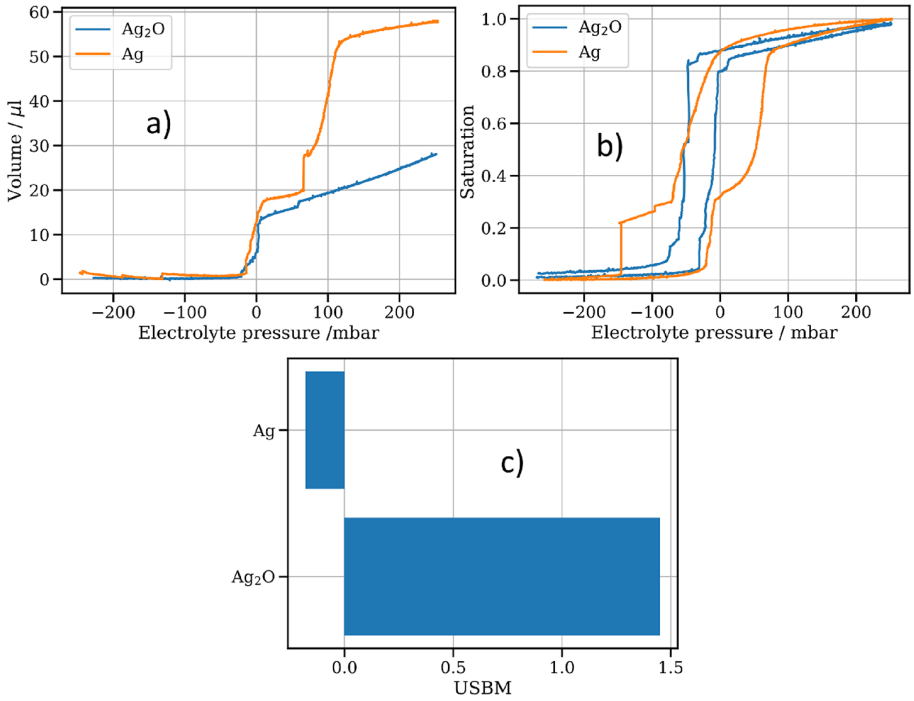

Figure 7. Pressure saturation curves for a metallic silver and a oxidized electrode. (a) The first imbibition for both electrodes; (b) the fifth cycle; (c) the USBM values calculated from (b).

For the oxidized electrode, the degree of saturation increases much more slowly than for the reduced electrode up to a capillary pressure of around 0 mbar. When changing to positive capillary pressures, the oxidized electrode shows a sharp increase in the degree of saturation up to about 12 μL. Consequently, the porous structure is steadily filled with further increasing pressure in a linear regime until 26 μL of water has penetrated the pore system and a capillary pressure of 250 mbar is reached. The reduced electrode exhibits behavior similar to the oxidized electrode up to a saturation level of 20 μL (about 65 mbar). With further increase of the capillary pressure, the volume increase increases sharply up to a capillary pressure of 115 mbar. Thereafter, the volume increase flattens out and reaches a volume of 58 μL at 250 mbar. According to the work of Danner et al., the porosity of the oxidized electrode that was also used in this work is 30.7%.[24] For another electrode that was produced using the same production technique, they further evaluated the change of porosity that takes place during reduction of the silver oxide. To approximate the porosity of the reduced electrode in this study, we herein assume a similar volume change as in the work from Danner et al. Accordingly, the porosity is around 38.3%. This corresponds to a water volume for the electrodes tested here of approximately 43.8 μL for the oxidized electrode and 54.5 μL for the reduced electrode. The amount of water infiltrated into the reduced electrode in the first cycle corresponds very well to the theoretical value here; for the oxidized electrode, a smaller infiltrated volume by a factor of 1.7 is shown. As the oxidized electrode has lower porosity, the PTFE is accumulated in this smaller pore space. This is equivalent to a higher PTFE loading and therefore lower wettability. The investigation of the PTFE distribution was not done by Danner et al. as the porosity determination was based on FIB-SEM sections. Here, the PTFE present in the pore space is evaporated during image acquisition. In the latter reconstruction of the 3D structure, this can therefore no longer be taken into account and might result in higher porosities than are actually present. The changed PTFE content also influences the percolation paths and might lead to an early formation of a liquid film between the rough electrode surface and the hydrophobic membrane even at very low filling levels, which reduces further filling of the pore space or increases the necessary pressure for further filling.

The hydrophilic behavior of the electrochemically reduced electrode may have been influenced by the reduction of the silver, since it can be assumed that not all the electrolytes could be removed from the electrode. The salt residues remaining in the pore space as a result are strongly hydrophilic and reduce the pressure required for filling. The behavior of the PTFE during the reduction of the silver oxide is another unknown factor. As surface transformations occur during the reduction process, detachment of PTFE fibrils may occur, which may also reduce hydrophobicity.

As shown in our previous publication with GDL39 BC as sample, there is always a difference between the first imbibition cycle and following cycles and was also shown by other groups for different samples.[25−28] After about three cycles, a stable cycling behavior can be observed. Cycles showing this stable cycling behavior are called reproducible region in the following. Both the first injection and the reproducible cycle range provide important information, but for an electrode in operation, the reproducible cycle range is more informative.

Figure 7b shows the pressure saturation curves for the silver electrode in the oxidized (Ag_2O) as well as reduced (Ag) state in the reproducible range. For pressure ranges with negative values, the imbibition takes place without acquiring a working force while for regions with positive values, work has to be performed to further penetrate the porous system with electrolyte during imbibition. The opposite applies during withdrawal.

https://doi.org/10.1021/acssuschemeng.2c04542
ACS Sustainable Chem. Eng. XXXX, XXX, XXX−XXX

The oxidized electrode shows negative capillary pressures up to a saturation level of 80%, equivalent to a hydrophilic pore space. The total injected volume for the oxidized electrode is 28.9 μL, and 57.3 μL for the reduced electrode. As explained for Figure 7a, the total volume of the oxidized electrode is not filled with water here. This might be an effect of mixed wettability as explained above resulting in pore space, which is filled more easily than other surrounding pores with lower wettability and therefore trapping the gas inside this space.

It is known from literature that metal oxides can exhibit hydrophilic behavior.[29−31] As shown in Figure 7, Ag_2O exhibits a strongly hydrophilic behavior dominating the hydrophobic binder (PTFE) in the filled region. Here, a water film is probably formed on the Ag_2O surface during the first filling, which lowers the capillary pressure required in subsequent cycles for filling. This water film may also result from very low contact angles on metal oxides.

In comparison, the reduced electrode shows clearly positive capillary pressures during the filling process from a saturation level above 30%. Below this degree of saturation, a negative capillary pressure can be observed during filling, which is comparable to the Ag_2O electrode. This indicates that at least parts of the surface could not be completely reduced. This may be caused by the electrolyte remaining in the pores after electrochemical reduction. Due to the equilibrium reaction of the silver in contact with the electrolyte, silver oxide can form again but only along the moistened paths in the partially flooded electrode. These paths, which are hydrophilic due to the surface silver oxide, are first filled during the filling process, resulting in the region of negative capillary pressures up to a saturation level of 30%. Subsequently, the pore space of pure silver is filled, resulting in the region of positive capillary pressures. According to the literature, silver shows a contact angle of 95° with increasing wetting and is thus slightly hydrophobic.[32] Thus, the high capillary pressures observed are likely due to a mean pore radius of 210 μm as well as the PTFE in combination with the silver. On the return path, the silver electrode shows negative capillary pressures; for the decreasing wetting, a contact angle of 37° is reported for silver surfaces,[32] which is strongly hydrophilic and contributes to the hysteresis in addition to the influence of the pore necks. When the degree of saturation is reduced below 30%, the capillary pressure decreases to much more negative values. In this case, the paths covered with silver oxide are emptied. Since pore passages not continuously covered with silver oxide up to the hydrophilic membrane are also emptied in this process, much lower capillary pressures are observed than with pure Ag_2O. When a capillary pressure of −150 mbar is reached, a sudden emptying occurs.

Figure 7c shows the US Bureau of Mines (USBM) index values calculated from Figure 7b. For the area below the pressure, saturation curves above (A_1) and below (A_2) 0 mbar are calculated and the USBM index calculated as shown in eq 9:[33]

(9)

Positive values represent a hydrophilic material, and negative values represent a hydrophobic material. The Ag_2O electrode shows a strongly hydrophilic character with a value of 1.45, while the reduced silver electrode shows a slightly hydrophobic character with a value of −0.18. Due to the clear expression of the wetting properties of the materials in the USBM index, a good applicability of this method for the electrodes used here can be assumed.

From the measurements shown, it can be concluded that the decreasing pore space during silver oxidation, which presses the electrolyte inside the porous system, and the formation of hydrophilic surfaces of the silver oxide allow the electrode to be flooded easily during charging of the battery. Since during discharge the reaction is reversed, the electrolyte might be pushed back with the use of gas pressure allowing for increased cycle life. If the cathode flooding effects are not accommodated, the cycle life of both electrodes could be shortened as the anode dries out while the cathode gets flooded.

CONCLUSION

In this study, the influence of the different silver oxidation states during charge and discharge onto the wetting and transport characteristics were investigated. It was shown that in a vertical cell, current distribution shifts to the upper half of the cell during cycling. While during discharge metallic silver is present with a hydrophobic characteristic and bigger pores, during charging, the pore size gets smaller due to the higher molar volume of the silver oxide, which shows a hydrophilic behavior. This aids to the flooding of the electrode. In the vertical cell, the hydrostatic pressure leads to heterogeneous flooding with higher electrolyte saturation in the lower part of the porous system and lower saturation levels in the higher part. This results in the observed shift of higher currents to the upper parts of the cell and a current decrease in the lower parts. As during charge no gas supply is necessary, the flooding does not result in a decrease of currents or shift in current density. However, the resulting smaller pore sizes might be responsible for limiting currents as the evolved gas is not effectively removed. As this effect is independent from electrolyte saturation but is evenly distributed over the whole electrode area, it is not visible in the current distribution map. Another effect of the different pore sizes are the one-magnitude-lower gas permeability and the effective diffusion coefficient for the silver oxide compared to the silver electrode.

ASSOCIATED CONTENT

Supporting Information

The Supporting Information is available free of charge at https://pubs.acs.org/doi/10.1021/acssuschemeng.2c04542.

Schematic illustration of experimental cells used, current distribution maps used for normalization, measurement data of transport parameters, and measurement data of hydrostatic pressure measurement without backing GDL (PDF)

AUTHOR INFORMATION

Corresponding Author

Alexander Kube − *German Aerospace Center, 70569 Stuttgart, Germany;* orcid.org/0000-0002-8042-326X; Email: alexander.kube@dlr.de

Authors

Dennis Kopljar − *German Aerospace Center, 70569 Stuttgart, Germany;* orcid.org/0000-0002-2228-2016

Norbert Wagner − *German Aerospace Center, 70569 Stuttgart, Germany*

https://doi.org/10.1021/acssuschemeng.2c04542
ACS Sustainable Chem. Eng. XXXX, XXX, XXX−XXX

Kaspar Andreas Friedrich − *German Aerospace Center, 70569 Stuttgart, Germany; Institute of Building Energetics, Thermal Engineering and Energy Storage (IGTE), University of Stuttgart, 70569 Stuttgart, Germany;* orcid.org/0000-0002-2968-5029

Complete contact information is available at: https://pubs.acs.org/10.1021/acssuschemeng.2c04542

Notes

The authors declare no competing financial interest.

■ ACKNOWLEDGMENTS

This research was supported by funding from the European Commission in the frame of Horizon2020 through the grant agreement 646186-ZAS. Furthermore, the authors want to specially thank Werner Seybold for building the test cells and the fruitful discussions.

■ REFERENCES

(1) Franzen, D.; Krause, C.; Turek, T. Experimental and Model-Based Analysis of Electrolyte Intrusion Depth in Silver-Based Gas Diffusion Electrodes. *ChemElectroChem* **2021**, *8*, 2186−2192.

(2) Bienen, F.; Paulisch, M. C.; Mager, T.; Osiewacz, J.; Nazari, M.; Osenberg, M.; Ellendorff, B.; Turek, T.; Nieken, U.; Manke, I.; Friedrich, K. A. Investigating the electrowetting of silver-based gas-diffusion electrodes during oxygen reduction reaction with electrochemical and optical methods. *Electrochem. Sci. Adv.* **2022**, *n/a*, No. e2100158.

(3) Mainar, A. R.; Iruin, E.; Blázquez, J. A. High performance secondary zinc-air/silver hybrid battery. *J. Energy Storage* **2021**, *33*, No. 102103.

(4) Kube, A.; Meyer, J.; Kopljar, D.; Wagner, N.; Friedrich, K. A. A Segmented Cell Measuring Technique for Current Distribution Measurements in Batteries, Exemplified by the Operando Investigation of a Zn-Air Battery. *J. Electrochem. Soc.* **2021**, *168*, 120530.

(5) Celzard, A.; Collas, F.; Marêché, J. F.; Furdin, G.; Rey, I. Porous electrodes-based double-layer supercapacitors: pore structure versus series resistance. *J. Power Sources* **2002**, *108*, 153−162.

(6) Sarkezi-Selsky, P.; Schmies, H.; Kube, A.; Latz, A.; Jahnke, T. Lattice Boltzmann simulation of liquid water transport in gas diffusion layers of proton exchange membrane fuel cells: Parametric studies on capillary hysteresis. *J. Power Sources* **2022**, *535*, No. 231381.

(7) Kube, A.; Bienen, F.; Wagner, N.; Friedrich, K. A. Wetting Behavior of Aprotic Li−Air Battery Electrolytes. *Adv. Mater. Interfaces* **2022**, *9*, 2101569.

(8) Lees, E. W.; Mowbray, B. A. W.; Parlane, F. G. L.; Berlinguette, C. P. Gas diffusion electrodes and membranes for CO2 reduction electrolysers. *Nat. Rev. Mater.* **2022**, *7*, 55−64.

(9) Röhe, M.; Franzen, D.; Kubannek, F.; Ellendorff, B.; Turek, T.; Krewer, U. Revealing the degree and impact of inhomogeneous electrolyte distributions on silver based gas diffusion electrodes. *Electrochim. Acta* **2021**, *389*, No. 138693.

(10) Franzen, D.; Ellendorff, B.; Paulisch, M. C.; Hilger, A.; Osenberg, M.; Manke, I.; Turek, T. Influence of binder content in silver-based gas diffusion electrodes on pore system and electrochemical performance. *J. Appl. Electrochem.* **2019**, *49*, 705−713.

(11) Sinha, P. K.; Wang, C.-Y. Pore-network modeling of liquid water transport in gas diffusion layer of a polymer electrolyte fuel cell. *Electrochim. Acta* **2007**, *52*, 7936−7945.

(12) Leclaire, S.; Parmigiani, A.; Malaspinas, O.; Chopard, B.; Latt, J. Generalized three-dimensional lattice Boltzmann color-gradient method for immiscible two-phase pore-scale imbibition and drainage in porous media. *Phys. Rev. E* **2017**, *95*, 033306.

(13) Rosén, T.; Eller, J.; Kang, J.; Prasianakis, N. I.; Mantzaras, J.; Buchi, F. N. Saturation Dependent Effective Transport Properties of PEFC Gas Diffusion Layers. *J. Electrochem. Soc.* **2012**, *159*, F536−F544.

(14) Kube, A.; Strunz, W.; Wagner, N.; Andreas Friedrich, K. Evaluation of electrochemical impedance spectra of - batteries (Li-air/Zn-air) for aqueous electrolytes. *Electrochim. Acta* **2021**, *396*, No. 139261.

(15) Kube, A.; Wagner, N.; Friedrich, K. A. Influence of Organic Additives for Zinc-Air Batteries on Cathode Stability and Performance. *J. Electrochem. Soc.* **2021**, *168*, No. 050531.

(16) Barcia, O. E.; D'Elia, E.; Frateur, I.; Mattos, O. R.; Pébere, N.; Tribollet, B. Application of the impedance model of de Levie for the characterization of porous electrodes. *Electrochim. Acta* **2002**, *47*, 2109−2116.

(17) Bienen, F.; Löwe, A.; Hildebrand, J.; Hertle, S.; Schonvogel, D.; Kopljar, D.; Wagner, N.; Klemm, E.; Friedrich, K. A. Degradation study on tin- and bismuth-based gas-diffusion electrodes during electrochemical CO2 reduction in highly alkaline media. *J. Energy Chem.* **2021**, *62*, 367−376.

(18) Hirakata, S.; Mochizuki, T.; Uchida, M.; Uchida, H.; Watanabe, M. Investigation of the effect of pore diameter of gas diffusion layers on cold start behavior and cell performance of polymer electrolyte membrane fuel cells. *Electrochim. Acta* **2013**, *108*, 304−312.

(19) Ambrose, J.; Barradas, R. G. The electrochemical formation of Ag2O in KOH electrolyte. *Electrochim. Acta* **1974**, *19*, 781−786.

(20) Grdeń, M. Impedance study on the capacitance of silver electrode oxidised in alkaline electrolyte. *J. Solid State Electrochem.* **2017**, *21*, 3333−3344.

(21) Sasikala, N.; Ramya, K.; Dhathathreyan, K. S. Bifunctional electrocatalyst for oxygen/air electrodes. *Energy Convers. Manage.* **2014**, *77*, 545−549.

(22) Wittmaier, D.; Cañas, N. A.; Biswas, I.; Friedrich, K. A. Highly Stable Carbon-Free Ag/Co3O4-Cathodes for Lithium-Air Batteries: Electrochemical and Structural Investigations. *Adv. Energy Mater.* **2015**, *5*, 1500763.

(23) Tudela, D. Silver(II) Oxide or Silver(I,III) Oxide? *J. Chem. Educ.* **2008**, *85*, 863.

(24) Danner, T.; Horstmann, B.; Wittmaier, D.; Wagner, N.; Bessler, W. G. Reaction and transport in Ag/Ag2O gas diffusion electrodes of aqueous Li−O2 batteries: Experiments and modeling. *J. Power Sources* **2014**, *264*, 320−332.

(25) Fairweather, J. D.; Cheung, P.; St-Pierre, J.; Schwartz, D. T. A microfluidic approach for measuring capillary pressure in PEMFC gas diffusion layers. *Electrochem. Commun.* **2007**, *9*, 2340−2345.

(26) Gostick, J. T.; Fowler, M. W.; Ioannidis, M. A.; Pritzker, M. D.; Volfkovich, Y. M.; Sakars, A. Capillary pressure and hydrophilic porosity in gas diffusion layers for polymer electrolyte fuel cells. *J. Power Sources* **2006**, *156*, 375−387.

(27) Cheung, P.; Fairweather, J. D.; Schwartz, D. T. Characterization of internal wetting in polymer electrolyte membrane gas diffusion layers. *J. Power Sources* **2009**, *187*, 487−492.

(28) Watanabe, M.; Uchida, H.; Emori, M. Polymer Electrolyte Membranes Incorporated with Nanometer-Size Particles of Pt and/or Metal-Oxides: Experimental Analysis of the Self-Humidification and Suppression of Gas-Crossover in Fuel Cells. *J. Phys. Chem. B* **1998**, *102*, 3129−3137.

(29) Hagihara, H.; Uchida, H.; Watanabe, M. Preparation of highly dispersed SiO2 and Pt particles in Nafion®112 for self-humidifying electrolyte membranes in fuel cells. *Electrochim. Acta* **2006**, *51*, 3979−3985.

(30) Espié, L.; Drevet, B.; Eustathopoulos, N. Experimental study of the influence of interfacial energies and reactivity on wetting in metal/oxide systems. *Metall. Mater. Trans. A* **1994**, *25*, 599−605.

(31) Bartell, F. E.; Cardwell, P. H. Reproducible Contact Angles on Reproducible Metal Surfaces. I. Contact Angles of Water against Silver and Gold1. *J. Am. Chem. Soc.* **1942**, *64*, 494−497.

(32) Gostick, J. T.; Ioannidis, M. A.; Fowler, M. W.; Pritzker, M. D. Wettability and capillary behavior of fibrous gas diffusion media for polymer electrolyte membrane fuel cells. *J. Power Sources* **2009**, *194*, 433−444.

5. Summary

The objective of this work was to investigate the GDE for the reversible Zn-air battery. The large potential range during charging and discharging poses a great challenge for the stability of the materials of the GDE. In addition to the stability and activity of the materials, the largest possible active surface is essential for a high cycle life, since this reduces the required overvoltages during charging and discharging. In the case of GDE, the reaction takes place at the 3-phase boundary, which is why uniform wetting within the pore space with electrolyte, as well as gas-bearing pore spaces extending into the depth, are necessary. Due to expansion of the negative electrode during discharge and shrinkage during charging, the electrolyte pressure within the system changes, which can lead to a change in the electrolyte distribution within the positive electrode pore space. For a basic understanding of the processes, the effects occurring during operation were investigated on a commercial silver electrode. The following effects were considered in this work:

1. *Changes in electrolyte penetration depth*:

   The electrolyte penetration depth can be influenced during operation by the changing volume of the negative and positive electrode as well as by varying wettabilities of the materials of the positive electrode.
   Using a measuring cell in which the electrolyte pressure can be adjusted, increasing flooding of the pore space, as can occur during discharge, was simulated. Here the silver electrode showed decreasing performance with increasing electrolyte pressure. With a measuring cell in which the electrolyte pressure can be adjusted, increasing flooding of the pore space, as can occur during discharge, was simulated. The silver electrode showed a decreasing performance with increasing electrolyte pressure. The evaluation of the impedance spectra showed a slowdown of the electrolyte penetration velocity from an electrolyte pressure of about 11 mbar and that the GDL is also wetted.

2. *Transport parameter*:

   During charging and discharging, the changing oxidation states can lead to large changes in pore distribution, as shown in the case of silver. The changing pore distribution has an influence on the electrolyte distribution in the pore space, on the one hand, and the influence on the permeability as well as the effective ion transport studied in this work, on the other hand.
   For the silver electrode, the reduced electrode showed a 5-fold increase in gas permeability due to the enlargement of the mean pore diameter. The effective diffusion constant of ions in the electrolyte showed an order of magnitude difference between the reduced and oxidized electrodes.

3. *Pressure saturation curves*:

   As shown with the penetration depth experiments, the degree of saturation of the pore space with electrolyte is an important parameter for electrode performance. However, the degree of saturation could not be determined with the electrochemical hydrostatic pressure tests. For this purpose, a special measurement setup was used to specifically determine the saturation as a function of the applied electrolyte pressure.
   For the silver electrode, the influence of the oxidation state could be demonstrated. While the reduced electrode exhibits a hydrophobic character, the silver oxide electrode shows a strongly hydrophilic character and could be filled without any work to be done.

As a further point, the influence of electrolyte additives on the performance and stability of the positive electrode was investigated. Additives are mainly used in Zn-air batteries to improve the properties of the negative electrode, such as lower hydrogen evolution, or better zinc deposition. In this work, an electrolyte mixture consisting of 2 M potassium citrate, 1 M glycine and 0.5 M zinc oxide was investigated for this purpose.
A strongly reduced electrochemical performance was shown, which is independent of the conductive medium and catalyst used and their combination. It was shown that the reduction in performance cannot be attributed solely to a reduction in ionic conductivity. With a mixture of 6 M KOH with 2 M potassium citrate, a similar power reduction as with the electrolyte mixture mentioned above could be reproduced. One explanation for this is the instability of the potassium citrate demonstrated in this work, which decays to CO_2. This causes a breakdown of the ionic transport, which is described by the Grotthuß effect, and thus a strongly reduced ionic conductivity. Furthermore, both the potassium citrate and the gylcine form complexes with metal ions. This was evident in the CV from the absence of reduction and oxidation peaks, as well as pitting evident in post-mortem SEM studies. Additionally, the decomposition of potassium citrate could be shown with gas analysis which showed increased CO_2 and H_2O signals.

6. Zusammenfassung

Das Ziel dieser Arbeit war es, die GDE für die reversible Zn-Luft-Batterie zu untersuchen. Der große Potenzialbereich während des Ladens und Entladens stellt eine große Herausforderung für die Stabilität der Materialien der GDE dar. Neben der Stabilität und Aktivität der Materialien ist eine möglichst große aktive Oberfläche essentiell für eine hohe Zyklenlebensdauer, da dies die benötigten Überspannungen beim Laden und Entladen reduziert. Bei GDEs findet die Reaktion an der 3-Phasen-Grenze statt, weshalb eine gleichmäßige Benetzung innerhalb des Porenraums mit Elektrolyt sowie in die Tiefe reichende gasführende Porenräume notwendig sind. Durch die Ausdehnung der negativen Elektrode beim Entladen und die Schrumpfung beim Laden ändert sich der Elektrolytdruck im System, was zu einer Veränderung der Elektrolytverteilung im Porenraum der positiven Elektrode führen kann. Für ein grundlegendes Verständnis der Vorgänge wurden die während des Betriebs auftretenden Effekte an einer kommerziellen Silberelektrode untersucht. Die folgenden Effekte wurden in dieser Arbeit berücksichtigt:

1. *Veränderungen der Eindringtiefe des Elektrolyten*:

   Die Elektrolyteindringtiefe kann während des Betriebs zum einen durch das sich ändernde Volumen der negativen und positiven Elektroden als auch durch variierende Benetzbarkeiten der Materialien der positiven Elektrode beeinflusst werden.
   Mit einer Messzelle bei welcher der Elektrolytdruck eingestellt werden kann wurde eine zunehmende Flutung des Porenraums, wie es während des Entladens auftreten kann, nachempfunden. Hierbei zeigte sowohl die Silberelektrode eine abnehmende Leistung mit zunehmendem Elektrolytdruck. Die Auswertung der Impedanzspektren zeigte ab einem Elektrolytdruck von ungefähr 11 mbar eine Verlangsamung der Elektrolyteindringgeschwindigkeit sowie das die GDL ebenfalls benetzt wird.

2. *Transportparameter*:

   Während des Ladens und Entladens können die sich ändernden Oxidationstufen, wie im Fall von Silber gezeigt, zu großen Änderungen der Porenverteilung führen. Die veränderte Porenverteilung hat zum einen einen Einfluss auf die Elektrolytverteilung im Porenraum, zum anderen den in dieser Arbeit untersuchten Einfluss auf die Permeabilität sowie den effektiven Ionentransport.
   Für die Silberelektrode zeigte die reduzierte Elektrode eine 5-fach höhere Gaspermeabilität durch die Vergößerung des mittleren Porendurchmessers. Die effektive Diffusionskonstante der Ionen im Elektrolyten zeigte einen Unterschied von einer Größenordnung zwischen der reduzierten und der oxidierten Elektrode.

3. *Drucksättigungskurven*:

Wie mit den Versuchen zur Eindringtiefe gezeigt, ist der Sättigungsgrad des Porenraums mit Elektrolyt ein wichtiger Parameter für die Leistungsfähigkeit der Elektrode. Der Sättigungsgrad konnte mit den elektrochemischen hydrostatischen Druckversuchen jedoch nicht bestimmt werden. Hierfür wurde ein spezieller Messaufbau verwendet und mit diesem gezielt die Sättigung in Abhängigkeit des anliegenden Elektrolytdrucks bestimmt. Für die Silberelektrode konnte der Einfluss des Oxidationszustands nachgewiesen werden. Während die reduzierte Elektrode einen hydrophoben Charakter aufweist, zeigt die Silberoxidelektrode einen stark hydrophilen Charakter und lies sich ohne zu verrichtende Arbeit befüllen.
Die Einzelmessung der Materilien der Ni/Co_3O_4-Mischelektrode zeigte für das Nickel einen leicht hydrophoben Charakter, das Kobaltoxid vergleichbar dem Silberoxid einen stark hydrophilen Charakter. Die Mischelektrode wies eine Mischung aus beiden auf, mit einem vom Herstelldruck sprunghaften Anstieg im reproduzierbaren Bereich. Für den initialen Zyklus zeigte der geringste Herstelldruck von $300\,\mathrm{kN{\cdot}m^{-2}}$ die geringste Benetzbarkeit, die mit $700\,\mathrm{kN{\cdot}m^{-2}}$ gepresste Elektrode aufgrund der Rissbildung in den hydrophilen Kobaltagglomeraten die höchste Benetzbarkeit.

Als weiterer Punkt wurde der Einfluss von Elektrolytadditiven auf die Leistung und Stabilität der positiven Elektrode untersucht. Additive werden in Zn-Luft-Batterien hauptsächlich zur Verbesserung der Eigenschaften der negativen Elektro, wie z.B. geringere Wasserstoffentwicklung, oder bessere Zinkabscheidung eingesetzt. In dieser Arbeit wurde hierfür eine Elektrolytmischung bestehend aus 2 M Kaliumzitrat, 1 M Glyzin und 0,5 M Zinkoxid untersucht.
Es zeigte sich eine stark reduzierte elektrochemische Leistung, welche unabhängig vom verwendeten leitfähigem Medium und Katalysator und deren Kombination ist. Es konnte gezeigt werden, dass die Reduktion der Leistung nicht allein auf eine Reduzierung der ionischen Leitfähigkeit zurückgeführt werden kann. Mit einer Mischungen aus 6 M KOH mit 2 M Kaliumzitrat konnte eine ähnliche Leistungsreduktion wie mit der oben erwähnten Elektrolytmischung nachvollzogen werden. Eine Erklärung hierfür ist die in dieser Arbeit nachgewiesene Instabilität des Kaliumzitrats, welches zu CO_2 zerfällt. Dies bewirkt ein Zusammenbrechen des ionischen Transports, welcher durch den Grotthußeffekt beschrieben wird, und somit eine stark reduzierte ionische Leitfähigkeit. Weiterhin bildet sowohl das Kaliumzitrat, als auch das Gylzin Komplexe mit Metallionen aus. Dies war im CV an der Abwesenheit der Reduktions- und Oxidationspeaks sowie in Post-Mortem Untersuchungen mittels REM ersichtlichem Lochfrass nachvollziehbar.

7. Outlook

Due to the good availability of the materials used in Zn-air batteries and the stage of development, it is a strong alternative to the Li-ion battery for home storage. However, for further commercialization, there are still some challenges to be overcome, which were also evident in this work. On the material side, the need for better catalysts that further reduce overpotentials is of strong importance. The change between oxidized and reduced state of the materials poses great challenges in terms of stability. Furthermore, the reduction of the overpotentials will increase the efficiency of the overall system.
The integration of such catalysts is a challenge. Industrially, GDEs for the primary Zn-air battery are produced in Germany in a dry process similar to the one used by DLR. Attention must be paid here to the stability of the materials during manufacture as well as to the lowest possible loading in order to be cost competitive.

The constant change of oxidation states of the cathode materials leads to a constant change of the wettability and thus the flooding degree of the electrode. For a high cycle stability, further investigations are required here that go beyond the measurements carried out statically at one state in this work. The goal here should be an understanding of the processes in order to be able to develop effective prevention strategies.
Depending on the requirements, different solution strategies are possible. For example, the influence of different electrolyte pressures due to a vertical cell structure can be compensated by grading the pore distribution or the PTFE content. Furthermore, it is possible not to leave the electrolyte static in the vessel, but to minimize the pressure differences by a continuous flow of the electrolyte, as it is already used in industrial operation. A variation of the gas pressure depending on the state of charge or the hydrostatic electrolyte pressure is also a possible solution strategy.

As an important finding from this work, the overall system should be considered at all times for all modifications and optimizations in further developments of Zn-air batteries in order to ensure compatibility of all materials used with each other.

A. Appendix

Supplementary information Publication I:

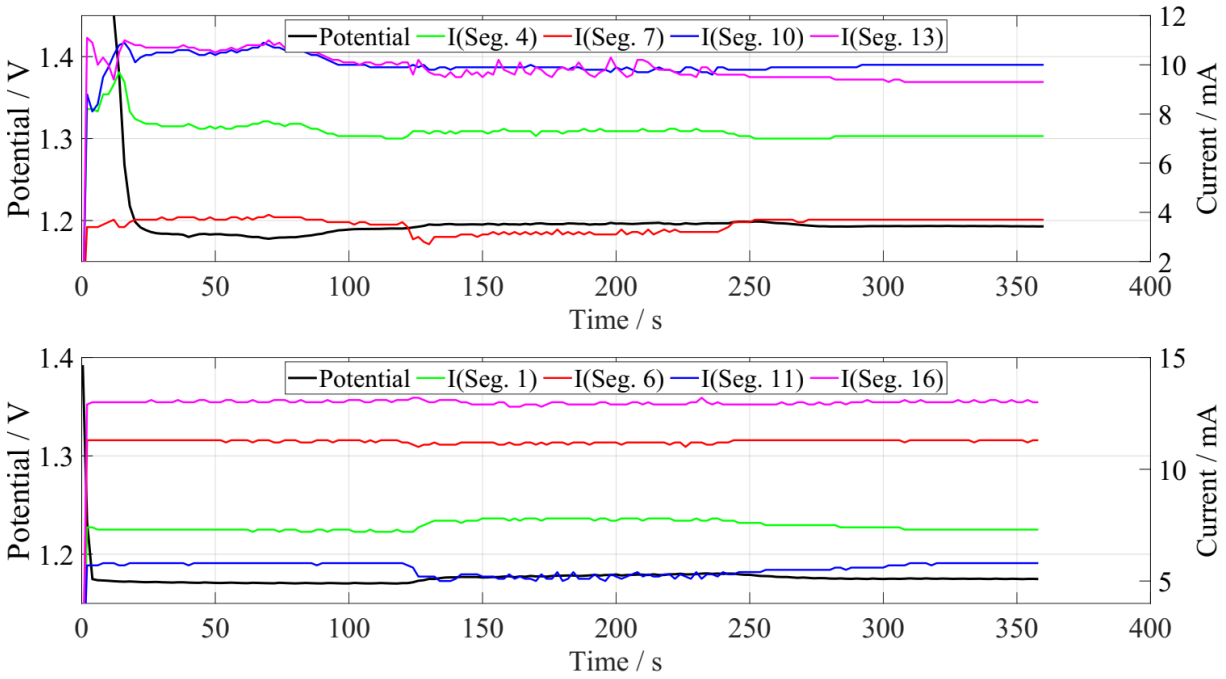

Figure 1:Current and Potential during test with different gas volume flows along gas flow direction. Upper figures show gas flow from lower right (lr) to upper right (ur), lower figures the gas flow from upper left (ul) to lower left (ll)

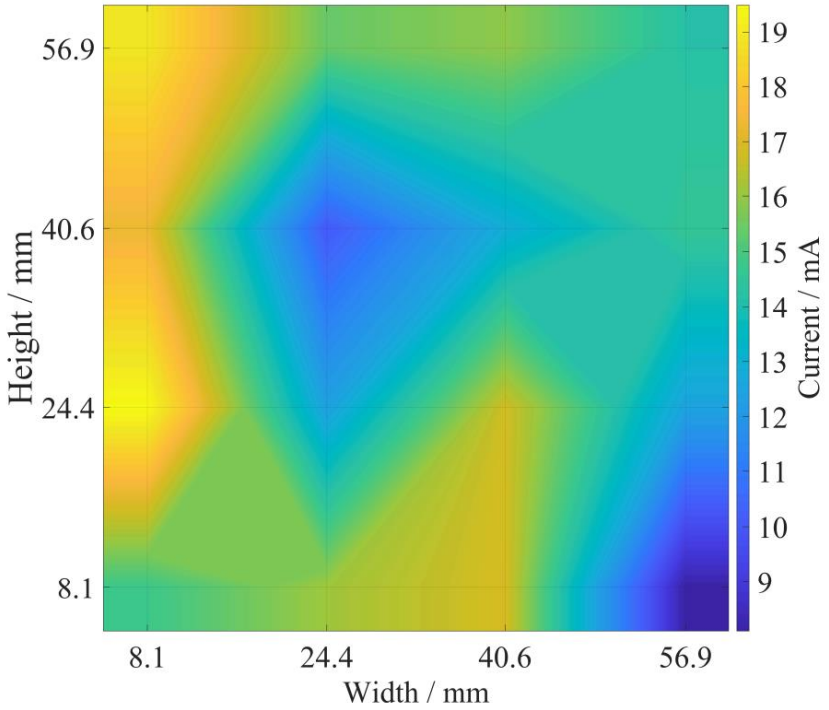

Figure 2: current distribution of discharge test at t=2.78 h

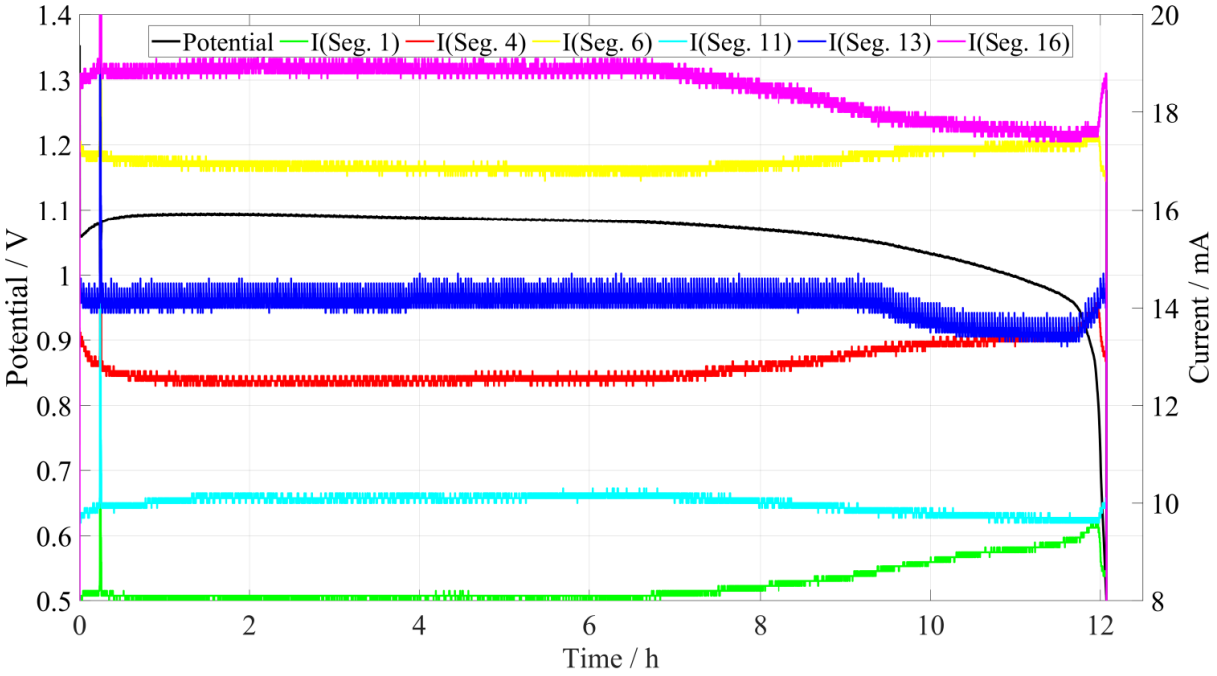

Figure 3: Currents and potential during discharge of Zn-air battery until 0.5 V vs. Zn

Calculation of errors:

Calculation was performed for the maximum systematic error with the equations [1]-[4]

$$y = F(x_1, x_2, x_3, \dots, x_N) \qquad \text{eq. 1}$$

$$\epsilon y = \sum_{i=1}^{N} \left| \frac{\partial F}{\partial x_i} \cdot \epsilon x_i \right| \qquad \text{eq. 2}$$

$$f(x_1, x_2, x_3) = x_1^a x_2^b x_3^c \qquad \text{eq. 3}$$

$$\delta f = |a|\delta x_1 + |b|\delta x_2 + |c|\delta x_3 \qquad \text{eq.4}$$

$$x_i \ll F$$

Y is the target size from which the error is determined. F and f describe functions that are dependent on different error sizes x_i to x_n. ϵx_i describes the absolute error of the error size xi, ϵy the absolute and δf the relative maximum e rror of the function. The variables a, b and c are exponents of the example function f.

Error of electrical circuit

TIV

Source of error	Value x	Rel. Error δx_i	Abs. error Δx_i
Resistance R	100 Ω	± 1 %	± 1 Ω
Voltage U_{out}	4 V	± 0.001 %	± 10 µV

$$U_{out} = I \cdot R = -40\ mA \cdot 100\ \Omega = -4\text{V}$$

With equation [1]-[4]

$$y = U_{out}$$

$$\epsilon y = I \cdot \Delta R = -40\ mA\ \cdot (\pm 1\ \Omega) = \pm 4 \cdot 10^{-2}\ V$$

$$\delta y = 1\ \%$$

U_{out} has an additional error of $\pm 10\ \mu V$ which is only 0.4 % of the absolute error ϵy. This corresponds to an additional relative error of 2.5·10^{-4} % for δy and was not considered due its small influence.

InAmp

Source of error	Value x	Rel. Error δx_i	Abs. error Δx_i
Shunt-Resistance R_S	0.1 Ω	± 1 %	± 0.001 Ω
Var. Resistance R_G	511 Ω	± 1 %	± 5.11 Ω
Amplification G	100 V	± 0.5 %	± 0.5
Voltage V_{out}	4 V	± 1 %	± 0,04 µV

U_{out} is defined by voltage drop U_S in the shunt resistance R_S, multiplied by the amplification G

$$U_{out} = U_{out}^{*} \cdot (1 + \delta U_{out})$$

$$U_{out}^{*} = U_S \cdot G$$

$$G = G^{*} + \Delta G$$

$$G^{*} = \frac{50\ k\Omega}{R_G} + 1$$

Error of amplification G in dependence of the variable resistance R_G

$$y_1 = G^{*}$$

$$y_2 = G$$

$$\epsilon y_1 = \frac{50\ k\Omega}{R_G^2} \cdot \Delta R_G = \frac{50\ k\Omega}{(511\ \Omega)^2} \cdot 5.11\ \Omega = 0.978$$

$$\epsilon y_2 = \epsilon y_1 + \Delta G = 0.978 + 0.5 = 1.478$$

Calculation of absolute error

$$y_3 = U_{out}^{*}$$

$$y = U_{out}$$

$$\epsilon y_3 = G \cdot \Delta U_S + U_S \cdot \Delta G = 0.41\,V$$

$$U^*_{out,max} = 4.41\,V$$

$$\epsilon y = 0.454\,V$$

$$\delta y = 11.35\,\%$$

Max total error

U_{MD} describes the absolute error from the measurement device

TIV: $\Delta U_{tot} = \Delta U_{out,TIV} + \Delta U_{MD} = 0.04\,V$

InAmp: $\Delta U_{tot} = \Delta U_{out,InAmp} + \Delta U_{MD} = 0.454\,V$

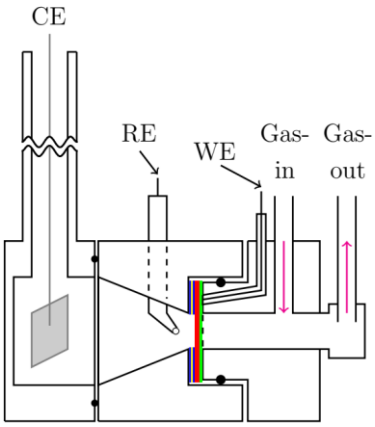

Figure S1: Cell for testing and varying the electrolyte level and therefore the electrolyte pressure. The electrode is depicted in red

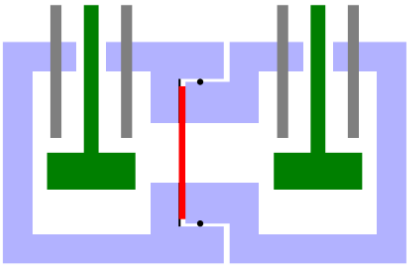

Figure S2: Cell to determine the effective diffusion constant. One compartment is filled with low molarity KOH the other with high molarity KOH. Both compartments are separated by the electrode sample of interest

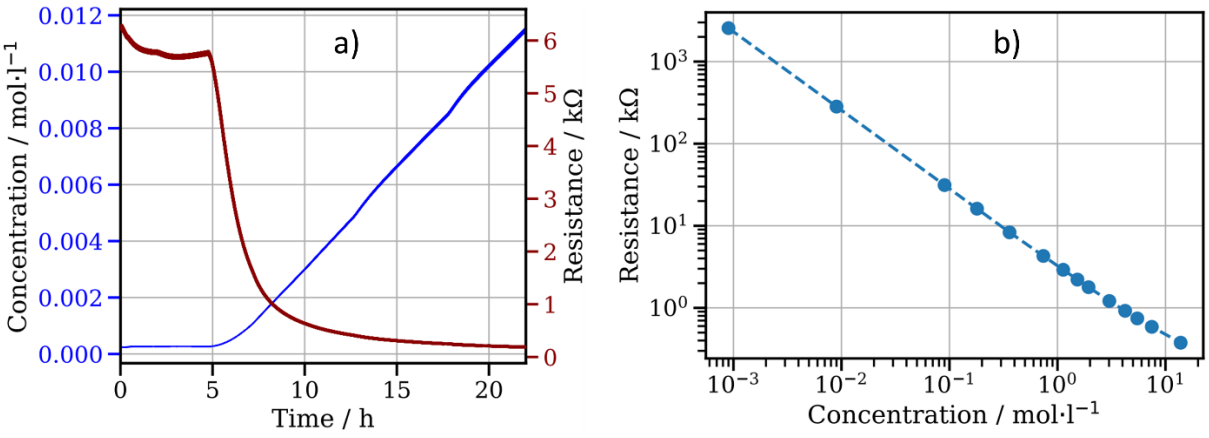

Figure S3: a) Exemplarily measurement (red) to determine the effective diffusion coefficient and the calculated concentration (blue) in the compartment with the lower molarity KOH b) Calibration curve

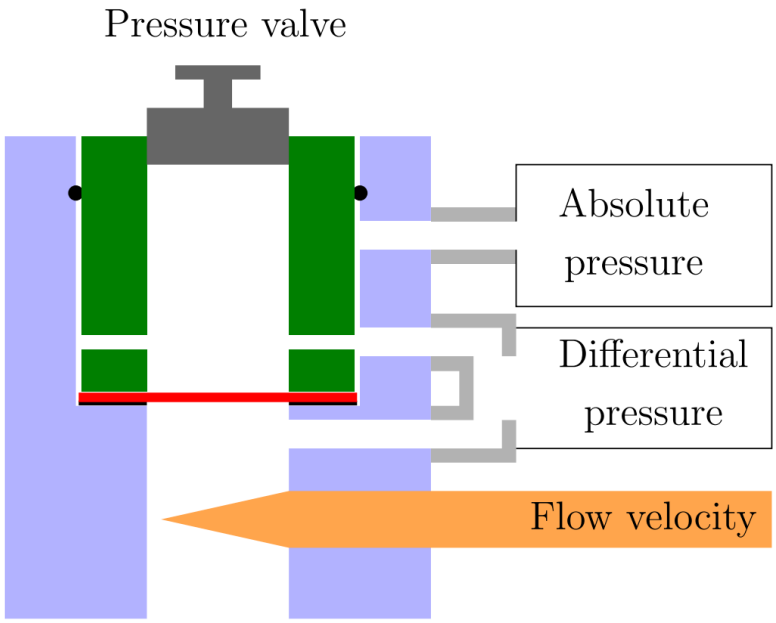

Figure S4: Test setup to determine the permeability. The sample (red) is mounted and the pressure in the upper compartment is slowly increased. The absolute pressure and pressure difference above and below the sample are ~~measures~~ measured as well as the gas flow velocity

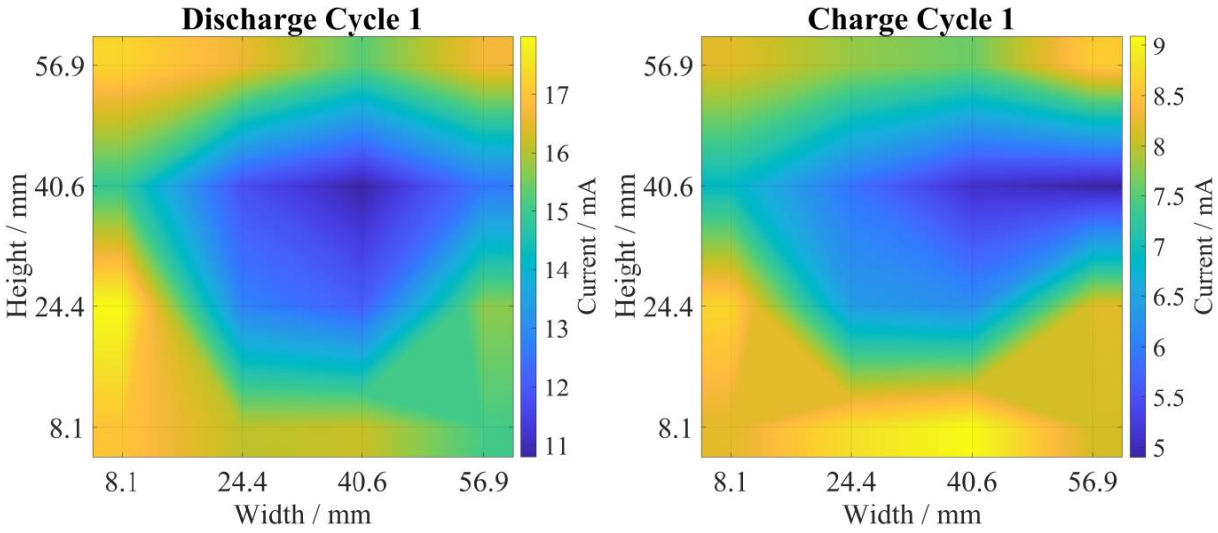

S5: Current density maps used for normalization. These maps show the current distribution 8 s after the corresponding reaction has started to allow for stabilization of the system

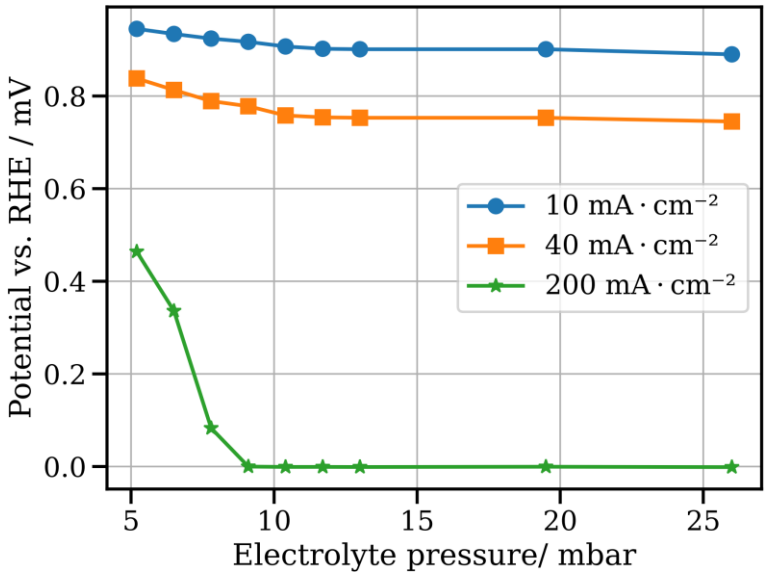

S6: Voltage vs. hydrostatic electrolyte pressure for -10, -40 and -200 mA*cm^{-2} measured at 25 °C with pure O_2 and 32 wt.% KOH

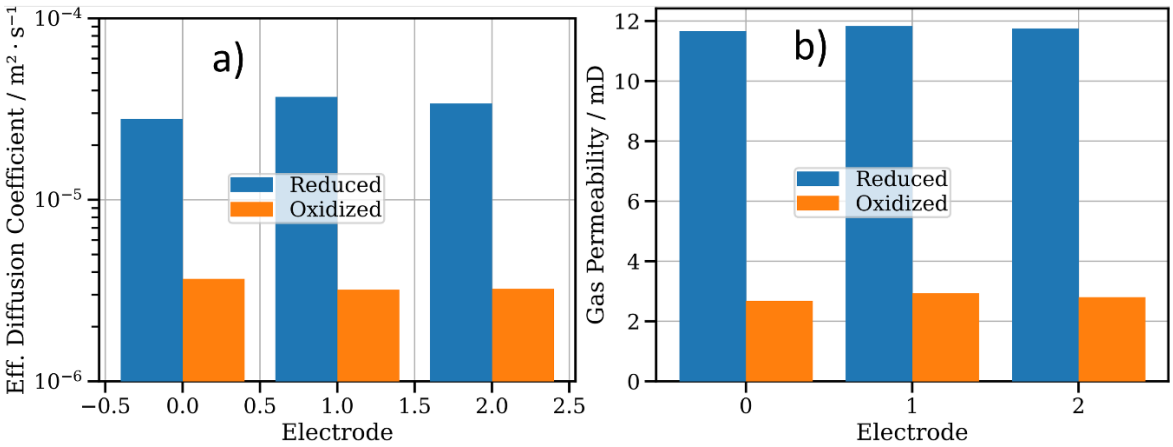

Figure S7: Measurement results of the effective diffusion coefficient (a) at 25°C and the result of the gas permeability test for the oxidized (orange) and reduced electrode (blue)

Bibliography

[1] Marija Maisch. South australia's tesla big battery saves 40 million dollar in grid stabilization costs. www.pv-magazine.com/2018/12/05/south-australias-tesla-big-battery-saves-40-million-in-grid-stabilization-costs, 2018. [Online; Zugriff: 28. August. 2019].

[2] The Korea Times. Gov't officials clueless about cause of ess fires. www.koreatimes.co.kr/www/tech/2019/05/129_268188.html, 2018. [Online; Zugriff: 24. Maerz. 2020].

[3] Yanguang Li and Jun Lu. Metal-air batteries: Will they be the future electrochemical energy storage device of choice? *ACS Energy Letters*, 2(6):1370–1377, 2017.

[4] E. Davari and D. G. Ivey. Bifunctional electrocatalysts for zn-air batteries. *Sustainable Energy Fuels*, 2:39–67, 2018.

[5] G. W. Heise. Battery cell, U.S. patent US2077561A, 1933.

[6] George W. Heise and Erwin A. Schumacher. An air?depolarized primary cell with caustic alkali electrolyte. *Transactions of The Electrochemical Society*, 62(1):383–391, 1932.

[7] D. V. Ragone. Review of battery systems for electrically powered vehicles. In *SAE Technical Paper*. SAE International, 02 1968.

[8] Richard Eckl, Peter Burda, Armin Förg, Harald Finke, and Markus Lienkamp. Alternative range extender for electric cars - zinc air batteries. In *Conference on Future Automotive Technology*, pages 3–18, 03 2012.

[9] Cody A. Friesen, Ramkumar Krishnan, Toni Tang, and Derek Wolfe. Metal-air cell comprising an electrolyte with a room temperature ionic liquid and hygroscopic additive, U.S. patent US8808929B2, 2011.

[10] Jang-Soo Lee, Sun Tai Kim, Ruiguo Cao, Nam-Soon Choi, Meilin Liu, Kyu Tae Lee, and Jaephil Cho. Metal-air batteries with high energy density: Li-air versus zn-air. *Advanced Energy Materials*, 1(1):34–50, 2011.

[11] Dennis Wittmaier, Simon Aisenbrey, Norbert Wagner, and K. Andreas Friedrich. Bifunctional, carbon-free nickel/cobalt-oxide cathodes for lithium-air batteries with an aqueous alkaline electrolyte. *Electrochimica Acta*, 149:355–363, 2014.

[12] Dennis Wittmaier, Norbert Wagner, K. Andreas Friedrich, Hatem M.A. Amin, and Helmut Baltruschat. Modified carbon-free silver electrodes for the use as cathodes in lithium-air

batteries with an aqueous alkaline electrolyte. *Journal of Power Sources*, 265:299 – 308, 2014.

[13] Ludwig Jörissen. Bifunctional oxygen/air electrodes. *Journal of Power Sources*, 155(1):23 – 32, 2006. Selected papers from the 88th BunsenkolloquiumIn honour of Prof. Dr. Jürgen Garche's 60th birthday88th Bunsenkolloquium.

[14] S. Kaliaguine W. Prellier P. Granger, V. I. Parvulescu. *Perovskites and Related Mixed Oxides: Concepts and Applications*. John Wiley & Sons, 2016.

[15] P. Hosseini Benhangi, A. Alfantazi, and E. Gyenge. Manganese dioxide-based bifunctional oxygen reduction/evolution electrocatalysts: Effect of perovskite doping and potassium ion insertion. *Electrochimica Acta*, 123:42 – 50, 2014.

[16] Jang-Soo Lee, Sun Tai Kim, Ruiguo Cao, Nam-Soon Choi, Meilin Liu, Kyu Tae Lee, and Jaephil Cho. Metal-air batteries with high energy density: Li-air versus zn-air. *Advanced Energy Materials*, 1(1):34–50, 2011.

[17] Niklas Borchers, Simon Clark, Birger Horstmann, Kaushik Jayasayee, Mari Juel, and Philippe Stevens. Innovative zinc-based batteries. *Journal of Power Sources*, 484:229309, 2021.

[18] A. Kube A. Blasquez D. Wittmaier, N. Wagner and A. Ramos. Secondary cell, accumulator comprising one or more secondary cells, and method for charging and discharging, U.S. patent US20200358156, 2018.

[19] Alexander Kube, Norbert Wagner, and Kaspar Andreas Friedrich. Influence of organic additives for zinc-air batteries on cathode stability and performance. *Journal of The Electrochemical Society*, 168(5):050531, may 2021.

[20] Simon Clark, Arnulf Latz, and Birger Horstmann. Rational development of neutral aqueous electrolytes for zinc-air batteries. *ChemSusChem*, 10(23):4735–4747, 2017.

[21] F. W. Thomas Goh, Zhaolin Liu, T. S. Andy Hor, Jie Zhang, Xiaoming Ge, Yun Zong, Aishui Yu, and Weiliang Khoo. A near-neutral chloride electrolyte for electrically rechargeable zinc-air batteries. *Journal of The Electrochemical Society*, 161(14):A2080–A2086, 2014.

[22] Afriyanti Sumboja, Xiaoming Ge, Guangyuan Zheng, F.W. Thomas Goh, T.S. Andy Hor, Yun Zong, and Zhaolin Liu. Durable rechargeable zinc-air batteries with neutral electrolyte and manganese oxide catalyst. *Journal of Power Sources*, 332:330 – 336, 2016.

[23] Mega Kar, Tristan J. Simons, Maria Forsyth, and Douglas R. MacFarlane. Ionic liquid electrolytes as a platform for rechargeable metal-air batteries: a perspective. *Phys. Chem. Chem. Phys.*, 16:18658–18674, 2014.

[24] Z. Liu, S. Zein El Abedin, and F. Endres. Electrodeposition of zinc films from ionic liquids and ionic liquid/water mixtures. *Electrochimica Acta*, 89:635 – 643, 2013.

[25] Soraya Hosseini, Salman Masoudi Soltani, and Yuan-Yao Li. Current status and technical challenges of electrolytes in zinc-air batteries, an in-depth review. *Chemical Engineering Journal*, 408:127241, 2021.

[26] A.P. Manso, F.F. Marzo, J. Barranco, X. Garikano, and M. Garmendia Mujika. Influence of geometric parameters of the flow fields on the performance of a pem fuel cell. a review. *International Journal of Hydrogen Energy*, 37(20):15256–15287, 2012. The 2011 Asian Bio-Hydrogen and Biorefinery Symposium (2011ABBS).

[27] Thangavel Sangeetha, Po-Tuan Chen, Wei-Mon Yan, and K. David Huang. Enhancement of air-flow management in zn-air fuel cells by the optimization of air-flow parameters. *Energy*, 197:117181, 2020.

[28] Ahmed Habib Shallal and Ibtehal Kareem Shakir. Effects of operating parameters on the performance of a zinc-air fuel cell. *Journal of Physics: Conference Series*, 1973(1):012122, aug 2021.

[29] Birgit Pichler, Stephan Weinberger, Lucas Rescec, Ilena Grimmer, Florian Gebetsroither, Brigitte Bitschnau, and Viktor Hacker. Bifunctional electrode performance for zinc-air flow cells with pulse charging. *Electrochimica Acta*, 251:488–497, 2017.

[30] Melanie Cornelia Paulisch, Marcus Gebhard, David Franzen, André Hilger, Markus Osenberg, Shashidhara Marathe, Christoph Rau, Barbara Ellendorff, Thomas Turek, Christina Roth, and Ingo Manke. Operando synchrotron imaging of electrolyte distribution in silver based gas diffusion electrodes during oxygen reduction reaction in highly alkaline media. *ACS Applied Energy Materials*, 4(8):7497–7503, 2021.

[31] Maximilian Röhe, David Franzen, Fabian Kubannek, Barbara Ellendorff, Thomas Turek, and Ulrike Krewer. Revealing the degree and impact of inhomogeneous electrolyte distributions on silver based gas diffusion electrodes. *Electrochimica Acta*, 389:138693, 2021.

[32] Daniel Schröder, Tobias Arlt, Ulrike Krewer, and Ingo Manke. Analyzing transport paths in the air electrode of a zinc air battery using x-ray tomography. *Electrochemistry Communications*, 40:88–91, 2014.

[33] Ze Ma, Pucheng Pei, Keliang Wang, Xizhong Wang, Huachi Xu, Yongfeng Liu, and Guanlin peng. Degradation characteristics of air cathode in zinc air fuel cells. *Journal of Power Sources*, 274:56–64, 2015.

[34] King Wai Choi, Drannan Hamby, Douglas N. Bennion, and John Newman. Engineering analysis of shape change in zinc secondary electrodes: II . experimental. *Journal of The Electrochemical Society*, 123(11):1628–1637, nov 1976.

[35] Jing Li, Qiaowei Lin, Zhi Zheng, Liuyue Cao, Wei Lv, and Yuan Chen. How is cycle life of three-dimensional zinc metal anodes with carbon fiber backbones affected by depth of discharge and current density in zincion batteries. *ACS Applied Materials & Interfaces*, 14(10):12323–12330, 2022. PMID: 35234443.

[36] Pucheng Pei, Keliang Wang, and Ze Ma. Technologies for extending zincair battery s cyclelife a review. *Applied Energy*, 128:315–324, 2014.

[37] Joseph F. Parker, Christopher N. Chervin, Eric S. Nelson, Debra R. Rolison, and Jeffrey W. Long. Wiring zinc in three dimensions re-writes battery performancedendrite-free cycling. *Energy Environ. Sci.*, 7:1117–1124, 2014.

[38] X. Gregory Zhang. Fibrous zinc anodes for high power batteries. *Journal of Power Sources*, 163(1):591–597, 2006. Special issue including selected papers presented at the Second International Conference on Polymer Batteries and Fuel Cells together with regular papers.

[39] Daniel Deckenbach and Jörg J. Schneider. A 3d hierarchically porous nanoscale zno anode for high-energy rechargeable zinc-air batteries. *Journal of Power Sources*, 488:229393, 2021.

[40] Chang Woo Lee, K. Sathiyanarayanan, Seung Wook Eom, Hyun Soo Kim, and Mun Soo Yun. Effect of additives on the electrochemical behaviour of zinc anodes for zinc/air fuel cells. *Journal of Power Sources*, 160(1):161–164, 2006.

[41] Kee Wah Leong, Yifei Wang, Meng Ni, Wending Pan, Shijing Luo, and Dennis Y.C. Leung. Rechargeable zn-air batteries: Recent trends and future perspectives. *Renewable and Sustainable Energy Reviews*, 154:111771, 2022.

[42] Aroa R. Mainar, Luis C. Colmenares, Hans-Jürgen Grande, and J. Alberto Blázquez. Enhancing the cycle life of a zincair battery by means of electrolyte additives and zinc surface protection. *Batteries*, 4(3), 2018.

[43] Chang Woo Lee, K. Sathiyanarayanan, Seung Wook Eom, and Mun Soo Yun. Studies on suppression of hydrogen evolution reaction for zinc/air fuel cell. In *THERMEC 2006*, volume 539 of *Materials Science Forum*, pages 1427–1430. Trans Tech Publications Ltd, 2 2007.

[44] Mao-Chia Huang, Shih-Hsuan Huang, Sheng-Cheng Chiu, Kan-Lin Hsueh, Wen-Sheng Chang, Chang-Chung Yang, Ching-Chen Wu, and Jing-Chie Lin. Improved electrochemical performance of znair secondary batteries via novel organic additives. *Journal of the Chinese Chemical Society*, 65(10):1239–1244, 2018.

[45] Simon Clark, Aroa Ramos Mainar, Elena Iruin, Luis César Colmenares, Jose Alberto Blázquez, Julian Richard Tolchard, Zenonas Jusys, and Birger Horstmann. Designing aqueous organic electrolytes for zincair batteries: Method, simulation, and validation. *Advanced Energy Materials*, 10(10):1903470, 2020.

[46] Hao-Fan Wang and Qiang Xu. Materials design for rechargeable metal-air batteries. *Matter*, 1(3):565–595, 2019.

[47] Dennis Wittmaier. *Herstellung und Charakterisierung bifunktioneller Sauerstoffelektroden für die hochenergetische Lithium-Luft-Batterien*. PhD thesis, Universität Stuttgart, 2016.

[48] F. Scholz, G. Inzelt, F. Marken, and Z. Stojek. *Electroanalytical Methods - Guide to Experiments and Applications*. Springer-Verlag Berlin Heidelberg, 2002.

[49] A. Ševčik. Oscillographic polarography with periodical triangular voltage. *Collection of Czechoslovak Chemical Communications*, 13(5):349–377, 1948.

[50] R.Holze. *Impedanzmessungen an porösen Elektroden*. PhD thesis, Rheinische Friedrich-Wilhelms-Universität, Bonn, 1983.

[51] N. Bonanos, B. C. H. Steele, E. P. Butler, J. Ross Macdonald, William B. Johnson, Wayne L. Worrell, Gunnar A. Niklasson, Sara Malmgren, Maria Strømme, S. K. Sundaram, Michael C. H. McKubre, Digby D. Macdonald, George R. Engelhardt, Evgenij Barsoukov, Brian. E. Conway, Wendy. G. Pell, Norbert Wagner, C. M. Roland, and Robert S. Eisenberg. *Applications of Impedance Spectroscopy*, chapter 4, pages 175–478. John Wiley and Sons, Ltd, 2018.

[52] A. Leonide, V. Sonn, and E. Ivers-Tiffee. Evaluation and modeling of the cell resistance in anode-supported solid oxide fuel cells. *Journal of the Electrochemical Society*, 155(1):B36–B41, 2008.

[53] Enis Tuncer and J. Ross Macdonald. Comparison of methods for estimating continuous distributions of relaxation times. *Journal of Applied Physics*, 99(7):074106, 2006.

[54] H. Schichlein, A.C. Müller, M. Voigts, A. Krügel, and E. Ivers-Tiffée. Deconvolution of electrochemical impedance spectra for the identification of electrode reaction mechanisms in solid oxide fuel cells. *Journal of Applied Electrochemistry*, 32(8):875–882, Aug 2002.

[55] Mattia Saccoccio, Ting Hei Wan, Chi Chen, and Francesco Ciucci. Optimal regularization in distribution of relaxation times applied to electrochemical impedance spectroscopy: Ridge and lasso regression methods - a theoretical and experimental study. *Electrochimica Acta*, 147:470 – 482, 2014.

[56] Francesco Ciucci and Chi Chen. Analysis of electrochemical impedance spectroscopy data using the distribution of relaxation times: A bayesian and hierarchical bayesian approach. *Electrochimica Acta*, 167:439 – 454, 2015.

[57] Ting Hei Wan, Mattia Saccoccio, Chi Chen, and Francesco Ciucci. Influence of the discretization methods on the distribution of relaxation times deconvolution: Implementing radial basis functions with drttools. *Electrochimica Acta*, 184:483 – 499, 2015.

[58] Herbert Giesche. Mercury porosimetry: A general (practical) overview. *Particle & Particle Systems Characterization*, 23(1):9–19, 2006.

[59] Krista S. Walton and Randall Q. Snurr. Applicability of the bet method for determining surface areas of microporous metal?organic frameworks. *Journal of the American Chemical Society*, 129(27):8552–8556, 2007. PMID: 17580944.

[60] Jürgen Bauch and Rüdiger Rosenkranz. *REM - Rasterelektronenmikroskopie*, pages 6–7. Springer Berlin Heidelberg, Berlin, Heidelberg, 2017.

[61] H. Stanjek and W. Häusler. Basics of x-ray diffraction. *Hyperfine Interactions*, 154(1):107–119, Jun 2004.

[62] Seong Jin Kim, Robert Dean, Robert L. Jackson, and George T. Flowers. An investigation of the damping effects of various gas environments on a vibratory mems device. *Tribology International*, 44(2):125 – 133, 2011.

[63] A.E. Scheidegger. *Corrosion and Electrochemistry of Zinc*. University of Toronto Press, 1963.

[64] B Ph van Milligen, P D Bons, B A Carreras, and R Sánchez. On the applicability of fick's law to diffusion in inhomogeneous systems. *European Journal of Physics*, 26(5):913–925, jul 2005.

[65] Jeff Gostick. *Multiphase Mass Transfer and Capillary Properties of Gas Diffusion Layers for Polymer Electrolyte Membrane Fuel Cells*. PhD thesis, Universität of Waterloo, 2008.

[66] Norman R. Morrow. Physics and thermodynamics of capillary action in porous media. *Industrial & Engineering Chemistry*, 62(6):32–56, 1970.

Publications

Poster

K. Kube, D. Wittmaier, N. Wagner, and K. A. Friedrich: *Production and characterization of bi-functional cathodes for secondary zinc-air batteries*, 67th ISE Meeting Den Haag(August 21 - August 26, 2016)

A. Kube, N. Wagner, and K. A. Friedrich: *Development of Bifunctional Catalysts/Electrodes for Rechargeable Zn-Air Batteries in Alkaline and Near-Neutral Electrolyte*, Kraftwerk Batterie Münster (March 28 - March 30, 2017)

A. Kube, N. Wagner, and K. A. Friedrich: *Improving Zn-air batteries by using results from electrochemical impedance spectroscopy*, Electrochemistry Ulm (September 24 - September 26, 2018)

A. Kube, N. Wagner, and K. A. Friedrich: *Wetting behavior of electrolyte in a GDE and how it affects performance in Zn-air battery*, GDE Symposia Magdeburg (September 23 - September 25, 2019)

C. Schmitt, K. Schad, A. Kube, N. Wagner and K. A. Friedrich: *Anode-Controlled Fast Charging Optimization of Lithium Ion Batteries*, Advanced Battery Power (April 27 - April 29, 2021)

Q. Chen , A. Kube , D. Kopljar , N. Wagner, S. Geiger , M. Schmidt , K. A. Friedrich: *Rational design of single-layer carbon-supported Cu-B GDE for CO_2 electroreduction to C_{2+} products*, Advanced Battery Power (April 27 - April 29, 2021)

C. Schmitt, A. Kube, N. Wagner, and K. A. Friedrich: *Operando X-ray Diffraction of Graphite (De-)lithiation at Various Temperatures*, International Operando Battery Days (May 16 - May 18, 2022)

A. Kube, N. Wagner, and K. A. Friedrich: *Wetting behavior of electrolyte in a silver GDE and how it affects performance in Metal-air batteries*, GDE Symposia Magdeburg (September 5 - September 7, 2022)

Talks

K. Jayasayee, C. Bathgate, R. Oates, S. M. Hanetho, J. R. Tolchard, L. Colmenares, S.

Labonnote-Weber, A. Kube, and M. Juel: *Development of Bifunctional Catalysts/Electrodes for Rechargeable Zn-Air Batteries in Alkaline and Near-Neutral Electrolyte*, for 231st ECS Meeting New-Orleans (May 28 - June 2, 2017)

A. Kube, N. Wagner, and K. A. Friedrich: *Influence of Electrolyte Penetration Depth and How It Affects the Electrochemical Performance of Cathodes in Zn-Air Batteries*, for 231st ECS Meeting New-Orleans (May 28 - June 2, 2017)

A. Kube, N. Wagner, and K. A. Friedrich: *Influence of Electrolyte Penetration Depth and How It Affects the Electrochemical Performance of Cathodes in Zn-Air Batteries*, Zn-Air Battery Workshop Ulm (June 23, 2017)

N. Wagner, D. Wittmaier, N.A. Cañas, I. Biswas, A. Kube, and K. A. Friedrich: *Highly Stable Carbon-Free Cathodes for Li-Air Batteries with Aqueous Alkaline Electrolyte: Electrochemical and Structural Investigations*, 68th Annual Meeting of ISE 2017 Providence (August 276 - September 1, 2017)

N. Wagner, A. Kube, and K. A. Friedrich: *Study of the Electrolyte Penetration Depth of Cathodes in Zn-Air Batteries by Electrochemical Impedance Spectroscopy*, IWIS 2017 Chemnitz (September 27 - September 29, 2017)

A. Kube, N. Wagner, and K. A. Friedrich: *Material screening for bifunctonal cathodes and how operaton conditons influences their performance*, IZABW2 Trondheim (April 11 - April 12, 2018)

K. Jayasayee, C. Bathgate, R. Oates, S. M. Hanetho, J. R. Tolchard, L. Colmenares, S. Labonnote-Weber, A. Kube, and M. Juel: *Development of $Ni_xCo_3 - xO_4$ as bifunctonal catalysts for rechargeable Zn-Air*, IZABW2 Trondheim (April 11 - April 12, 2018)

B. Abrashev, K. Petrov, D. Uzun, M. Slavova, E. Mladenova, B. Burdin, E. Mihaylova-Dimitrova, A. Kube, N. Wagner, M. Juel, D. Vladikova, and Z. Stoynov: *The Zinc Air Bateries at IEES - Past, Present, Future Plans*, IZABW2 Trondheim (April 11 - April 12, 2018)

N. Wagner, A. Kube, and K. A. Friedrich: *Post Li-Ion Batteries*, ErnerEn Baile Govora (October 24 - October 26, 2018)

N. Wagner, A. Kube, and K. A. Friedrich: *Evaluation of electrochemical impedance spectra of metal-air batteries (Li-air/Zn-air) for aqueous and organic electrolytes*, IWIS 2019 Chemnitz (September 25 - September 27, 2019)

N. Wagner, A. Kube, and K. A. Friedrich: *Evaluation of electrochemical impedance spectra of metal-air batteries (Li-air/Zn-air) for aqueous and organic electrolytes*, Electrochemical Days

(SED) 2019 Sofia (October 16 - October 19, 2019)

N. Wagner, M. Nojabaee, M. Gerle, A. Kube, F. Bienen, and K. A. Friedrich: *Electrochemical impedance spectroscopic investigations of porous and gas diffusion electrodes for various applications*, EnergEn21 2021 Baile Govora (October 26 - October 29, 2019)

Patents

D. Wittmaier, N. Wagner, A. Kube, A. Blasquez and A. Ramos: *Secondary cell, accumulator comprising one ore more secondary cells, and method for charging and discharging*, WO/2018/099955 (2018)

A. Kube, T. Kaz: *Trockene Herstellung von Li-Ionen All-Solid State-Batterieelektroden*, DE102022116218.4 (2022)

Peer-reviewed Publications

A. Kube, N. Wagner and K.A. Friedrich: *Influence of organic additives for zinc-air batteries on cathode stability and performance* , Journal of Electrochemical Society, Volume 168, Issue 5, 050531 (2021)

A. Kube, W. Strunz, N. Wagner and K.A. Friedrich: *Evaluation of electrochemical impedance spectra of metal-air batteries (Li-air/Zn-air) for aqueous electrolytes*, Electrochimica Acta, Volume 396, 139261 (2021)

A. Kube, J. Meyer, D. Kopljar, N. Wagner and K. A. Friedrich: *A segmented cell measuring technique for current distribution measurements in Zn-air batteries* , Journal of the Electrochemical Society, Volume 168, Issue 12, 120530 (2021)

A. Kube, N. Wagner and K. A. Friedrich: *Influence of Cycling onto electrolyte distribution inside a silver-based gas diffusion electrode for Zn-Air batteries*, ACS Sustainable Chemistry & Engineering , Volume 10, Issue 51, 1710717115 (2022)

Not part of this dissertation:

C. Schneider, T.Heindel, A.Huggenberger, T.A. Niederstrasser, S.Reitzenstein, A. Forchel, S.Höfling and M. Kamp: *Microcavity enhanced single photon emission from an electrically driven site-controlled quantum dot* , Applied Physics Letters, Volume 100, Issue 9, 091108 (2012)

B. Abrashev, D. Uzun, A. Kube, N. Wagner, K. Petrov: *Optimization of the bi-functional oxygen electrode (BOE) structure for application in a Zn-air accumulator*, Bulgarian Chemical Communications, Volume 52, Issue 2, 245 - 249 (2020)

C. Schmitt, A. Kube, N. Wagner and K. A. Friedrich: *Understanding the Influence of Temperature on the Phase Evolution during Li-Graphite (De-)Intercalation Processes: An Operando X-ray Dif-fraction Study*, ChemElectroChem (2021)

A. Kube, B. Bienen, N. Wagner and K. A. Friedrich: *Wetting behavior of aprotic Li-air battery*, Advanced Materials Interfaces, Volume 9, Issue 4, 2101569 (2021)

Patrick Sarkezi-Selsky, Henrike Schmies, Alexander Kube, Arnulf Latz and Thomas Jahnke: *Lattice Boltzmann simulation of liquid water transport in gas diffusion layers of proton exchange membrane fuel cells: Parametric studies on capillary hysteresis*, Journal of Power Sources, Volume 535, 231381 (2022)

Jan Petersen, Alexander Kube, Sebastian Geier and Peter Wierach: *Structure-Integrated Thin-Film Supercapacitor as a Sensor*, Sensors, Volume 22, Issue 18, 6932 (2022)

Acknowledgement

At this point I would like to thank all those who contributed to the success of this thesis:

I would like to thank Prof. Dr. A. Friedrich and Norbert Wagner for accepting me at the German Aerospace Center and for giving me the opportunity to carry out this thesis with its interesting topic. I would also like to thank my second examiner Prof. Thomas Turek. For the many substantive and challenging discussions during our joint project, I would like to especially thank Mathias, Aroa, Kaushik, and Louis. The constant input helped a lot to understand the problems of the system and to think outside the box.

At DLR special thanks go to Timo and Patrick who supported me a lot during the simulations, both in the organization and in the execution. Also that I was allowed to use the simulation tools developed by you. I would like to thank Werner for his constant commitment to help me with the development and construction of new measuring cells. Without you some of this work would not have been possible. For the good working environment I thank my dear colleagues, Fabian, Joachim, Jan, Oli, Chris, Dirk and Miriam.

Furthermore, I would like to thank my wife and my two children, who have always cheered me up even in the difficult moments that one has during the dissertation, as well as the pink ant Lilifee.

Declaration

I declare that I have prepared this doctoral thesis independently and without the use of any auxiliary materials other than those indicated.

Stuttgart, April 12, 2023

Alexander Kube